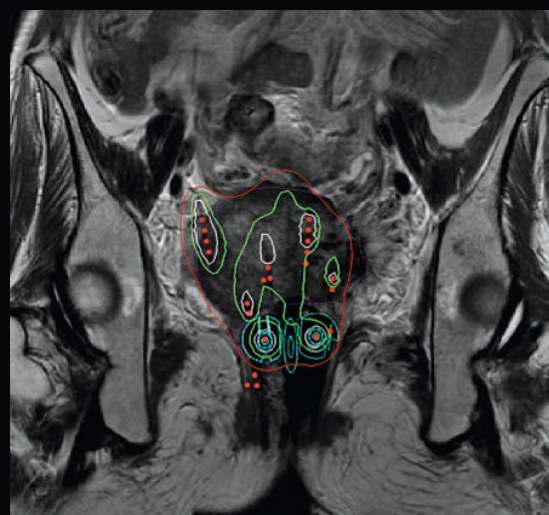
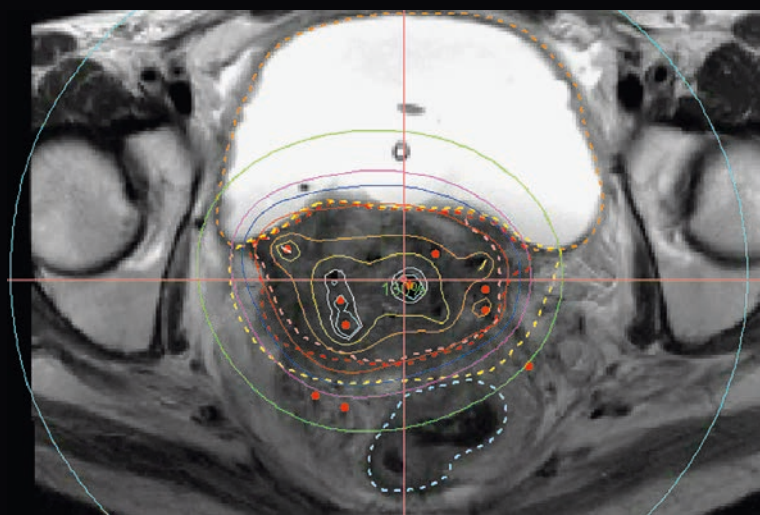
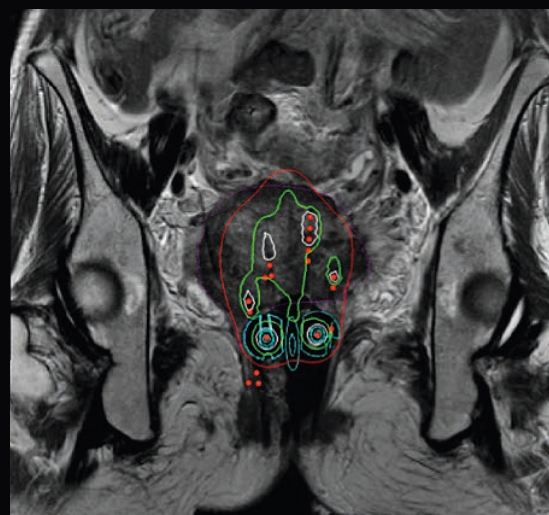
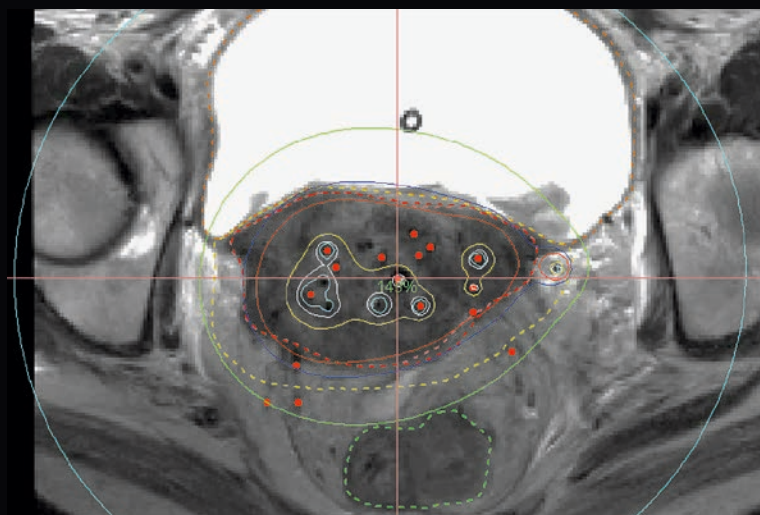


Editorial Comment
MRI in Radiation Therapy
David A. Jaffray
Page 2

MRI in Head-and-Neck
RT Planning
Houda Bahig
Page 6

Integrating DWI & DTI into
RT Treatment Planning of
Brain Tumors
Tong Zhu
Page 26

Utilizing 4D-MRI for
Radiation Treatment
Planning
Eric S. Paulson
Page 32



Not for distribution in the US

MReadings: MR in RT

Contributions from our MAGNETOM users
3rd Edition ESTRO 2017



David Jaffray graduated from the University of Alberta, Canada, with a B.Sc. in Physics (Hons.) in 1988 and completed his Ph.D. in the Department of Medical Biophysics at the University of Western Ontario in 1994. Following graduation, he took a position as Staff Physicist in the Department of Radiation Oncology at William Beaumont Hospital in Michigan, USA, where he instigated a direction of research that garnered funding from the National Institutes of Health (NIH) and from congressionally-directed funding programs. Dr. Jaffray became a Board Certified Medical Physicist (ABMP – Radiation Oncology) in 1999. In 2002, he joined the Princess Margaret Hospital in Toronto as Head of Radiation Physics and a Senior Scientist within the Ontario Cancer Institute. David holds the Fidani Chair in Radiation Physics, and is the Director of the TECHNA Institute for Health Technology Development at the University Health Network. In October of 2015, he became the Executive Vice President of Technology and Innovation at the University Health Network. He is a Professor in the Departments of Radiation Oncology, Medical Biophysics, and Institute for Biomaterials and Biomedical Engineering at the University of Toronto.

His primary area of research has been in the development and application of image-guided therapy. He has over 5 patents issued and several licensed, including, kilovoltage cone-beam computed tomography for image-guided radiation therapy. Dr. Jaffray has >200 peer-reviewed publications in the field, >100 invited lectures, and holds numerous peer-review and industry sponsored research grants. He sits on numerous scientific and research boards and has contributed to the NIH and CIHR grant review process for several years. He is an active member of the American Association of Physicists in Medicine (AAPM) and has an active teaching role in workshops and annual meetings of the American Society of Therapeutic Radiation Oncology (ASTRO). He has an active interest in commercialization and led the development of a variety of commercial products including software and hardware for quality assurance and the development of small animal irradiator systems for basic research. He has successfully supervised over 20 graduate students and fellows. Dr. Jaffray has won each of the major prizes in the field of the medical physics, including, the Sylvia Sorkin-Greenfield Award, The Farrington Daniels Award, and the Sylvia Fedoruk Award. In 2004, Dr. Jaffray was identified as one of Canada's Top 40 Under 40 and was recognized by The University of Western Ontario with their Young Alumni Award in 2004. His current research interests focus on the development of imaging technologies and methods with a focus on image-guided interventions, including radiation therapy, drug delivery, and surgery.



MRI in Radiation Therapy

Radiation therapy is an essential component of effective cancer control with clinical evidence supporting its use in over 50% of cancer patients at some time in their course of management [1]. While early success in radiotherapy relied almost completely on the relative sensitivity of cancer and normal tissues to achieve acceptable therapeutic ratios, the past 30 years have focused on the use of technology to spatially control the shape and intensity of dose delivered within the body. Three-dimensional (3D) imaging of the body has been the critical enabler in this pursuit.

The development of computed tomography (CT) transformed medicine with dramatic reductions in exploratory surgery, the ability to provide more accurate staging in cancer, and opening the frontier of minimally-invasive interventions – a frontier that radiation therapy was perfectly positioned to explore. It is important to note that the same advances in computing that were enabling CT were at the same time advancing the computation of dose in 2D or 3D volumes for more accurate delivery of dose. The reproducibility, geometric accuracy, and common physics of CT and radiation therapy dose calculation precipitated a period of accelerated innovation in the field of radiotherapy. In many ways, CT was an ideal imaging partner for radiation therapy treatment planning – quantitative Hounsfield Units (HU), geometric accuracy, large field-of-view (FOV), reasonable cost, reliability, and a large bore to tolerate immobilization devices. It was almost too easy.

The 1970s was the decade that also heralded the advancement of nuclear magnetic resonance imaging techniques that not only generated high contrast images of the human body, but also promised to classify cancer tissues according to their proton relaxation characteristics [2, 4]. Despite the promise MR offered for use in targeting radiation therapy [3] adoption has been remarkably slow with MR-simulation installations gradually emerging in the early 2000s [5] and momentum only starting to build in earnest in the past five years [6].

This volume of MReadings highlights the ‘coming of age’ of MR imaging in radiation therapy where MR imaging’s remarkable flexibility and scope of impact is becoming undeniable. The articles in this volume and the trends in the broader literature make it clear that MR will be more than a replacement for CT in radiation therapy. Investing in MR as a means to simply improve the quality of images and assure targeting of disease while avoiding normal tissue is attractive but not sufficiently compelling to overcome the barriers to adoption. The community is clearly looking for much more. They want MR to automate delineation of disease, non-invasively assess radiosensitivity, provide early measures of response, auto-delineate normal tissues for

avoidance, and to do so with a high degree of certainty regardless of motion or context, including in the presence of an intensity modulating beam of ionizing radiation. This isn’t unreasonable – radiotherapy is a highly effective curative therapy and we need to bring as much as possible to the process of treatment design and delivery to ensure we maximize the likelihood of a successful outcome for each patient.

As highlighted in the articles contained in this volume, MR is unmatched in its flexibility and seemingly unlimited capacity to extract new and impactful information about the normal and disease processes in the body. Beyond a doubt, MR imaging science and technology will continue to evolve into the foreseeable future, bringing even greater specificity and additional measures of the underlying biology. For these advances to bring real impact to patients receiving radiation therapy, the community needs to work closely with our industry partners to establish the foundational elements of MR in radiation therapy. We need to build the pipeline that makes MR have the robustness of CT while delivering so much more. This requires serious focus, investment and collaboration.

The industry needs to seriously engage in understanding the needs of radiotherapy and demonstrate commitment. The traditional approach of radiotherapy receiving ‘hand-me-down’ technology from other higher priority sectors of the MR industry needs to stop. The history of MR in radiotherapy is littered with token investments that seemed like ‘quick wins’ but resulted in half-baked ‘solutions’ that were often abandoned. The recent developments in MR-simulation and MR-guided radiotherapy systems demonstrate a much higher level of commitment than ever seen before and this is extremely exciting, but it remains to be seen just how committed the MR-imaging partners are to fully leveraging the underlying MR technology in these endeavors [7]. In fact, MR-guided RT systems are likely to be quite limited in the amount of MR imaging functionality released clinically for the foreseeable future.

The radiation oncologists, medical physicists, and radiotherapy technologists and their communities also need to invest. The development of new MR methods and their integration into radiotherapy practice is challenging work. Technological challenges are numerous and include assuring geometric accuracy, developing robust imaging sequences, validating image analysis methods, and calculating dose based on MR images. The development of clinical research protocols to evaluate the impact of MR technologies requires oncologists to build deep expertise in the science and technology of MR – this requires significant commitment. Hybrid MR/RT technologists will be needed –

"MR is unmatched in its flexibility and seemingly unlimited capacity to extract new and impactful information about the normal and disease processes in the body."

David Jaffray

particularly in the early stages of development of these technologies – to facilitate thoughtful design of processes that are patient-centered and safe. In addition to individual commitments, the professions need to invest to build expertise and assure patient safety. To that end, the American Association of Physicists in Medicine (AAPM) has recently launched an MRI in Radiation Therapy certificate course as part of their annual meeting.

Finally, we need to look for partnerships beyond our community to deal with the deluge of MR imaging data that radiotherapy-related MR systems will produce in the future. SAR-related issues aside, MR imaging systems have the capacity to generate massive quantities of data without the dose constraints associated with X-ray based systems. Considering the value of multi-parametric sequences, multi-fraction adaptive radiotherapy, continuous monitoring for real-time tracking, it is clear that data management will be a challenge when combined with auto-segmentation, clinical decision making, re-optimization, and dose computation. Big data is often characterized

by the four V's – volume, variety, velocity and veracity – efforts to engage computer scientists and consider emerging technologies such as artificial intelligence as a means to assure safety and quality of care for our patients should be considered a high priority for the advancement of MR in radiotherapy.

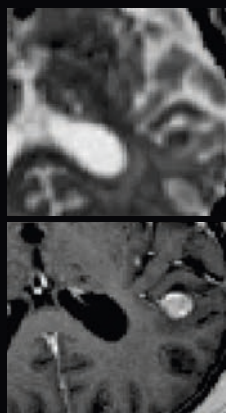
In summary, the promise of MR in radiation oncology paints a beautiful picture in the minds of clinicians, therapists, and physicists alike – a panacea of high contrast images streaming into semi-automated systems that deliver highly personalized cancer treatments for our patients. We need to be bold and commit to finishing this picture together with our partners in industry.



David A. Jaffray

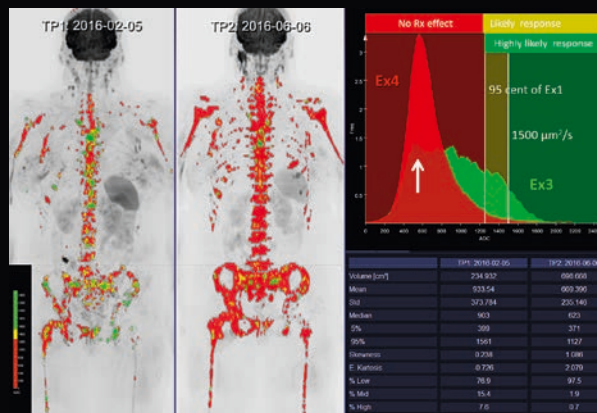
References

- 1 Atun, R., D. A. Jaffray, et al. (2015). "Expanding global access to radiotherapy." *Lancet Oncol* 16(10): 1153-1186.
- 2 Damadian, R. (1971). "Tumor Detection by Nuclear Magnetic Resonance." *Science* 181: 1151-1153.
- 3 Fraass, B. A., D. L. McShan, et al. (1987). "Integration of magnetic resonance imaging into radiation therapy treatment planning: I. Technical considerations." *Int J Radiat Oncol Biol Phys* 13(12): 1897-1908.
- 4 Lauterbur, P. (1973). "Image Formation by Induced Local Interactions: Examples Employing Nuclear Magnet Resonance." *Nature* 242: 190-191.
- 5 Mah, D., M. Steckner, et al. (2002). "Characteristics and quality assurance of a dedicated open 0.23 T MRI for radiation therapy simulation." *Medical Physics* 29: 2541.
- 6 Menard, C. and U. van der Heide (2014). "Introduction: Systems for magnetic resonance image guided radiation therapy." *Semin Radiat Oncol* 24(3): 192.
- 7 Menard, C. and U. A. van der Heide (2014). "Introduction: Magnetic resonance imaging comes of age in radiation oncology." *Semin Radiat Oncol* 24(3): 149-150.



22

Perfusion and diffusion changes in brain metastases treated with stereotactic radiosurgery



48

Observing endocrine therapy resistance in metastatic breast cancer with whole-body MRI



60

Slice-specific shimming with BioMatrix SliceAdjust¹

Editorial Comment

2 MRI in Radiation Therapy

David A. Jaffray, Princess Margaret Cancer Centre, Toronto, Canada

Radiation Therapy

6 MRI in Head and Neck Radiotherapy Planning

Houda Bahig, et al., Centre Hospitalier de l'Université de Montréal, Montreal, Quebec, Canada

12 Optimizing Fiducial Markers for MRI-based Radiotherapy

Ingemar Näslund, et al., Karolinska Institutet, Stockholm, Sweden

15 Performing Gynecologic Brachytherapy in the Medical Innovation Technical Expert Center

Lia Verhoef, et al., Department of Radiation Oncology, Radboud University Medical Center, Nijmegen, the Netherlands

20 Early Measures of Perfusion and Diffusion Changes Using a Standardized Analysis Platform Evaluated in Brain Metastases Treated with Stereotactic Radiosurgery

Catherine Coolens, Princess Margaret Cancer Centre and University Health Network, University of Toronto, Toronto, ON, Canada

26 Integration of Diffusion-Weighted Imaging / Diffusion Tensor Imaging into Radiation Therapy Treatment Planning of Brain Tumors

Tong Zhu, et al., University of North Carolina at Chapel Hill, NC, USA

32 Initial Clinical Experience Utilizing 4D-MRI for Radiation Treatment Planning

Eric S. Paulson, et al., Medical College of Wisconsin, Milwaukee, WI, USA

Oncological Imaging

38 Metastatic Prostate Cancer in Practice – the MET-RADS-P Imaging Response System Using Whole-body MRI

Anwar R. Padhani, et al., Paul Strickland Scanner Centre, Northwood, Middlesex, UK

48 Observing Endocrine Therapy Resistance in Metastatic Breast Cancer with Whole-body MRI

Anwar R. Padhani, et al., Paul Strickland Scanner Centre, Northwood, Middlesex, UK

Product News

52 Whole-body Diffusion-weighted MR Image Analysis with syngo.via Frontier MR Total Tumor Load²

Robert Grimm, et al., Siemens Healthineers, Erlangen, Germany

56 Whole-body MR Image Reading and Bone Assessment with syngo.via Frontier MR Bone Scan²

Matthias Fenchel, et al., Siemens Healthineers, Erlangen, Germany

60 Magnet Homogeneity and Shimming

Mathias Blasche, et al., Siemens Healthineers, Erlangen, Germany

Meet Siemens Healthineers

68 Introducing Lars Filipsson, Business Manager MR, Leader Special Oncology Projects, Sweden and Benjamin Schmitt, Head of Collaborations & Research for Australia and New Zealand

¹ 510(k) pending. The product is not commercially available. Future availability cannot be guaranteed.

² syngo.via Frontier is for research only, not a medical device.

MRI in Head and Neck Radiotherapy Planning

Houda Bahig, M.D.¹; Karim Boudam, Ph.D.¹; David Landry, M.D.²; Edith Filion, M.D.¹; Olivier Ballivy, M.D.¹; David Roberge, M.D.¹; Jean-Charles Côté, Ph.D.¹; Phuc-Félix Nguyen-Tan, M.D.¹

¹ Department of Radiation Oncology, Centre Hospitalier de l'Université de Montréal, Montreal, Quebec, Canada

² Department of Radiology, Centre Hospitalier de l'Université de Montréal, Montreal, Quebec, Canada

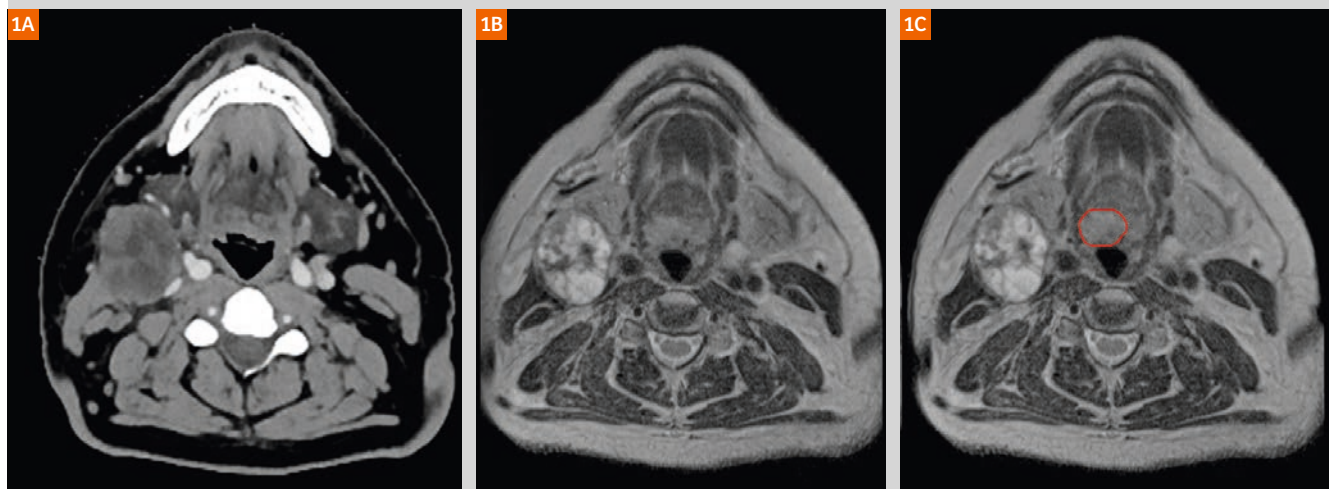
The introduction of intensity modulated radiotherapy (IMRT) as standard of care as well as the sustained improvements in image-guidance have significantly increased the precision and complexity of head and neck cancer (HNC) radiotherapy (RT) planning. As have many other institutions, the Centre Hospitalier de l'Université de Montréal (CHUM), a high-volume center for head and neck oncology, has adopted a multi-modality imaging approach for RT planning in locally advanced HNC. This approach includes routine acquisition of fluorodeoxyglucose-positron emission tomography (FDG-PET) and magnetic resonance imaging (MRI) using RT-dedicated technologies, combined with contrast-enhanced planning computed tomography (CT). While the use of IMRT allows for improved conformity of dose distribution, it requires

accurate tumor volume definition in order to prevent target-miss or unnecessary dose to organs at risk. In this report, we describe CHUM's planning MRI workflow for locally advanced HNC and we discuss the current role of MRI in HNC planning.

MRI in head and neck cancer – planning workflow at CHUM

The current approach at CHUM involves the systematic acquisition of a planning CT for dose calculation, as well as MRI sequences in treatment position for improvement of soft-tissue delineation and optimal registration with planning CT for HNC cases. This is of particular importance in HNC where differences in imaging planes and neck flexion

Figure 1: T2-weighted MRI allows to detect a base of tongue lesion that is occult on CT scan.



This patient presented with a right T1N2b squamous cell cancer of the base of tongue. **(1A)** Planning contrast-enhanced CT scan shows a large level IIA necrotic lymph node but fails to detect primary tumor; **(1B, C)** axial T2-weighted MRI sequence shows a suspicious hyperintensity at the right base of tongue measuring 1.6 x 1.3 cm and corresponding to the known primary tumor detected on fiberoptic nasopharyngoscopy.

between planning and diagnostic imaging can be major. MRI planning examinations are obtained on a RT-dedicated 70 cm open bore 1.5 Tesla system (MAGNETOM Aera, Siemens Healthcare, Erlangen, Germany). The images are acquired in treatment position with a head and neck thermoplastic mask fixed to a custom hard foam flat table insert. Due to the incompatibility between the head and neck mask and the standard head coil, surface radiofrequency coils are used [1]; this typically involves a spine array coil posteriorly and a large 18-channel flexible array coil anteriorly (Siemens Healthcare, Erlangen, Germany).

Our institutional planning MRI protocols have been adapted to RT planning through optimization of resolution and geometric distortions, resulting in scanning parameters that differ from those used in diagnostic radiology. All sequences were corrected for geometric distortion using the built in 3D correction algorithm. Parameters of the sequences currently used in our standard workflow are as follows:

- (1) **Transverse T2-weighted Turbo Spin Echo (TSE) sequence:** Repetition time (TR) / echo time (TE) 5610/80 ms, field-of-view (FOV) 19 cm, voxel resolution 0.6 mm x 0.6 mm x 3.0 mm, matrix 224 x 320 and bandwidth 191 Hz/pixel. In patients presenting dental restorations, a modified metallic artifact protocol is used, with the following parameters: TR/TE 5000/91 ms, FOV 20 cm, voxel resolution 0.6 x 0.6 x 2.0 mm, matrix 320 x 320 and bandwidth 488 Hz/pixel.
- (2) **Transverse T1-weighted TSE sequence:** TR/TE 689/23 ms, FOV 19 cm, voxel resolution 0.6 x 0.6 x 3.0 mm, matrix 224 x 320, bandwidth 200 Hz/pixel. Parameters of the modified metallic artifact protocol: TR/TE 626/9 ms, FOV 20 cm, voxel resolution 0.6 x 0.6 x 2.0 mm, matrix 320 x 320, and bandwidth 504 Hz/pixel.
- (3) **Transverse post-gadolinium T1-weighted fat saturated TSE sequence:** TR/TE 739/23 ms, FOV 19 cm, voxel resolution 0.6 x 0.6 x 3.0 mm, matrix 224 x 320, bandwidth 200 Hz/pixel. Parameters of the modified metallic artifact protocol: TR/TE 654/9 ms, FOV 20 cm, voxel resolution 0.6 x 0.6 x 2.0 mm, matrix 320 x 320 and bandwidth 504 Hz/pixel.

In addition to anatomic sequences, a focused diffusion-weighted sequence targeting gross tumor volume (GTV) is also routinely obtained before gadolinium injection, using a transverse short tau inversion recovery-echo planar imaging (STIR EPI) sequence with the following parameters: TR/TE 6900/81 ms, FOV 26 cm, voxel resolution 2.0 x 2.0 x 5.0 mm, matrix 119 x 128, bandwidth 1302 Hz/pixel. Three b-values are applied: 0, 500, 1000 s/mm², with diffusion gradient encoding in 3 orthogonal directions and combined into a trace image.

After their acquisition, MRI sequences are co-registered with the planning CT. Primary and nodal GTV delineation is performed using multimodality information from contrast and non-contrast CT, MRI as well as FDG-PET. Our

institutional protocol involves systematic formal interpretation of MRI imaging of all patients by an expert head and neck radiologist.

Advantages of MRI in HNC planning

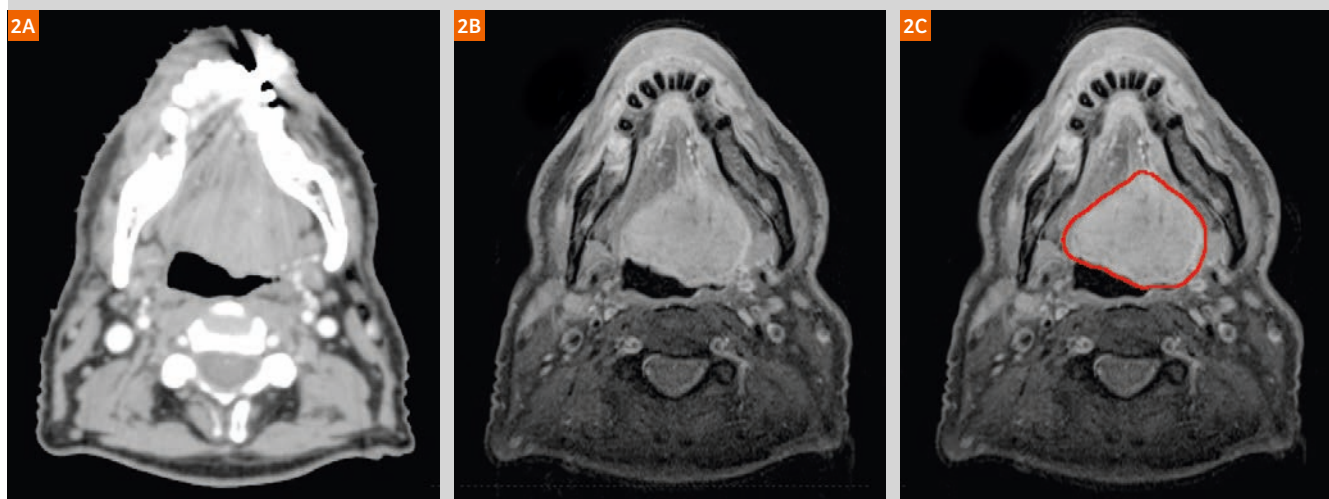
MRI is now routinely integrated in the HNC RT planning workflow [2, 3]. While planning CT provides the geometric integrity and relative electron density crucial for dose calculation, MRI co-registration to the planning CT has become indispensable for precise contouring in HNC owing to the improved soft tissue contrast. The use of an RT dedicated MRI has the advantage of increasing accessibility and allowing optimal scheduling within radiation oncology, without encroaching on diagnostic time slots. In addition, our 70 cm open bore RT MRI allows for acquisition of images in treatment position with immobilisation devices in place. For optimal RT planning imaging, major particularities of an RT dedicated MRI system include use of: (a) adapted planning MRI acquisition protocols, (b) compatible immobilisation devices, (c) flat table tops, and (d) surface coils rather than standard MRI head coils [4–6]. In addition, when looking forward to MR-only planning, in-room mobile lasers may be required. Use of planning MRI in HNC was shown to increase the precision of CT-to-MR registration compared to use of diagnostic MRI [7, 8]. In a study including 22 patients with oropharyngeal cancer, Hanvey et al. showed that MRI in treatment position was associated with a reduction of mean geometric error from 7 mm to 2 mm which translated in significant improvement of dose distribution [8]; data on the clinical impact of this improvement is still needed.

The excellent soft-tissue contrast of MRI is of particular importance in HNC where discrimination between tumor and surrounding healthy tissues is as challenging as it is crucial to avoid unnecessary dose to organs at risk. MRI has been associated with increased accuracy of GTV definition in oral cavity, oropharynx, and nasopharynx [9, 10]. In addition, MRI multi-planar imaging helps cranio-caudal tumor delimitation [11–14]. Importantly, use of morphological MRI in RT planning has been associated with reduced inter-observer variability for both GTV and organs at risk contouring [7, 12, 15]. In a prospective study of 10 patients with oropharynx cancer using multimodality assessment based on MRI, FDG-PET, and CT – MRI had the lowest inter-observer variability [16]; this is critical as delineation variability was shown to have a large impact on dose to both tumor and organs at risk [17]. International head and neck consensus guidelines, published in 2015, strongly recommend the use of MRI for RT planning for oral cavity, oropharynx, and nasopharynx tumors, as well as for delineation of several organs at risk (brainstem, spinal cord, pituitary gland, lacrimal glands, optic structures, parotid glands, and pharyngeal constrictor muscles) [18]. Precise MRI-based delineation of organs at risk is particularly useful when the GTV is in the vicinity of critical structures. Figure 1 shows an example of a patient with stage T1N2b squamous cell carcinoma of the base of tongue who

presented a radio-graphically occult primary tumor on contrast-injected CT. This tumor was however detected on a T2-weighted MRI as a suspicious heterogeneous signal. Figure 2 shows an example of a large T4aN2c squamous cell cancer of the base of tongue with anterior extension to the extrinsic muscles of tongue. As can be observed, the limits of the tumor are better defined on MRI.

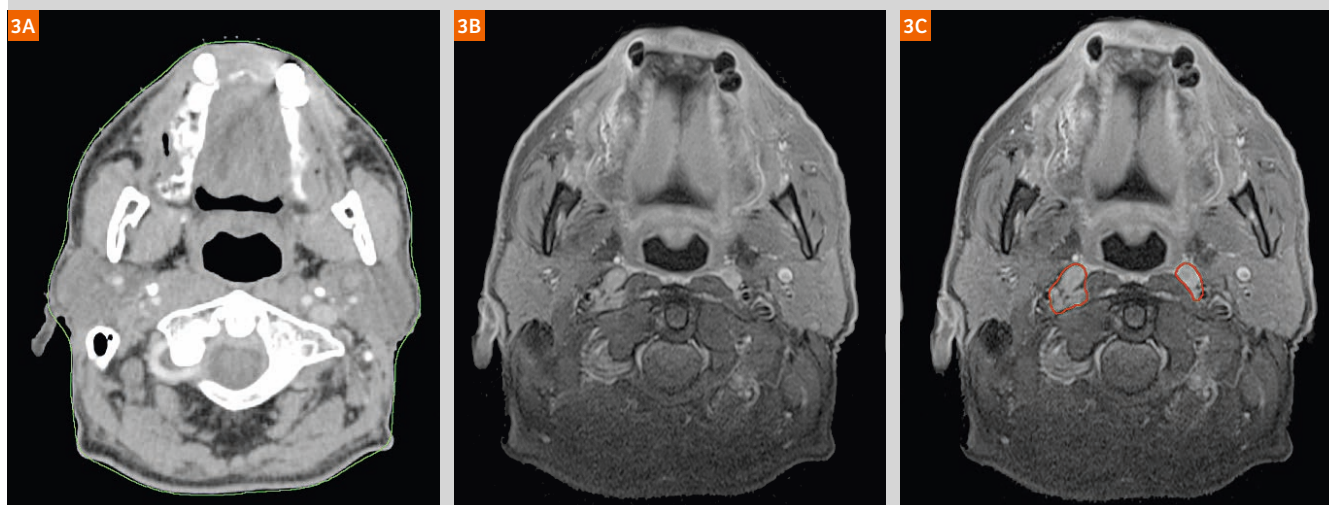
The advantage of MRI for delineation of nodal disease is more controversial [19, 20]. Anatomical MRI may however offer an advantage in the particular context of retropharyngeal lymph nodes. In a study comparing the diagnostic accuracy of CT versus MRI for detection of metastatic retropharyngeal lymph nodes in 38 patients with nasopharynx or oropharynx cancers, the two modalities were found to have similar specificity but

Figure 2: MRI improving delineation of a base of tongue tumor.



This patient presented with a left T4aN2c squamous cell cancer of the base of tongue. **(2A)** Planning contrast-enhanced CT scan shows a large base of tongue mass; **(2B, C)** axial contrast-injected T1-weighted MRI sequence shows a large 5.4 cm base of tongue lesion with anterior extension to the extrinsic muscles of the tongue; anterior, lateral and posterior limits of the tumor are better appreciated on MRI.

Figure 3: MRI improving detection and delineation of retropharyngeal lymph nodes.



This patient presented with a T2N2c squamous cell cancer of the oropharynx. While bilateral retropharyngeal lymph nodes are suspected on contrast-injected CT scan **(3A)**, gadolinium-enhanced T1-weighted MRI allows better visualisation and delineation of bilateral retropharyngeal lymph nodes **(3B, C)**.

MRI had a superior sensitivity [21]. Figure 3 shows the example of a patient presenting with a T2N2c squamous cell cancer of the oropharynx with bilateral retropharyngeal lymphadenopathies, better observed on gadolinium-enhanced T1-weighted MRI sequence.

The advantage of MRI in HNC RT planning is perhaps most eloquent in the context of base of skull tumors, where the use of MRI has been associated with not only decreased inter-observer variation [22], but also increased identification of intracranial and perineural spreads which are poorly visualized on CT scan [22–24]. In a study by Chung et al. [9] involving 258 patients with nasopharyngeal carcinoma, MRI had significantly higher detection rate of intracranial and pterygo-palatine fossa infiltrations compared to CT, which translated into both improved tumor delineation and staging. In addition, although bone cortex erosion is often better appreciated on CT, MRI may be superior for detection of skull base invasion [25]. Figure 4 shows post-operative planning CT and gadolinium-enhanced T1-weighted MRI from a patient with a partially resected nasopharyngeal adenoid cystic cancer. The images illustrate improved tumor delineation, as well as base of skull and perineural extensions.

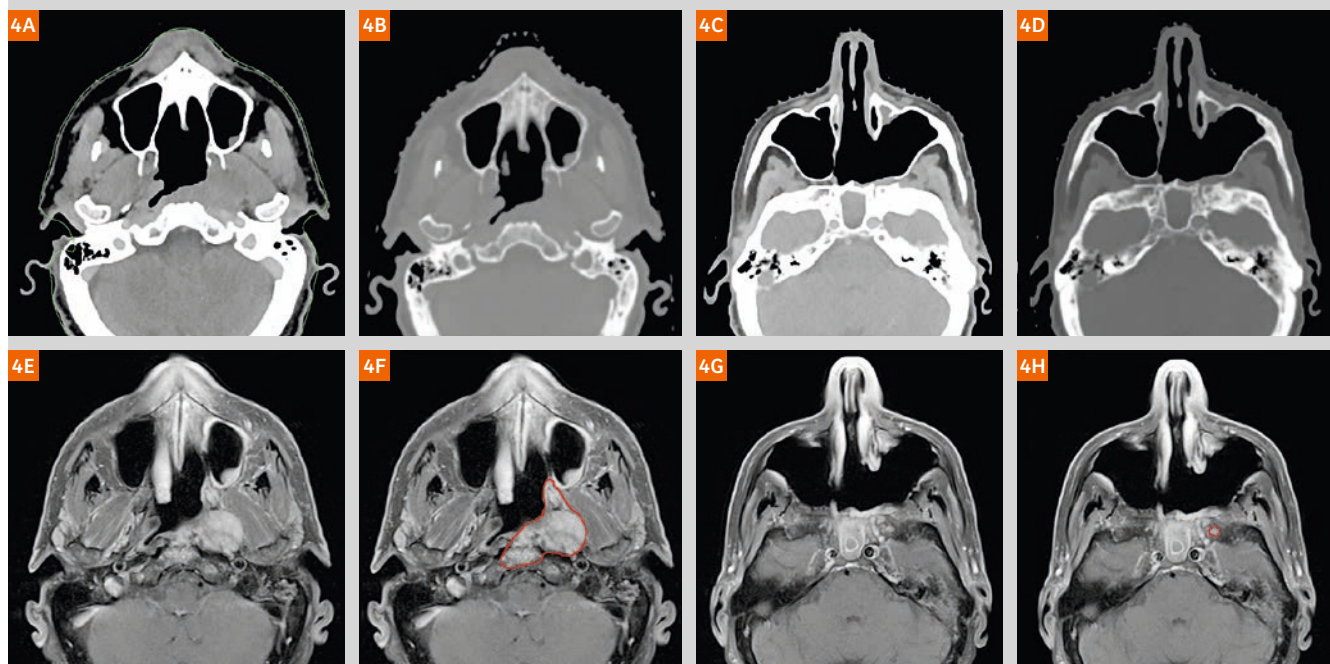
Lastly, use of MRI is particularly beneficial in patients presenting dental artifacts. Dental artifacts are a common problem in HNC RT planning, given that poor dentition

shares risk factors with HNC. High attenuation metal objects¹ such as dental restorations, surgical plates or pins can cause significant scatter artifacts and, as a consequence, can severely impair CT-based oral cavity or oropharynx primary tumor delineation [26]. Variations in magnetic field strength at the interface between dental material and soft tissues can also cause artifacts, but image quality is affected to a lesser extent [27]. Figure 5 shows planning CT and gadolinium-enhanced T1-weighted MRI (modified metal artifact protocol) from a patient with a T4N0 squamous cell cancer of the oropharynx. While the primary lesion is poorly visualized on planning CT, MRI shows a well-defined right oropharynx lesion measuring 4.4 cm with extension to the median pterygoid muscle, buccal space, soft palate, and uvula.

In conclusion, the use of MRI has become an essential part of HNC RT planning owing to the increased accuracy of co-registration with planning CT and improved tumor and organs at risk delineation, particularly for oral cavity, oropharynx, and skull base sites. However, planning MRI

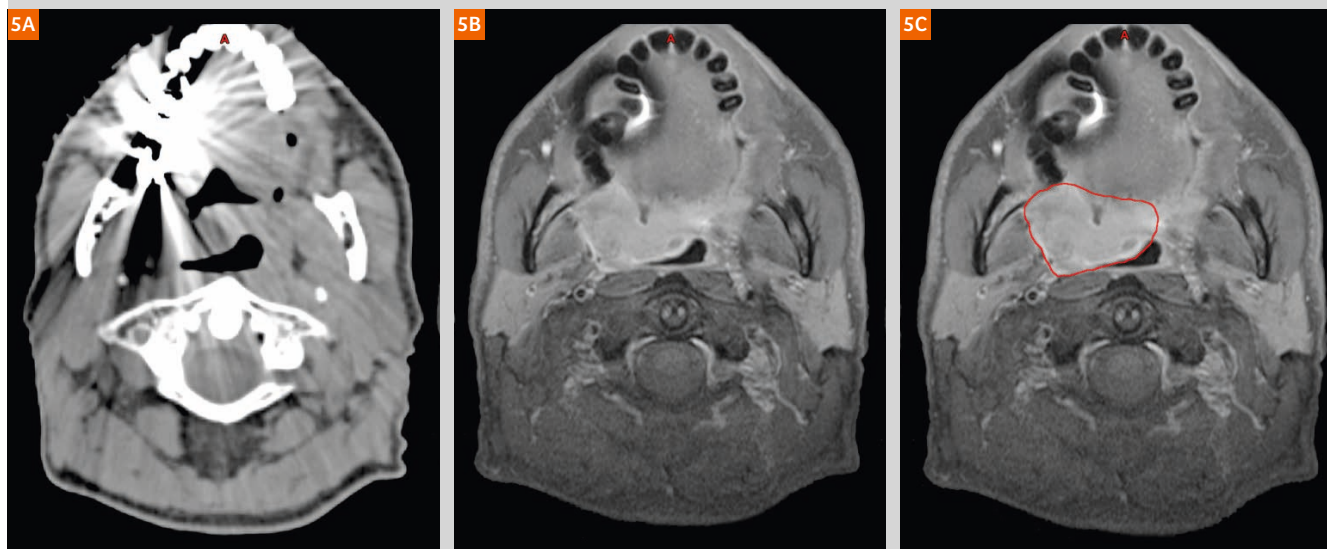
¹ The MRI restrictions (if any) of the metal implant must be considered prior to patient undergoing MRI exam. MR imaging of patients with metallic implants brings specific risks. However, certain implants are approved by the governing regulatory bodies to be MR conditionally safe. For such implants, the previously mentioned warning may not be applicable. Please contact the implant manufacturer for the specific conditional information. The conditions for MR safety are the responsibility of the implant manufacturer, not of Siemens Healthcare.

Figure 4: Improved assessment of soft tissue, base of skull, and perineural invasion in a case of nasopharynx adenoid cystic cancer.



This patient presented with a left T4N0 adenoid cystic cancer of the nasopharynx with cranial nerve involvement and positive biopsy at the clivus, status post partial resection. Planning CT (4A, B) shows a post-operative left parapharyngeal residual lesion; gadolinium-enhanced T1-weighted MRI allows to better appreciate extensions to the retropharynx, medial and lateral pterygoid plates, and clivus (4E, F), as well as perineural dissemination along extracranial V3 path (4G, H).

Figure 5: MRI improves oropharyngeal tumor delineation in a patient with important artifacts secondary to dental amalgams.



This patient presented with a right T4N0 squamous cell cancer of the oropharynx that can hardly be seen on planning CT due to important dental artifacts (5A); on T1-weighted MRI, a well delineated 4.4 cm oropharynx lesion, invading the right median pterygoid muscle, joining the right buccal space and extending to the soft palate and uvula is demonstrated (5C, D).

remains associated with several challenges including the management of geometric distortions, the need for MRI compatible immobilisation devices that maintain image-quality, the prolonged time of acquisition, and the increased use of resources. In addition, there remains uncertainty as to which imaging modality is closest to ground-truth. Considering the low concordance between CT-, FDG-PET-, and MRI-based delineations [22], MRI currently remains a complementary imaging modality to be used in combination with FDG-PET and physical examination for safe target volume delineation. Synthetic CT solutions, deriving relative electronic density data from MRI imaging, are currently being evaluated at the CHUM and, in the upcoming years, will likely lead to a more widespread adoption of MR-based workflow in HNC [28–31]. In addition, the potential value of functional MRI in HNC radiotherapy for predicting tumor response and spatiotemporal mapping of radioresistant tumor areas is currently under investigation [25, 32–35]. With the emergence of more robust data on functional imaging biomarkers, diffusion-weighted and dynamic contrast-enhanced MRI may become crucial tools to the promising avenues of dose painting and adaptive radiotherapy.

References

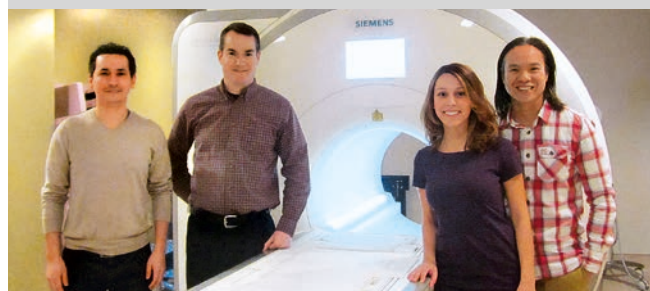
- 1 Ahmed M, Schmidt M, Sohaib A, Kong C, Burke K, Richardson C, et al. The value of magnetic resonance imaging in target volume delineation of base of tongue tumours—a study using flexible surface coils. *Radiation therapy and oncology : journal of the European Society for Therapeutic Radiology and Oncology*. 2010;94(2):161-7.
- 2 Khoo VS, Joon DL. New developments in MRI for target volume delineation in radiotherapy. *The British journal of radiology*. 2006;79 Spec No 1:S2-15.
- 3 Dirix P, Haustermans K, Vandecaveye V. The value of magnetic resonance imaging for radiotherapy planning. *Seminars in radiation oncology*. 2014;24(3):151-9.
- 4 Paulson ES, Erickson B, Schultz C, Allen Li X. Comprehensive MRI simulation methodology using a dedicated MRI scanner in radiation oncology for external beam radiation treatment planning. *Medical physics*. 2015;42(1):28-39.
- 5 Schmidt MA, Payne GS. Radiotherapy planning using MRI. *Physics in medicine and biology*. 2015;60(22):R323-61.
- 6 Metcalfe P, Liney GP, Holloway L, Walker A, Barton M, Delaney GP, et al. The potential for an enhanced role for MRI in radiation-therapy treatment planning. *Technology in cancer research & treatment*. 2013;12(5):429-46.
- 7 Prestwich RJ, Sykes J, Carey B, Sen M, Dyker KE, Scarsbrook AF. Improving target definition for head and neck radiotherapy: a place for magnetic resonance imaging and 18-fluoride fluorodeoxyglucose positron emission tomography? *Clinical oncology (Royal College of Radiologists (Great Britain))*. 2012;24(8):577-89.
- 8 Hanvey S, McJury M, Tho LM, Glegg M, Thomson M, Grose D, et al. The influence of MRI scan position on patients with oropharyngeal cancer undergoing radical radiotherapy. *Radiation oncology (London, England)*. 2013;8:129.
- 9 Chung NN, Ting LL, Hsu WC, Lui LT, Wang PM. Impact of magnetic resonance imaging versus CT on nasopharyngeal carcinoma: primary tumor target delineation for radiotherapy. *Head & neck*. 2004;26(3):241-6.
- 10 Weber AL, Romo L, Hashmi S. Malignant tumors of the oral cavity and oropharynx: clinical, pathologic, and radiologic evaluation. *Neuroimaging clinics of North America*. 2003;13(3):443-64.
- 11 Emami B, Sethi A, Petruzzelli GJ. Influence of MRI on target volume delineation and IMRT planning in nasopharyngeal carcinoma.

- International journal of radiation oncology, biology, physics. 2003;57(2):481-8.
- 12 O'Daniel JC, Rosenthal DI, Garden AS, Barker JL, Ahamad A, Ang KK, et al. The effect of dental artifacts, contrast media, and experience on interobserver contouring variations in head and neck anatomy. *American journal of clinical oncology*. 2007;30(2):191-8.
 - 13 Tien RD, Robbins KT. Correlation of clinical, surgical, pathologic, and MR fat suppression results for head and neck cancer. *Head & neck*. 1992;14(4):278-84.
 - 14 Phillips CD, Gay SB, Newton RL, Levine PA. Gadolinium-enhanced MRI of tumors of the head and neck. *Head & neck*. 1990;12(4):308-15.
 - 15 Rasch C, Keus R, Pameijer FA, Koops W, de Ru V, Muller S, et al. The potential impact of CT-MRI matching on tumor volume delineation in advanced head and neck cancer. *International journal of radiation oncology, biology, physics*. 1997;39(4):841-8.
 - 16 Bird D, Scarsbrook AF, Sykes J, Ramasamy S, Subesinghe M, Carey B, et al. Multimodality imaging with CT, MR and FDG-PET for radiotherapy target volume delineation in oropharyngeal squamous cell carcinoma. *BMC cancer*. 2015;15:844.
 - 17 Rasch C, Steenbakkers R, van Herk M. Target definition in prostate, head, and neck. *Seminars in radiation oncology*. 2005;15(3):136-45.
 - 18 Brouwer CL, Steenbakkers RJ, Bourhis J, Budach W, Grau C, Gregoire V, et al. CT-based delineation of organs at risk in the head and neck region: DAHANCA, EORTC, GORTEC, HKNPCSG, NCIC CTG, NCRI, NRG Oncology and TROG consensus guidelines. *Radiotherapy and oncology: journal of the European Society for Therapeutic Radiology and Oncology*. 2015;117(1):83-90.
 - 19 Liao LJ, Lo WC, Hsu WL, Wang CT, Lai MS. Detection of cervical lymph node metastasis in head and neck cancer patients with clinically NO neck-a meta-analysis comparing different imaging modalities. *BMC cancer*. 2012;12:236.
 - 20 Sun J, Li B, Li CJ, Li Y, Su F, Gao QH, et al. Computed tomography versus magnetic resonance imaging for diagnosing cervical lymph node metastasis of head and neck cancer: a systematic review and meta-analysis. *OncoTargets and therapy*. 2015;8:1291-313.
 - 21 Kato H, Kanematsu M, Watanabe H, Mizuta K, Aoki M. Metastatic retropharyngeal lymph nodes: comparison of CT and MR imaging for diagnostic accuracy. *European journal of radiology*. 2014;83(7):1157-62.
 - 22 Thiagarajan A, Caria N, Schoder H, Iyer NG, Wolden S, Wong RJ, et al. Target volume delineation in oropharyngeal cancer: impact of PET, MRI, and physical examination. *International journal of radiation oncology, biology, physics*. 2012;83(1):220-7.
 - 23 Gandhi D, Gujar S, Mukherji SK. Magnetic resonance imaging of perineural spread of head and neck malignancies. *Topics in magnetic resonance imaging: TMRI*. 2004;15(2):79-85.
 - 24 Geets X, Daisne JF, Arcangeli S, Coche E, De Poel M, Duprez T, et al. Inter-observer variability in the delineation of pharyngo-laryngeal tumor, parotid glands and cervical spinal cord: comparison between CT-scan and MRI. *Radiotherapy and oncology: journal of the European Society for Therapeutic Radiology and Oncology*. 2005;77(1):25-31.
 - 25 Zhang SX, Han PH, Zhang GQ, Wang RH, Ge YB, Ren ZG, et al. Comparison of SPECT/CT, MRI and CT in diagnosis of skull base bone invasion in nasopharyngeal carcinoma. *Bio-medical materials and engineering*. 2014;24(1):1117-24.
 - 26 Cooper JS, Mukherji SK, Toledano AY, Beldon C, Schmalzfuss IM, Amdur R, et al. An evaluation of the variability of tumor-shape definition derived by experienced observers from CT images of supraglottic carcinomas (ACRIN protocol 6658). *International journal of radiation oncology, biology, physics*. 2007;67(4):972-5.
 - 27 Klinke T, Daboul A, Maron J, Gredes T, Puls R, Jaghsi A, et al. Artifacts in magnetic resonance imaging and computed tomography caused by dental materials. *PloS one*. 2012;7(2):e31766.
 - 28 Korhonen J, Kapanen M, Keyrilainen J, Seppala T, Tuomikoski L, Tenhunen M. Influence of MRI-based bone outline definition errors on external radiotherapy dose calculation accuracy in heterogeneous pseudo-CT images of prostate cancer patients. *Acta oncologica (Stockholm, Sweden)*. 2014;53(8):1100-6.
 - 29 Korhonen J, Kapanen M, Keyrilainen J, Seppala T, Tenhunen M. A dual model HU conversion from MRI intensity values within and outside of bone segment for MRI-based radiotherapy treatment planning of prostate cancer. *Medical physics*. 2014;41(1):011704.
 - 30 Gudur MS, Hara W, Le QT, Wang L, Ling L, Li R. A unifying probabilistic Bayesian approach to derive electron density from MRI for radiation therapy treatment planning. *Physics in medicine and biology*. 2014;59(21):6595-606.
 - 31 Hsu SH, Cao Y, Huang K, Feng M, Balter JM. Investigation of a method for generating synthetic CT models from MRI scans of the head and neck for radiation therapy. *Physics in medicine and biology*. 2013;58(23):8419-35.
 - 32 Quon H, Brizel DM. Predictive and prognostic role of functional imaging of head and neck squamous cell carcinomas. *Seminars in radiation oncology*. 2012;22(3):220-32.
 - 33 Vandecasteele V, De Keyser F, Nuyts S, Deraedt K, Dirix P, Hamaekers P, et al. Detection of head and neck squamous cell carcinoma with diffusion weighted MRI after (chemo)radiotherapy: correlation between radiologic and histopathologic findings. *International journal of radiation oncology, biology, physics*. 2007;67(4):960-71.
 - 34 Wang H, Balter J, Cao Y. Patient-induced susceptibility effect on geometric distortion of clinical brain MRI for radiation treatment planning on a 3T scanner. *Physics in medicine and biology*. 2013;58(3):465-77.
 - 35 Powell C, Schmidt M, Borri M, Koh DM, Partridge M, Riddell A, et al. Changes in functional imaging parameters following induction chemotherapy have important implications for individualised patient-based treatment regimens for advanced head and neck cancer. *Radiotherapy and oncology: journal of the European Society for Therapeutic Radiology and Oncology*. 2013;106(1):112-7.

Contact

Houda Bahig, M.D.
Radiation Oncologist

Centre Hospitalier de l'Université de Montréal
1560 Sherbrooke Street East
H2L 4M1
Montreal, QC
Canada
houda.bahig.chum@ssss.gouv.qc.ca



Optimizing Fiducial Markers for MRI-based Radiotherapy

Ingemar Näslund, M.D., Ph.D.¹; Eva Onjukka, Ph.D.²; Christian Gustafsson, MSc.^{3,4}

¹ Karolinska Institutet, Stockholm, Sweden; Naslund Medical, Huddinge, Sweden

² Department of Medical Radiation Physics, Karolinska University Hospital, Stockholm, Sweden

³ Department of Hematology, Oncology and Radiation Physics, Skåne University Hospital, Lund, Sweden

⁴ Department of Medical Physics, Lund University, Malmö, Sweden

Introduction

Radiotherapy treatment planning has in the past largely been based on information from CT images, but MR images provide a better basis for target delineation for several diagnoses, e.g. prostate, rectum, cervix, brain, and skin/throat.

A CT scan is, however, typically still required since most radiotherapy dose distribution calculations are based on the radiation absorption information extracted from the CT images.

Image registration of MRI and CT is therefore needed in order to transfer delineated structures to the CT. This, however, introduces geometric uncertainties into the treatment, since image registration seldom provides perfect results.

A reliable point of reference is needed

Implanted fiducial markers can provide reliable reference points for the registration, if they are visible on both CT and MR images.

These markers are also very valuable for the positioning of the target volume when the patient shall receive each fraction of radiotherapy, using on-board imaging with X-ray or the megavoltage treatment beam.

The first application of gold markers for tumor positioning was published in 1995 by James Balter et al. [1]. Gold markers of sufficient mass where required to be visible on the megavoltage images. The needles used to implant the markers were therefore relatively thick.

Flat-panel X-ray detectors based on amorphous silicon were developed rapidly in the early 2000s, resulting in lower dose requirements and improved image quality. By June 2004, the radiotherapy research institution Radiumhemmet at the

Figure 1: Gold Anchor to the left compared to traditional marker.



Figure 2: A piece of pork loin, a salted (cured) and slightly smoked cut of pork with several Gold Anchors with different percentage contents of iron.

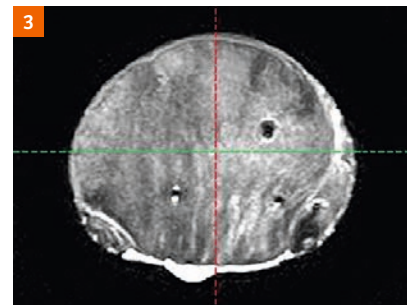


Figure 3: MRI of the pork loin with two markers of 0.5% and one of 2.5% iron content.

Karolinska University Hospital in Stockholm had already begun using On-Board Imaging with gold markers after installing Varian's very first linear accelerators with an integrated X-ray (kV) imaging system.

Modern kV imaging allows smaller gold markers to be used for patient positioning. This led to the development of the Gold Anchor® marker (www.GoldAnchorMarker.com).

Traditional fiducial markers:

- are preloaded in relatively thick needles, typically 17 or 18 gauge (outer diameter of 1.5 and 1.3 mm respectively), which can cause patient discomfort and complications related to the implantation such as pneumothorax, bleeding, infection, and seeding of cancer cells; and
- can move in the needle tract after implantation since the marker diameter is smaller than that of the needle tract caused during implantation – many medical teams therefore wait approximately 1–2 weeks after the implantation of the marker before proceeding, e.g. with CT or MRI for dose planning, to allow time for the marker to settle in and stabilize in the tissue.

In comparison, the Gold Anchor fiducial markers:

- are made of an alloy of pure gold and 0.5% pure iron, which improves the MRI visibility;
- are preloaded in industry leading thin needles, 20, 22 or 25 gauge (outer diameter of 0.9, 0.7, and 0.5 mm respectively), which reduce the risk of patient discomfort and complications related to the implantation; and
- are very stable in the tissue immediately after implantation since the marker can expand to a slightly larger size than the needle diameter after implantation and anchor directly.

Development through collaboration

More and more radiotherapy clinics are acquiring their own MR systems, adapted to their needs, providing them with new possibilities to develop tailored cancer treatments and follow-ups of treatment results. The patient needs to be scanned in treatment position with any relevant fixation devices, and image sequences are chosen to minimize geometric distortion. Plotted tumor areas are transferred to CT images which are used as a basis for treatment planning. Registering the images and daily setup is made easier and safer by using fiducial markers that are visible on both the CT and the MRI images. Currently the markers are clearly visible on MR gradient echo based T1-weighted images, but not on T2-weighted images, which are turbo spin echo

based and used for tumor delineation. Thus, a total of three image series are needed for the treatment planning.

Today, most Swedish university hospitals have MRI scanners dedicated to radiotherapy and more purchases are planned. There is thus a great need to optimize this modality for use in radiotherapy.

A national initiative, *Gentle Radiotherapy*, is currently developing methods to plan radiotherapy based solely on MRI images. The idea is also that companies involved should be able to commercialize the technology.

In this presentation we focus on a collaboration between Karolinska University Hospital in Stockholm, Sahlgrenska University Hospital in Gothenburg, Siemens Healthcare and Naslund Medical in Stockholm regarding an iron-containing gold fiducial marker. The aim was to adapt the iron content of the marker on the one hand, and the MRI sequence on the other, for reliable visualization of the markers on T2-weighted images. If successful, this would limit the number of image series needed in treatment planning, and the associated image registration uncertainties.

Visualization of markers with MRI

A range of markers of different sizes (diameter 0.28 – 0.40 mm, length 10–40 mm) and compositions (iron content 0.5–5.0%) were inserted in a piece of pork loin and imaged on a 1.5T MAGNETOM Aera and a 3T MAGNETOM Skyra (Siemens

“Gentle Radiotherapy” – Increase the chance of cure without harming the patient.
<http://www.gentleradiotherapy.se>

New research shows that magnetic resonance imaging (MRI) can describe tumor biology. This is a tool that radiologists normally use for diagnostic purposes rather than treatment plans.

Our project aims to integrate these research findings into clinical processes at all Swedish university hospitals. We also keep strict focus on efficiency to avoid increasing the costs of health care.

The consortium consists of all teaching hospitals associated with academia and 7 important industrial companies. The project is partly funded by the Swedish Innovation Agency – Vinnova.

The long-term goal is to create a large-scale national world class platform for cancer treatment.

	Aera T1	Aera T2	Skyra T1	Skyra T2
Field strength (T)	1.5	1.5	3	3
Sequence	3D VIBE	2D TSE	2D VIBE	2D TSE
Coil	Body 18*	Body 18*	Body 18	Body 18
TE (ms)	4.77	94	2.46	104
TR (ms)	7.46	12940	4.57	15990
FOV (mm)	420 x 420	448 x 448	390 x 390	220
Slice thickness (mm)	2.0	3.0	2.0	3.0
Pixel size (mm)	1.1 x 1.1	0.7 x 0.7	1.2 x 1.2	0.7 x 0.7
Bandwidth per pixel (Hz)	335	200	450	460
Slice orientation	trans	trans	trans	trans

*With coil support

Healthcare, Erlangen, Germany). All markers were inserted collapsed into a ball shape. The chosen sequences are listed in the table.

As seen in figures 4–7, showing markers with 0.5% iron contents, the markers were much more clearly visualized with T1 than with T2-weighted imaging. A greater iron content was required to reliably visualize the marker with T2, but the larger artifacts constituted a problem for image registration with markers as control points. Six members of staff assessed the performance of the markers on the T2w images with respect to visibility and artifact size/shape and found the best marker to be of 2.5% iron with a diameter of 0.28 mm and 40 mm in length.

Summary

The collaboration platform of Gentle Radiotherapy developed jointly by healthcare and industry has brought clinicians, researchers, inventors and entrepreneurs together from different places in Sweden in a stimulating collaboration.

Fiducial markers need to fulfill many, sometimes competing, criteria when used for MRI based radiotherapy treatment planning. The Gold Anchor markers are exceptionally small and are best visualized with T1 weighted gradient echo based imaging.

References

- 1 James M Balter, Howard M Sandler, Kwok Lam, Robert L Bree, Allen S Lichter, Randall K Ten Haken. Measurement of prostate movement over the course of routine radiotherapy using implanted markers. International Journal of Radiation Oncology *Biology* Physics, 31, 1, 113-118.

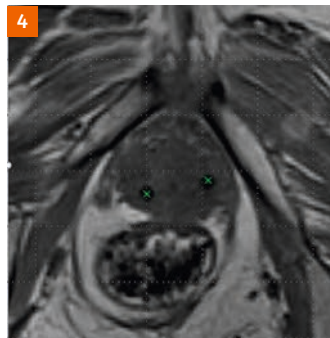


Figure 4: T1-weighted prostate 3T MRI from Karolinska with Gold Anchor 0.28 mm x 20 mm.



Figure 5: T2-weighted prostate 3T MRI from Karolinska with Gold Anchor 0.28 mm x 20 mm.

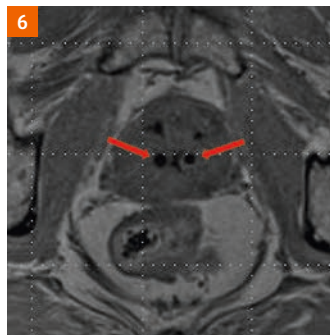


Figure 6: T1-weighted prostate 1.5T MRI from Gothenburg with Gold Anchor 0.40 mm x 20 mm.

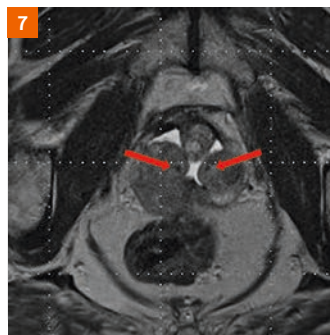


Figure 7: T2-weighted prostate 1.5T MRI from Gothenburg with Gold Anchor 0.40 mm x 20 mm.

Contact

Associate Professor Ingemar Näslund, M.D.
Karolinska Institutet, Stockholm, Sweden
Naslund Medical
Vassvagen 21
14139 Huddinge
Sweden
Ingemar.naslund@GoldAnchorMarker.com



Performing Gynecologic Brachytherapy in the Medical Innovation Technical Expert Center

Cindy P. M. Frentz¹; Ruud van Leeuwen²; Angelo van Wagendorff van Ryn³; Jurgen J. Fütterer¹; Lia Verhoef²

¹ Department of Radiology and Nuclear Medicine, Radboud University Medical Center, Nijmegen, the Netherlands

² Department of Radiation Oncology, Radboud University Medical Center, Nijmegen, the Netherlands

³ Siemens Healthineers, Siemens Healthcare Nederland B.V., The Hague, the Netherlands

Keypoints

In this article we describe our procedure of positioning brachytherapy applicators and catheters in cervical carcinoma. The procedure is performed with the support of intra operative MRI in the Medical Innovation Technical expert Center (MITeC) of the Radboud University Medical Center, Nijmegen.

Introduction

The Medical Innovation Technical expert Center (MITeC) of the Radboud University Medical Center is a multi-operation room setting utilized for minimal invasive surgical procedures supported by MRI, CT, or X-ray intervention technologies. In 2015 a wide-bore 3T MAGNETOM Skyra Combi Suite MRI scanner (Siemens Healthcare, Erlangen, Germany) was installed for MRI-guided procedures.

MR-guided adaptive brachytherapy (MRGABT) is a local radiotherapy treatment, employing after-loading techniques, that treats tumors by positioning a radioactive source, through hollow catheters placed in or near the tumor. The radioactive source is programmed to stay at pre-specified positions in the applicator and catheters, during a varying time. In this way it is possible to give a high dose to tumor tissue while minimizing the radiation dose to the vital organs in the environment of the tumor.

For Radiation Oncology, one of the great opportunities of the combination of MRI in an operating room is the possibility to perform an MRI scan directly after positioning brachytherapy catheters into a tumor in order to reposition or return to the OR if additional intervention is necessary. MRGABT can be performed based on the MR images, as soft tissue contrast allows to customize treatment plans to accurately deliver therapeutic doses to tumor tissue, while minimizing dose to the normal structures in the vicinity of the tumor, potentially resulting in fewer treatment related complications.

In our hospital, cervical carcinoma patients routinely undergo MRGABT in the MITeC since October 2015. In this article we will describe the application procedure in a patient with cervical carcinoma and the way to perform MRI-scanning in an OR setting.



Figure 1: Diagnostic sagittal T1-weighted VIBE post Gd-contrast (1A) of a cervix carcinoma in situ. Transversal T2-weighted image (1B) showing a large tumor with extensive diffusion restriction on transversal TraceW diffusion-weighted image (1C).

Procedure

For patients with locally advanced cervical carcinoma, external beam radiotherapy combined with weekly cisplatin, followed by high dose brachytherapy is the treatment of choice [6–8].

A case in clinical routine: a 50-year-old woman with a large squamous cell carcinoma of the cervix uteri. The diagnostic abdominal MRI shows a tumor of 8.8 x 10 x 11 cm that penetrates through the bladder, the urethra, the cervix, the apical vagina, and the myo- and endometrium uteri and is also fixed to the sigmoid (Fig. 1). This unresectable tumor was treated by chemo- and radiotherapy: after 25 fractions of large-field external beam radiotherapy, combined with weekly cisplatin, the remaining tumor was treated with brachytherapy. By doing it this way the tumor could be treated with a much higher dose than would have been possible with external beam radiotherapy only. The healthy tissue in the area of the tumor received a much lower dose than it would with external beam radiotherapy, as the radiation source is positioned inside the tumor.

For this treatment an applicator with guided catheters (Elekta Utrecht Interstitial Applicator Set) was used. The applicator system consists of an intra-uterine catheter and two ovoid shaped devices that allowed the placing of additional needles in the tumor (Fig. 2A) [2]. A template made in-house was used to position and adjust the needles (Fig. 2B).

As tumor sizes vary in patients the addition of a template allows the placing of extra needles outside the range of the applicator and their catheters.

The insertion of the applicator, template, and catheters was done in the OR of the MITeC under general anesthesia. The catheters were positioned in the tumor using the applicator, its ovoids, and template to guide the needles. The needles could be individually repositioned and locked for treatment. After positioning and fixing the device an MRI took place next to the OR where the catheters were placed. The patient remained under general anesthesia during the transport to the MRI-room and during the scan. Transport of the patient was easily performed using the Combi Dockable MRI table [3].

The Combi Dockable MRI table is a trolley that can be undocked from the scanner in order to transport the patient. The trolley contains a rail and a sliding table top. Connecting the MRI table to the OR table enables you to slide the table top safely on to the OR table (Fig. 3A). The table top of this MRI table will stay under the patient throughout the procedure.

The table top will be on the OR table and can easily slide on the MRI table whilst the patient remains on the table top. The rails of the table top prevent the use of a conventional spine coil. As an alternative, to receive signal from the posterior side, a 4-channel Siemens flex large coil is positioned among the rails on the MRI table before shifting the table top on it. The coils are placed along the length of

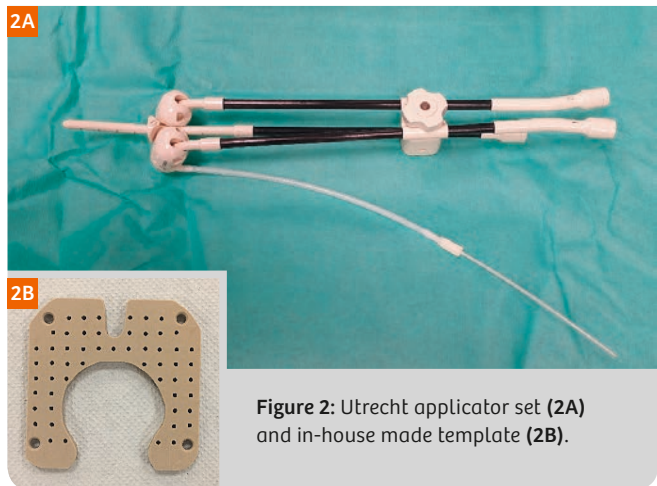


Figure 2: Utrecht applicator set (2A) and in-house made template (2B).

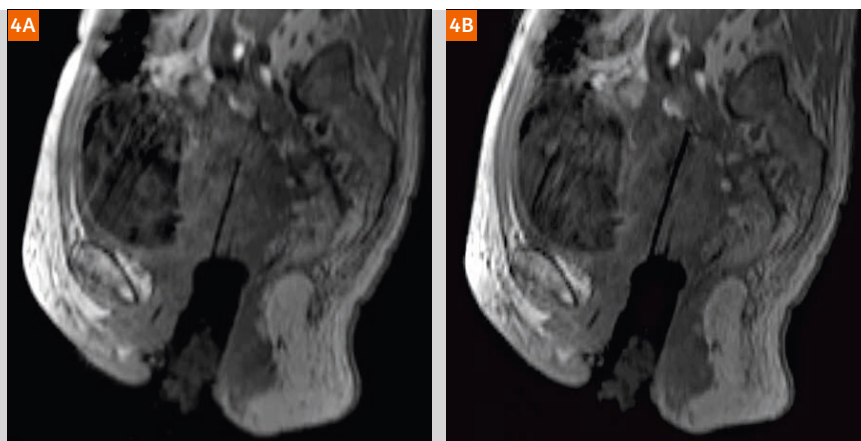


Figure 3: Patient transport from operation room (3A) to MRI room (3B) on the table top of the Combi Dockable MRI table.

the patient to facilitate full field-of-view MRI of the anatomy and catheters.

We used markers on the MRI-compatible trolley to mark the position of the 4-channel flex coil so that we could easily position the pelvic region on top of the coil. After an MRI safety check, the team transported the patient through the MRI entrance and the table was docked to the MRI-scanner.

Figure 4: Example of repositioning of a catheter. **(4A)** Sagittal reconstruction of 3D T1 VIBE: one of the catheters in situ. **(4B)** Catheter placed 15 mm deeper in the tumor.



MRI-scans were made when the patient was still under general anesthesia using MRI compatible respiratory equipment and MRI-compatible monitoring equipment to monitor patient condition during scanning. The patient was positioned in feet first position to allow a good level of respiratory control. Over the abdomen an 18-channel body coil was placed for good signal of the lower abdomen.

The scanning protocol contains a transversal 3D T1-weighted VIBE sequence (TE 2.46 ms, TR 4.57 ms, voxel size 1.2 x 1.2 x 2.0 mm, acquisition time 2:08 min) to visualize the location and depth of applicator and catheters in the cervix and tumor. On both sides of the tunnel there is enough space for adapting the catheters in a sterile way.

After repositioning the catheters the 3D T1 VIBE was repeated in order to check the location and depth (Fig. 4). After obtaining the correct position high-resolution T2 TSE sequences (TE 90 ms, TR 5020, voxel size 0.6 x 0.6 x 3.0 mm, acq. time 5:13 min) were performed in 3 directions aligned to the tip of the applicator to obtain good image contrast between normal tissue and tumor. The T2 sequences were used for contouring of the tumor and organs, and for planning of the brachytherapy dose. Normally, water filled tubes (Elekta MR line marker set) can be placed inside the applicator to have a better visualization of the applicator on the T2w images [2].

Safety issues

Because of the strong magnetic field and the radiofrequency pulses in the MRI room it is important to double-check patient and personnel for ferromagnetic and conductive materials. The patient was screened for contra-indications on the day of the intake, and again at the arrival at the OR. Before entering the MRI room there was a safety check moment planned, where personnel were checked and ferromagnetic material was removed. The applicator is MRI safe. The needles used for the positioning and replacing of the catheters are safe to use in the MRI room, but not safe to leave inside the catheters during scanning. Therefore the needles were taken out of the catheters before entering the MRI room. The template is MRI safe.

The door between the OR and the MRI room was locked. After the safety check the MRI technician unlocked the door and the patient could be transported to the MRI room. The door was automatically locked after a few minutes. To minimize risks, a minimal number of personnel were in the MR room: the anesthesiologist, the assistant anesthesiologist, and the MRI technician. All other personnel remained in the adjacent operation room or in the MRI control room.

Treatment

After the optimal placement of the applicator and catheters and the final MRI, the patient was transported back to the OR on the undocked MRI table. There she was brought to conscious, administered pain medication and transported to the recovery room. Meanwhile, dose planning was performed in the radiation oncology department. An accurate definition of the source positions relative to the anatomy is critical. Thus, evaluation of patient movements, artifacts of the applicator, and distortion should be taken into account. The bladder and bowel are organs in the direct area of the tumor. It is important for quality of life and tumor induction to spare these organs from as much radiation as possible. The optimal location of the radioactive source inside the catheters and applicator and the time they should stay inside were determined using Oncentra Brachy software (Elekta, Veenendaal, the Netherlands) [2].

After finalizing the optimal treatment planning the patient was transported to the treatment room in the department of radiation oncology, where the catheters and applicator were connected to the treatment device (Flexitron, Elekta, Veenendaal, the Netherlands) and radiation was performed [2]. After the radiation the applicator and catheters were taken out.

For effective treatment with high tumor dose and good recovery of healthy tissue the procedure of brachytherapy was carried out a total of four times during two consecutive weeks. Each time (fraction) the applicator and catheters were placed MRI-guided in the optimal way in relation to the tumor. In between the brachytherapy treatments two or three days were planned for recovery of healthy tissue [4, 5].

Figure 5: Dose plans of two sequential fractions in the same patient. The red line denotes 100% of the prescribed dose, the green line 50% of the prescribed dose, the red dotted line denotes the tumor. In an ideal situation the red line should exactly follow the red dotted line. **(5A)** Utrecht applicator plus template, 15 needles, target dose 7.4 Gray. MRI after check position and MRI guided reposition. **(5B)** Utrecht applicator and template, 5 needles; 2 free. Target dose 7.8 Gray. MRI after check position and repositioning using MRI.

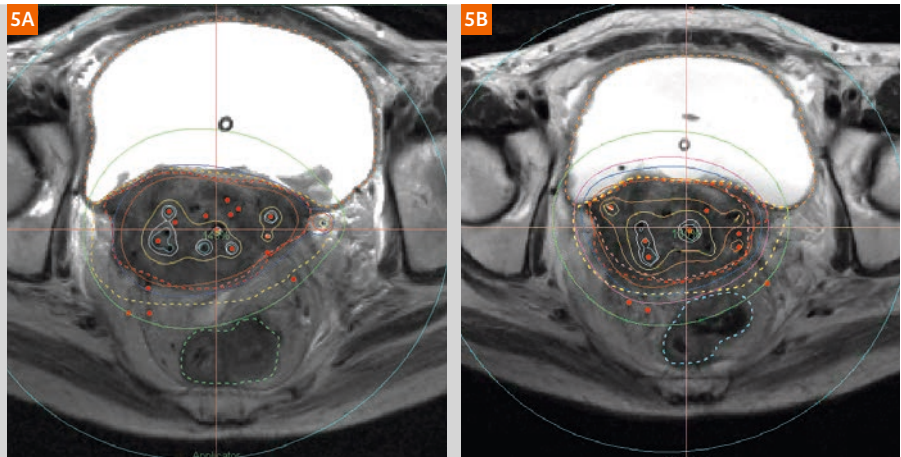
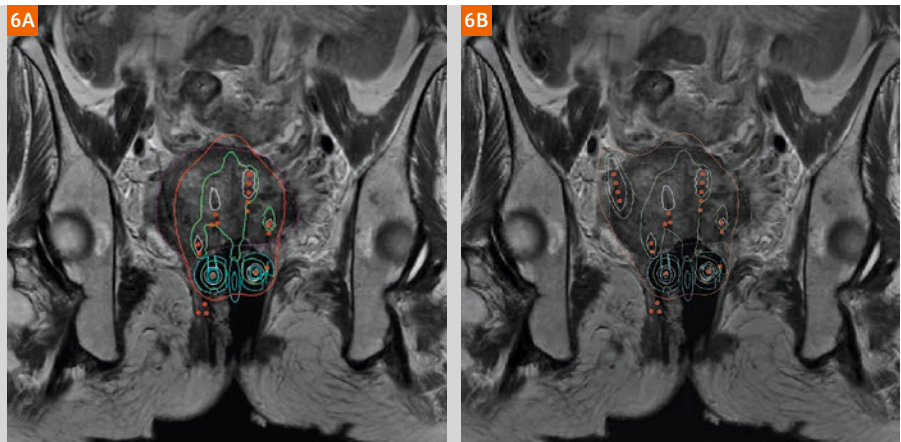


Figure 6: Dose plans on coronal T2w image in Oncentra brachy treatment planning software. Pink dotted line: tumor. Red line: 100% dose, green line: 200% dose, white line: 300% dose. Insufficient radiation dose in the outer part of the tumor (6A). Good coverage of 100% radiation dose thanks to a catheter placed free-hand in the outer part of the tumor when conventional device is not applicable for large tumors (6B).



In Figure 5 the planned dose distribution of two fractions is shown, showing high dose inside the tumor and lower dose in the surrounding organs. Panel 5A shows insufficient coverage of the tumor, especially in the ventral and right side of the tumor; panel 5B shows markedly improved coverage after MRI-guided needle adjustment.

Future perspective

In the future real-time MRI during needle shifting would be an effective way of repositioning the catheters using MRI-safe needles. Real-time imaging also allows free-hand positioning or repositioning of needles, especially in large tumors where the applicator and guided catheters are not close enough to certain parts of the tumor, resulting in under dosage. In Figure 6A you find a part of the tumor (pink dotted line) outside the 100% radiation dose (red line). In this case this part of the tumor is out of reach of the applicator. A catheter was therefore positioned free-hand in this area (Fig. 6B). This extra catheter enables you to treat this part of the tumor as it should have been. To minimize risks such as perforation, MRI-guided positioning would be a great improvement of optimal positioning of free-hand placed needles. Good visualization of an MRI safe needle needs to be available, but is not yet a clinical possibility in our hospital.

The MRI-guided procedure we described might also be applied for brachytherapy treatment in other cancer types, e.g. vagina, prostate or rectal tumors.

Conclusion and discussion

In order to prepare a patient for brachytherapy on cervix carcinoma it is good to have the availability of an MRI facility in the OR. This may offer the opportunity to effectively position and reposition applicator and catheters in a sterile way using MRI when the patient is in controlled general anesthesia. An additional advantage of the anesthesia is the reduction of motion artifacts caused by patient movement. The sliding table top of the Combi Dockable MRI table ensures easy patient transportation. Safety issues should be taken into account because of the high field strength, gradient field and radiofrequency pulses.

The option of real-time scanning during needle shifting would be an effective way of repositioning the catheters using MRI compatible needles. The treatment depends on size and position of the tumor. Different MRI compatible devices can be used. Real-time MRI can give you the ability to place or reposition needles free-hand in the tumor. This is not yet used in these procedures.

References

- 1 Joan I. Priscaandaro, James M. Balter, et al, MR-guided Gyneacological High Dose Rate (HDR) Brachytherapy, MAGNETOM Flash (S9)4/2014: 32-37.
- 2 <https://www.elekta.com/dam/jcr:bac0f2d8-1b55-43ee-bb96-2073cbf9f2eb/brachytherapy-applicator-guide.pdf#page=26>
- 3 <https://www.healthcare.siemens.nl/magnetic-resonance-imaging/mri-guided-therapy/cardiovascular-interventions/features>
- 4 www.embracestudy.dk
- 5 <https://www.embracestudy.dk/UserUpload/PublicDocuments/EmbraceProtocol.pdf>
- 6 Pötter, Richard et al.: Clinical outcome of protocol based image (MRI) guided adaptive brachytherapy combined with 3D conformal radiotherapy with or without chemotherapy in patients with locally advanced cervical cancer Radiotherapy and Oncology , Volume 100, Issue 1 , 116 – 123.
- 7 Dimopoulos J.C., Schard G., Berger D. Systematic evaluation of MRI findings in different stages of treatment of cervical cancer: potential of MRI on delineation of target, pathoanatomic structures, and organs at risk. Int J Radiat Oncol Biol Phys. 2006;64:1380–1388.
- 8 Viswanathan A.N., Dimopoulos J., Kirisits C., Berger D., Pötter R. Computed tomography versus magnetic resonance imaging-based contouring in cervical cancer brachytherapy: results of a prospective trial and preliminary guidelines for standardized contours. Int J Radiat Oncol Biol Phys. 2007;68:491–498.

Contact

Dr. C. G. Verhoef, Radiation oncologist
Department of Radiation oncology
Radboud University Medical Center

Geert Grooteplein zuid 32
6525GA Nijmegen
The Netherlands
Phone: +31(0)2436 86457
Lia.Verhoef@radboudumc.nl



Lia Verhoef



Cindy Frentz

MR-integrated workflows in Radiation Therapy for MAGNETOM Systems

We have compiled a series of study protocols and practical tips and tricks for several body sites from experts for both experts and novice users, so that everyone can benefit from each-other.

Download the booklet with tips & tricks and the .edx and .exar1 files at

www.siemens.com/magnetom-world-rt

Not for distribution in the US

Yue Qiao, Ph.D.
University of Michigan, Ann Arbor, USA

Eric Paulson, Ph.D.
Medical College of Wisconsin, Milwaukee, USA

Maja Sahlin, Ph.D.
Sahlgrenska University Hospital, Gothenburg, Sweden

Rohita Rai, MPhilSc and Gary Linzy, Ph.D.
Liverpool and Macarthur Cancer Therapy Centre, Ingham Institute for Applied Medical Research, Sydney, Australia

Cynthia Ménard, M.D., FRCPC and David Roberge, M.D., FRCPC
Centre hospitalier de l'Université de Montréal, Canada



MR-integrated Workflows in Radiation Therapy

for MAGNETOM Systems

siemens.com/magnetom-world-rt

SIEMENS
Healthineers

Early Measures of Perfusion and Diffusion Changes Using a Standardized Analysis Platform Evaluated in Brain Metastases Treated with Stereotactic Radiosurgery

Catherine Coolens, Ph.D.¹⁻⁴; Brandon Driscoll, MASC¹; Warren Foltz, Ph.D.^{1,2}; Igor Svistoun, BSc¹; Noha Sinno, MSc^{1,3}; Caroline Chung, FRCPC⁴

¹ Department of Medical Physics, Princess Margaret Cancer Centre and University Health Network, Toronto, ON, Canada

² Department of Radiation Oncology, University of Toronto, Toronto, ON, Canada

³ Department of Biomaterials and Biomedical Engineering, University of Toronto, Toronto, ON, Canada

⁴ TECHNA Institute, University Health Network, Toronto, ON, Canada

Background

Imaging systems need to perform as quantitative, precise measuring tools if they are to contribute to the goals of personalized and precision cancer medicine. This is especially true in radiation oncology where non-invasive imaging methods promise to probe the tissue/tumor for anatomical and physiological characteristics that affect both the decision to treat as well as the distribution of radiation dose to be delivered. Analysis of these imaging signals over time can also help monitor dynamic response to treatment, thereby enabling personalized management of solid tumors through treatment adaptation based on individual measurements. Quantitative imaging needs investment and adoption by industry, academia, and

healthcare providers to live up to its potential. For imaging techniques to become truly quantitative, a high level of standardization and novel quality assurance methods are needed to minimize the noise in the measurements so that even small changes in imaging characteristics associated with a patient's clinical outcome can be detected early enough to adapt and personalize treatment. For example, the emerging potential to alter the location and prescription of the applied radiation dose in response to images acquired through the course of treatment requires a high degree of reliability for the quantitative performance of the imaging performed.

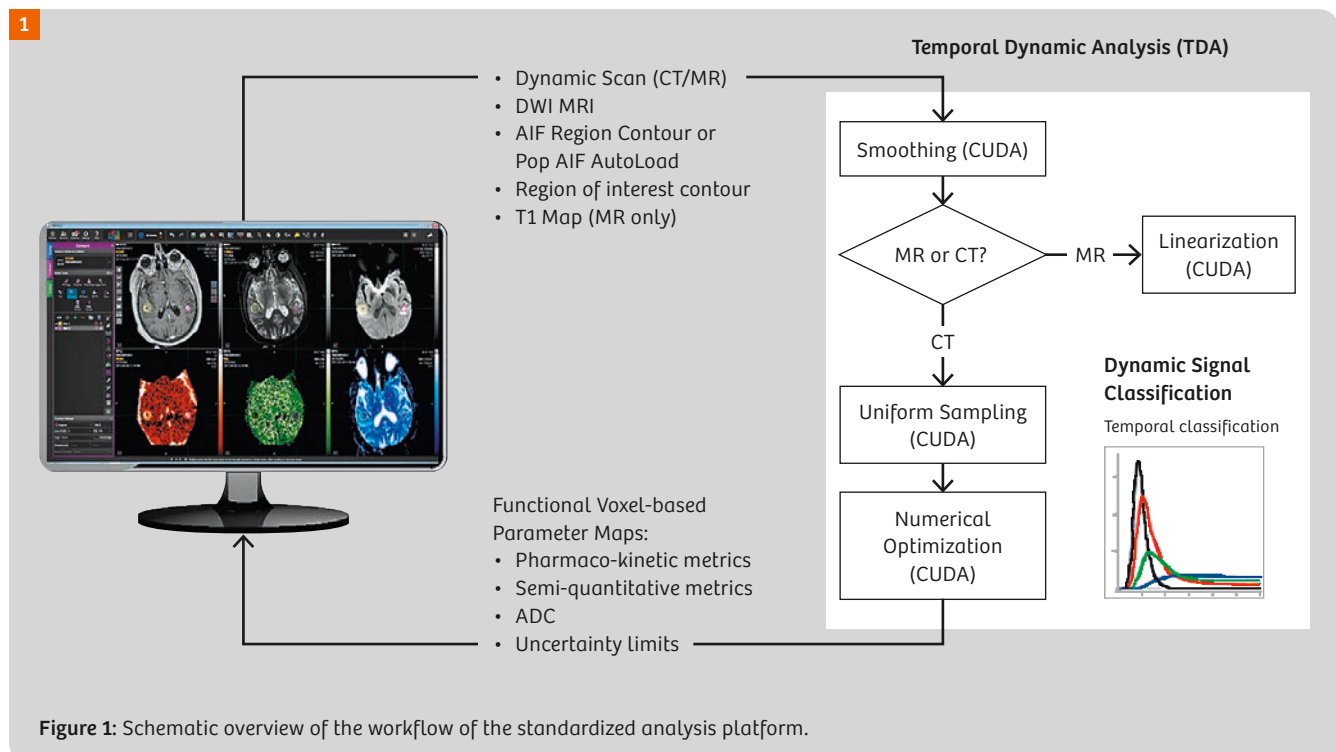


Figure 1: Schematic overview of the workflow of the standardized analysis platform.

Dynamic Contrast Enhanced (DCE) MRI is one such (functional) technique aimed at evaluating tissue and tumor perfusion parameters. DCE MRI techniques have seen a rapid growth in translation into radiation therapy clinical trials [1, 2] but DCE MRI measures of tumor vascular physiology have shown heterogeneous results across studies: this may reflect variability in the MR acquisition and analysis approaches across different studies, institutions, and even MR vendors [3–5]. Given the potential for DCE MR imaging metrics to provide early indicators of therapy-induced changes in the tumor micro-environment, it is imperative to obtain a better understanding of these imaging biomarkers to guide adaptive and potentially individualized therapy approaches in the future.

Pharmaco-kinetic modelling

The underlying process of DCE imaging is based on measuring the flow of an intravenously administered, low-molecular weight contrast agent such as Gadolinium and performing pharmaco-kinetic analysis. This involves modelling the transport of these contrast molecules between the intra-vascular and extra-vascular space. Different parameter models for contrast material exchange have been developed to quantify physiological properties of the microcirculation, such as tissue perfusion, vascular permeability, and blood volume. Most of these pharmaco-kinetic models are simplified, compartmentalized descriptions of transfer rates between intra-vascular and extra-vascular blood pools where a uniform contrast agent distribution is assumed. As such it is not surprising that the reproducibility and accuracy of model-based physiological parameters has been challenging, especially in flow-limited situations like hypoxic and necrotic tissue regions. Although the type of contrast agents used for other imaging techniques such as DCE CT and PET imaging will vary in size, osmolality, weight, etc., this fundamental analysis problem is shared by all.

Reproducibility of either DCE CT or DCE MRI alone has been low [6, 7] and output parameters from either imaging technique have not correlated well. This has been the case even in direct, *in-vivo* comparisons of the same tumor and in these situations the variability in kinetic parameters has been attributed mostly to differences in contrast agents and tumor dynamics between DCE CT and MRI. However, we hypothesized that two other factors are perhaps equally important:

- 1) Often, different kinetic models or model implementations are used for the DCE CT and MRI analysis despite both using low-molecular weight contrast agents;
- 2) notwithstanding advances in voxel-based DCE image acquisitions, analysis results are mostly reported in median values, hence losing the opportunity to investigate tumor heterogeneity and masking any correlations.

A recent 4D temporal dynamic analysis (TDA) method, which enables voxel-based, parametric analysis based on

patient-specific dynamic behaviour of contrast flow, might provide a more standardized approach for DCE MRI analysis, including its validation against DCE CT [8] given its linear relation between signal and contrast agent concentrate. It was shown that this TDA approach to DCE CT pharmacokinetic modelling provides more robust measures of change in perfusion following stereotactic radiosurgery (SRS) for brain as well as liver lesions [9].

Given that both DCE and diffusion-weighted imaging (DWI) modelling approaches probe the tumor micro-environment on a similar scale and are clearly linked in its biomechanical description, we designed a multi-modal architecture to analyse various complimentary solute transport processes in a common framework. The aim was to allow for a direct, voxel-to-voxel comparison of tumor perfusion, permeability and diffusion parameters from registered DCE CT, DCE MRI and DWI-MRI data using a shared pharmacokinetic model implementation. It was **hypothesized** that

- a) this unified platform would result in better correlations between parametric maps from DCE CT and MRI than previously reported; and that
- b) a high correlation would exist between the Apparent Diffusion Coefficient (ADC) and extravascular extracellular volume fractions, V_e , given their physiological connection describing the diffusion of water molecules inside the extravascular extracellular space.

A unified pipeline could streamline and perhaps improve even the reproducibility of individual functional imaging techniques and enable cross-validation of physiological response measures across imaging techniques and modalities. Once a shared pharmaco-kinetic platform is established, other voxel-based features of the tumor – such as cell density, or lipid and metabolites as obtained from MRI spectroscopy – could be incorporated in order to provide complementary information so that together a more comprehensive description of the tumor microenvironment can be evaluated.

Multi-functional analysis platform

In order to achieve this goal of rich, combined descriptions of the micro-environment, one must realize the amount of data associated with functional imaging techniques is significant. A typical brain perfusion CT scan can be 10 GB, which creates special viewing, processing, and data transfer requirements to enable reliable and practical integration into the clinical decision making process. Automation is therefore essential to conduct voxel-based image analysis on this scale, so we developed a platform to streamline and automate the analysis.

An overview of the platform pipeline is shown in a schematic in Figure 1. The core component is the computationally intensive TDA method [10] which was remodelled to enable GPU-based optimization on a high-throughput cluster [11] using CUDA. Briefly, this method applies a classification

scheme to each voxel, based on the temporal characteristics of the voxel's contrast enhancement over time and then iteratively improves the pharmaco-kinetic modelling based on this classification and its resulting parameter sensitivity. The Modified Tofts model [12] is commonly used in brain perfusion, based on the hypothesis of weak vascularization and increased permeability in tumors [13, 14] and this is what was used in the following evaluation in brain metastases. In addition to semi-quantitative measures, such as the integrated area under the enhancement curve ($iAUC_{90}$), the resulting functional parameters of interest were: K_{trans} , the transfer constant from the blood plasma into the extra-cellular extra-vascular space (EES); K_{ep} , the transfer constant from the EES back to the blood plasma and V_e , the extra-vascular extra-cellular volume. The haematocrit value, H_{ct} , was assumed to be 0.4 for all cases.

Additional image registration between DCE MRI and DWI-MRI modalities allowed ADC values to be calculated on the same voxels as from DCE-MRI. The directional diffusion images were averaged on a voxel-by-voxel basis to non-directional diffusion images within the TDA framework and then ADC values were calculated for each voxel by fitting the mono-

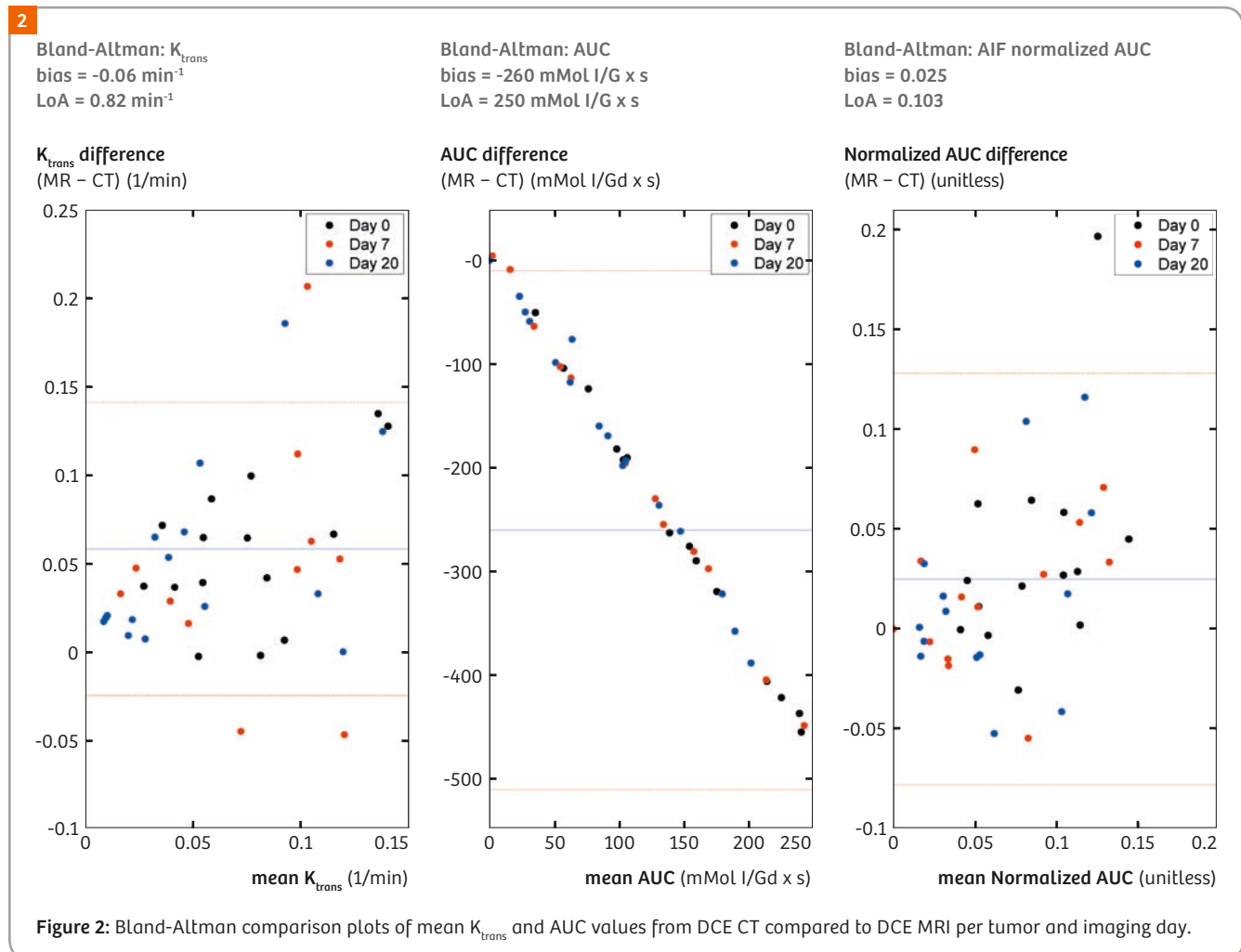
exponential model equation to four-point plots of signal intensity by using a linear least square fit algorithm [15].

A 3D Voxel Mask was created for each functional parameter as well as a separate sum of squared errors (SSE) mask to show the transport model quality-of-fit. Finally, a histogram moment analysis was done for each parameter inside the tumor mask assessing the standard deviation, skew and kurtosis of the histogram shape.

Early treatment response following SRS for brain metastases

Comparison of DCE CT to DCE MRI

Our initial clinical experience with tumor imaging biomarkers following SRS for brain metastases used volumetric DCE CT and DCE MRI in the same patients supported by this common TDA framework [16]. Patients were treated with SRS as part of REB-approved clinical trials and underwent volumetric DCE CT and DCE MRI scans at baseline, then 7 and 21 days post-SRS. TDA was used to create 3D pharmaco-kinetic parameter maps for both modalities. The arterial input function (AIF_{CT}) was chosen in the carotid artery for DCE CT and compared against a vascular input function (VIF_{CT}) in



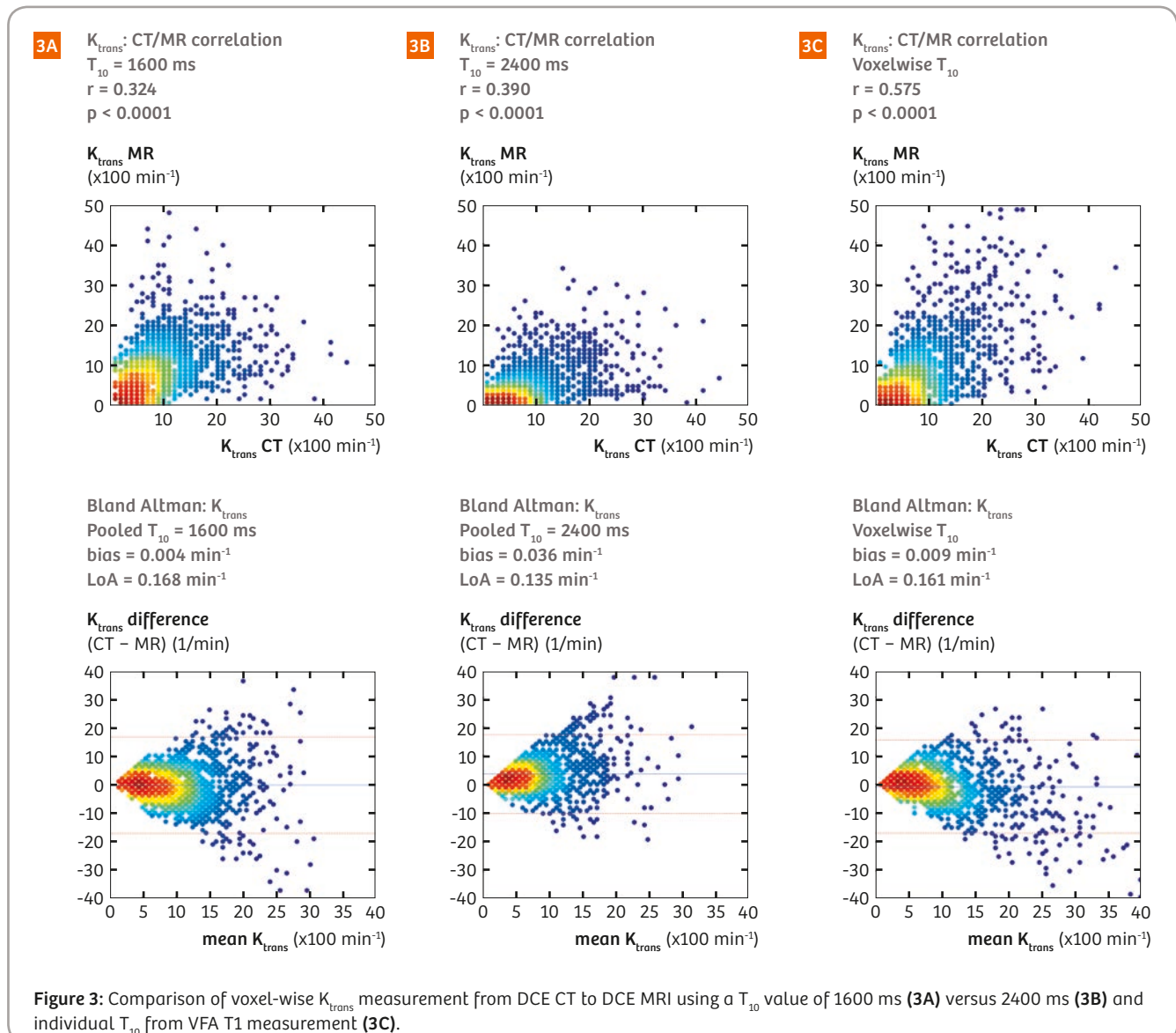
the sagittal sinus. For this study, a population-based input function (AIF_{MR}) was used for DCE MRI analysis because of variability in flip angle between patients, and to allow for a robust comparison of the impact of the analysis methodology against DCE CT.

Direct voxel-voxel Pearson's analysis showed statistically significant correlations between CT and MR which peaked at Day 7 for K_{trans} ($R = 0.74$, $P < 0.0001$, $n = 40$). The strongest correlation to DCE-CT measurements was found with DCE-MRI analysis using voxelwise T_{10} maps ($R = 0.575$, $p < 0.001$, all cases) instead of assigning a fixed T_{10} value. Comparison of histogram features demonstrated statistically significant correlations between modalities over all tumors for median K_{trans} ($R = 0.42$, $P = 0.01$), median $iAUC_{90}$ ($R = 0.55$, $P < 0.01$) and $iAUC_{90}$ skewness ($R = 0.34$, $p = 0.03$).

This is illustrated in Figures 2 and 3 with Figure 2 showing the mean tumor correlation by ways of Bland-Altman

comparison for all imaging days derived from DCE MRI and DCE CT. The correspondence is relatively scattered and indicates a slight bias towards higher K_{trans} values from MRI. Statistical significance improved significantly when comparing the voxelwise correlations taking into account tumor heterogeneity as shown in Figure 3 where no bias is present.

Based on DCE CT data, AIF and VIF appear to be interchangeable in generating similar K_{trans} values [16]. This confirms that use of individual VIF in DCE MRI analysis is a reasonable approach if it can be accurately measured. In contrast, the application of different T_{10} values impacted the K_{trans} value more dramatically and the inclusion of individualized voxel-wise pre-contrast relaxation times in the pharmacokinetic analysis is essential when evaluating parametric tumor heterogeneity [16, 17].



Correlation between ADC and DCE MRI

Statistically significant correlations were also present between ADC values and V_e from both DCE MRI and DCE CT, but a large variation was present across tumors (R^2 : 0.15–0.8). These correlations disappeared altogether when using the mean ADC values hence disregarding tumor heterogeneity as shown in Figure 4.

Summary

By analyzing contrast enhancement data from both DCE modalities in a unified and voxel-based approach, it was shown that the correlations between their parametric output values improved significantly compared to previously reported studies that used separate analysis software for both CT and MRI analysis. The high level of correlation between CT and MRI pharmacokinetic parameters supports the concept that low molecular weight contrast agents can

indeed help derive tumor permeability and perfusion heterogeneity independent of imaging modality, *provided the image analysis methods are standardised*. We also found correlations between ADC values and extravascular extracellular volume fraction parameters measured with DCE and DWI MRI when analysed using the TDA platform. This raises the potential to use this platform to further explore biophysical properties of different tumors and their microenvironments using multi-parametric imaging data.

This research indicates that more reproducible, quantitative measures of the tumor micro-environment can be extracted using DCE MRI and DCE CT with appropriate pharmacokinetic models. Being able to non-invasively interrogate the tumor micro-environment in a reliable way finally opens the possibility of using these imaging techniques to guide precision cancer medicine by directing care and adapting treatment based quantitative imaging measures of tumor response.

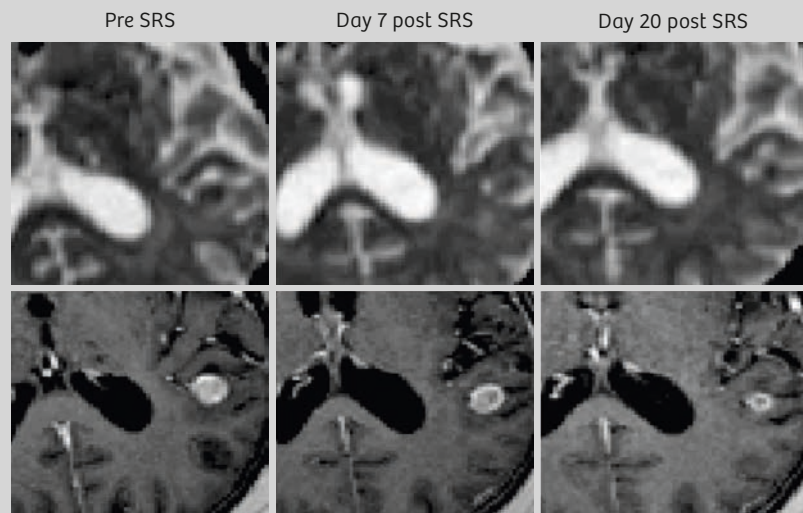
Figure 4:

(4A) T1-weighted Gad and ADC pre-treatment; Day 7 and day 20 post-SRS for a typical tumor;
(4B) Voxelwise correlation of V_e and ADC for the same tumor;
(4C) Correlation between median ADC and mean V_e values per tumor over all imaging days.

4A

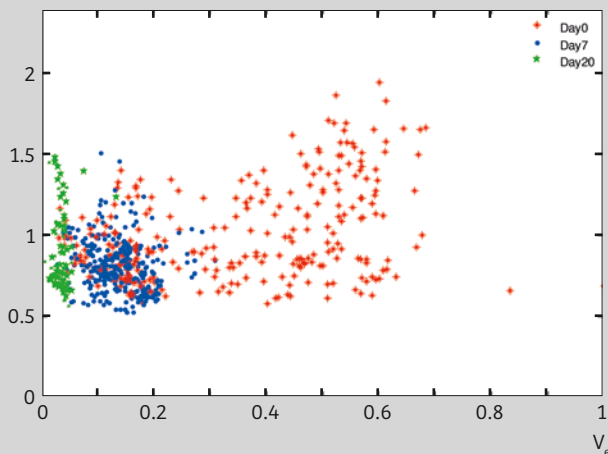
ADC

T1-Gad



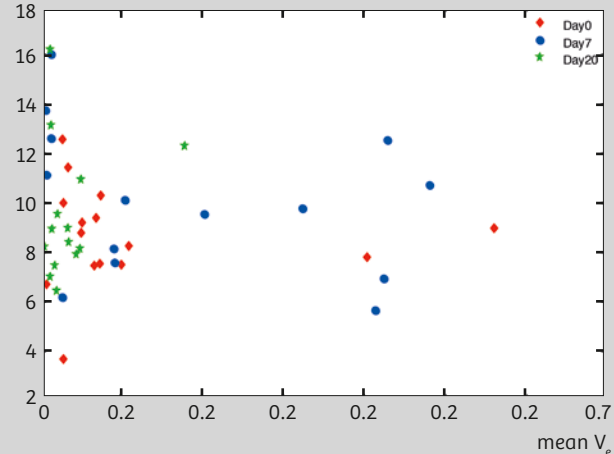
4B ADC vs V_e
 $\times 10^3$

ADC



4C mean ADC vs mean V_e
 $\times 10^4$

mean ADC



The success of the early TDA platform formed the basis of the comprehensive and multi-centre Quantitative Imaging for Personalized Cancer Management (QIPCM) program now in place at the Princess Margaret Cancer Centre. The centralised storage and archiving system that underpinned TDA was greatly expanded and QIPCM currently also provides end-to-end QA, workflow, and analysis services for imaging in clinical trials including: equipment QA, protocol development, data anonymization, QC of data during accrual, centralized data storage with remote access, software tools, and image analysis. The program currently supports approximately 20 open clinical trials run under Cancer Care Ontario as well as a number of international and industrial partners aiming to use functional imaging. The GPU version of the TDA tool is being tested internally and will be released for external trials in the next couple of months.

References

- 1 Kang TW, Kim ST, Byun HS, Jeon P, Kim K, Kim H, et al. Morphological and functional MRI, MRS, perfusion and diffusion changes after radiosurgery of brain metastasis. *European Journal of Radiology*. 2009;72(3):370-80.
- 2 Kim HR, Kim SH, Lee JJ, Seol HJ, Nam DH, Kim ST, et al. Outcome of radiosurgery for recurrent malignant gliomas: assessment of treatment response using relative cerebral blood volume. *J Neurooncol*. 2015;121(2):311-8. Epub 2014/12/10.
- 3 Goh V, Schaeffter T, Leach M. Reproducibility of Dynamic Contrast-enhanced MR Imaging: Why We Should Care. *Radiology*. 266(3):698-700. Epub 2013/02/23.
- 4 Heye T, Davenport MS, Horvath JJ, Feuerlein S, Breault SR, Bashir MR, et al. Reproducibility of Dynamic Contrast-enhanced MR Imaging. Part I. Perfusion Characteristics in the Female Pelvis by Using Multiple Computer-aided Diagnosis Perfusion Analysis Solutions. *Radiology*. 266(3):801-11. Epub 2012/12/12.
- 5 Heye T, Merkle EM, Reiner CS, Davenport MS, Horvath JJ, Feuerlein S, et al. Reproducibility of Dynamic Contrast-enhanced MR Imaging. Part II. Comparison of Intra- and Interobserver Variability with Manual Region of Interest Placement versus Semiautomatic Lesion Segmentation and Histogram Analysis. *Radiology*. 266(3):812-21. Epub 2012/12/12.
- 6 Checkley D, Tessier JJ, Kendrew J, Waterton JC, Wedge SR. Use of dynamic contrast-enhanced MRI to evaluate acute treatment with ZD6474, a VEGF signalling inhibitor, in PC-3 prostate tumours. *Br J Cancer*. 2003;89(10):1889-95. Epub 2003/11/13.
- 7 Cenic A, Nabavi DG, Craen RA, Gelb AW, Lee TY. Dynamic CT measurement of cerebral blood flow: a validation study. *AJNR Am J Neuroradiol*. 1999;20(1):63-73.
- 8 Merali Z, Wong T, Leung J, Gao MM, Mikulis D, Kassner A. Dynamic contrast-enhanced MRI and CT provide comparable measurement of blood-brain barrier permeability in a rodent stroke model. *Magnetic resonance imaging*. 2015;33(8):1007-12. Epub 2015/06/29.
- 9 Coolens C, Driscoll B, Moseley J, Brock KK, Dawson L. Feasibility of 4D perfusion CT imaging for the assessment of liver treatment response following SBRT and sorafenib. *Advances in Radiation Oncology*. 2016;1(3):194-203. Epub 7/1/2016.
- 10 Coolens C, Driscoll B, Chung C, Shek T, Gorjizadeh A, Menard C, et al. Automated voxel-based analysis of volumetric dynamic contrast-enhanced CT data improves measurement of serial changes in tumor vascular biomarkers. *Int J Radiat Oncol Biol Phys*. 2015;91(1):48-57. Epub 2014/12/03.
- 11 Svistoun I, Coolens C. Numerical Optimization Performance of a Perfusion Kinetic Modelling Algorithm using Volumetric DCE CT. *Springer Conference Proceedings Online*. 2015(SP020.4).
- 12 Tofts PS, Brix G, Buckley DL, Evelhoch JL, Henderson E, Knopp MV, et al. Estimating kinetic parameters from dynamic contrast-enhanced T(1)-weighted MRI of a diffusable tracer: standardized quantities and symbols. *J Magn Reson Imaging*. 1999;10(3):223-32.
- 13 Sourbron SP, Buckley DL. On the scope and interpretation of the Tofts models for DCE-MRI. *Magn Reson Med*. 2011;66(3):735-45. Epub 2011/03/09.
- 14 Fidler IJ, Yano S, Zhang R-d, Fujimaki T, Bucana CD. The seed and soil hypothesis: vascularisation and brain metastases. *The Lancet oncology*. 2002;3(1):53-7.
- 15 Dietrich O, Biffar A, Baur-Melnyk A, Reiser MF. Technical aspects of MR diffusion imaging of the body. *Eur J Radiol*. 2010;76(3):314-22. Epub 2010/03/20.
- 16 Coolens C, Driscoll B, Foltz W, Pellow C, Menard C, Chung C. Comparison of Voxel-Wise Tumor Perfusion Changes Measured with Dynamic Contrast-Enhanced (DCE) MRI and Volumetric DCE CT in Patients with Metastatic Brain Cancer Treated with Radiosurgery. *Tomography*. 2016;2(4):325 - 33.
- 17 Coolens C, Driscoll B, Foltz W, Chung C. SU-D-303-02: Impact of Arterial Input Function Selection and T10 Correction On DCE-MRI Tumour Response Prediction Using Compared to Volumetric DCE CT. *Med Phys*. 2015;42(6):3215. Epub 2015/07/02.

Contact

Catherine Coolens, Ph.D. CIPEM
Assistant Professor

Departments of Radiation Oncology and IBBME
Adjunct Faculty, TECHNA Institute
Radiation Medicine Program
Princess Margaret Cancer Centre and University Health Network
University of Toronto

610 University Avenue, Room 5-632
Toronto, Ontario M5G 2M9
Canada
Phone: +1 (416) 946 4501
Fax: +1 (416) 946 6566
Catherine.coolens@rmp.uhn.on.ca



Integration of Diffusion-Weighted Imaging / Diffusion Tensor Imaging into Radiation Therapy Treatment Planning of Brain Tumors

Tong Zhu, Ph.D.¹; Maurice Chojecki, MS²; Yue Cao, Ph.D.³

¹ Department of Radiation Therapy, University of North Carolina at Chapel Hill, Chapel Hill, NC, USA

² Departments of Radiation Therapy, and Biomedical Engineering, University of Michigan at Ann Arbor, Ann Arbor, MI, USA

³ Departments of Radiation Therapy, Radiology, and Biomedical Engineering, University of Michigan at Ann Arbor, Ann Arbor, MI, USA

Introduction

Radiation therapy (RT) is an important part of the standard care for most solid tumor types. The principle of modern RT is to precisely, accurately, and comfortably deliver high energy photon, electron, or heavy charged particle beams to a target volume that consists of solid tumors and high-risk microscopic invasions, while minimizing dose to nearby critical normal tissue structures.

Radiation therapy relies on modern medical imaging techniques to achieve precise target definition and dose delivery verification. Advanced MRI techniques, such as diffusion-weighted and diffusion tensor imaging (DWI and DTI), create unprecedented opportunities to quantify, both spatially and temporally, pathological changes in tumor

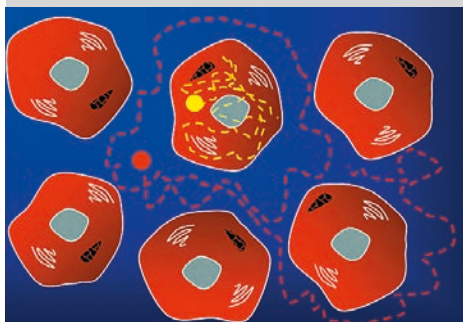
and normal brain tissue in response to RT. The quantitative measures from the diffusion MRI modalities provide a means for a paradigm-shift in radiation treatment strategy as simultaneously and dynamically assessing tumor response and normal tissue toxicity in the brain.

Here, we present two of our new approaches to integrate quantitative measures from DWI/DTI into treatment planning of radiation therapy for brain tumors.

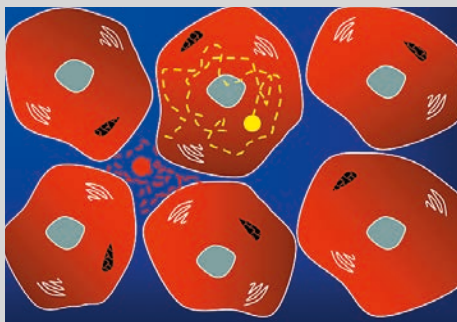
High b-value DWI for better target definition of glioblastoma

Accelerated proliferation of tumor cells is identified as one of the three main mechanisms causing failures of radiation therapy [1]. The two most fundamental hallmarks of cancer

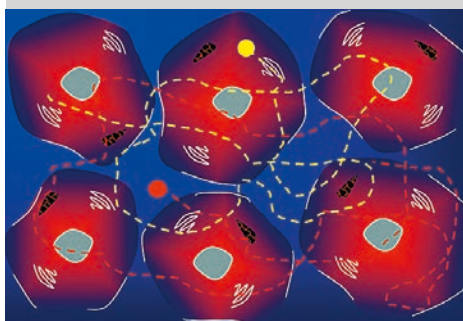
1A Normal tissue



1B Tumor (hypercellularity): diffusivity ↓



1C Necrosis (after RT): diffusivity ↑



1D Diffusion-weighted image

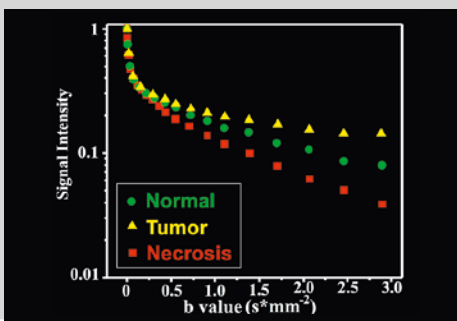


Figure 1: Illustration of diffusion MRI for radiation therapy, in terms of **(1B)** tumor detection, **(1C)** evaluation of tumor response to radiation therapy, and **(1D)** potentially increased sensitivity and specificity to normal appearing, non-contrast-enhanced parts of solid tumor using high b-value DWI. Courtesy and modified from Dr. Yaniv Assaf, Tel Aviv University

cell are its capability of deregulating the growth-promotion signals and suppress the anti-proliferation signals [2]. Using these mechanisms, cancer cells can maintain a chronic cell proliferation. Consequently, a cascade of aberrant events downstream happens, including accelerated synthesis of DNA, high demand for amino acids that are building blocks of protein and cell membranes, and ultimately high cell density as the results of this aberrant growth of cancer cells.

Diffusion is very sensitive to cell density, intra- and extra-cellular volumes, which can be used for detection of hypercellularity in tumors due to aberrant proliferation. For most solid brain tumors, water diffusion is approximately isotropic. In body temperature, free water diffusion *in vivo* is about $3 \times 10^{-6} \text{ mm}^2/\text{ms}$. With a typical b-value of 1000 s/mm^2 , clinical DWI will measure the displacement of free water molecules of 30 microns. As illustrated in Figure 1, in an image voxel of normal brain white matter tissues (Fig. 1A), intra- and extra-cellular diffusion (represented by yellow and red dots respectively) do not exchange due to the myelin sheath and both contribute to measured diffusion in DWI. In tumoral tissue, cells are highly packed with slightly increased cell size (Fig. 1B). Hypercellularity reduces extracellular diffusion dramatically and increases intracellular diffusion mildly. It leads to an overall decrease in diffusion. Radiation may damage/destroy intracellular organelles, increase cell membrane permeability, and even produce necrosis, which results in a reduction in restricted diffusion between extracellular and intracellular space (Fig. 1C), and an overall diffusion increase. Using a high b-value, fast diffusion signals will attenuate more rapidly than slow ones, the latter is largely from tumor cells due to hypercellularity and restricted diffusion (Fig. 1D).

In a recent study [3], we explored this unique characteristic of DWI with a high b-value toward detecting enhanced and non-enhanced hypercellular subvolumes of glioblastomas (GB). Glioblastoma is a highly aggressive tumor, and has high intra-tumoral heterogeneity. The standard of care for glioblastoma is resection followed by concurrent and adjuvant chemoRT with temozolomide (TMZ). Standard imaging for RT target definition includes Gd-enhanced T1-weighted and fluid attenuated inversion recovery (FLAIR) T2-weighted MRI. However, tumor heterogeneity and influence of edema and post-surgical inflammation lead to overestimation of the tumor volume by FLAIR images. DWI images with a b-value of 1000 s/mm^2 are heavily investigated in clinical research for target definition, tumor grading, and treatment assessment. However, inconsistent ADC values are often reported due to a mixture of high cellular tumor cells, edema, normal tissues, and scar tissues.

We hypothesized that *increasing b-value would improve sensitivity of DWI in detection of tumor with low diffusion due to high tumor cell densities (Figs. 1B, D) and therefore, would potentially improve the accuracy of the gross target volume definition of glioblastoma for radiation therapy.* This study applied DWIs of high b-value up to 3000 s/mm^2 to 21 patients with glioblastoma post-resection but prior to

chemoradiation. The gross target volume definition for radiation (GTV-Gd) still followed the conventional definition based on post-operative contrast-enhanced T1. Hypercellularity volume (HCV) was first determined on DWIs with a b-value = 3000 s/mm^2 within the FLAIR abnormality by using a threshold (the mean intensity plus 2 standard deviations) calculated from a volume of interest in the normal-appearing tissue most contralateral to the tumor. Furthermore, the HCV was divided into Gd-enhanced and non-enhanced components (Figs. 2A, B). Among 15 patients with post-treatment progression, 14 patients had incomplete dose coverage for the pre-treatment HCV (examples from one patient were shown on Figures 2B, C). Patients who had recurrence more rapidly had, on average, a greater percentage of recurrent GTV-Gd spatially overlapping with the pre-RT HCV than those whose recurrence came later. HCV, non-enhanced HCV and the sub-volume of HCV that was not covered by the prescription dose were all significant negative prognostic indicators for the progression free survival ($P < 0.002$, $P < 0.01$ and $P < 0.05$ respectively).

Our results suggested that, in glioblastoma, contrast-T1 imaging underestimates the gross target volume due to missing non-enhanced components and FLAIR overestimates the target volume due to edema and surgery associated inflammation. High b-value DWI could increase the sensitivity and specificity for detection of hypercellular components in glioblastoma and improve accuracy of target delineation. Due to simplicity, high b-value diffusion-weighted imaging likely makes an immediate clinical impact on radiation treatment of brain glioblastoma.

In this study, DWIs in three orthogonal directions with b-values of 1000, 2000, and 3000 s/mm^2 were acquired with a 3T MAGNETOM Skyra scanner (Siemens Healthcare, Erlangen, Germany), using the standard single-shot spin-echo echo-planar imaging sequence (ss-EPI). High b-value DWIs were used for assistance of the target delineation. Therefore, imaging parameters of the EPI sequence were carefully selected to balance between achievable geometric accuracy and sufficient signal-to-noise (SNR) level. A GRAPPA = 4 (parallel imaging factor) was chosen to reduce geometric distortion intrinsic to the EPI sequence. We then chose a voxel size with a mean spatial resolution = $1.3 \times 1.3 \times 5.2 \text{ mm}^3$ (range: [1.2–1.4], [1.2–1.4], 5.2 mm) and a mean TE/TR = 99.3/8222 ms (range: 98–105/7400–9200 ms) to obtain a reasonable SNR. Average was also used for high b-value images as 4, 3, and 2 for b = 3000, 2000, and 1000, respectively. Image acquisition for high b-value DWI in this study was quick, typically 2 to 3 minutes, and can be readily implemented in most clinical MRI scanners.

A new diffusion pulse sequence, the read-out segmentation of long variable echo trains technique (RESOLVE), further benefit the needs of radiation therapy. Compared with traditional ss-EPI, RESOLVE [4] effectively shortens echo-spacing with read-out segmentation EPI acquisitions, which leads to reductions in susceptibility and T2* artifact caused geometric distortion, blurring and signal loss. In RESOLVE-EPI, each segment readout is accompanied with

a 2D navigator. RESOLVE not only applies 2D navigators to correct the nonlinear phase variations among segmented readouts but also relies on them as quality indicators to reacquire uncorrectable data, such as signal void from pulsations of the corticospinal fluid (CSF) during the specific segment readout acquisition corresponding to that navigator. Combined with parallel imaging techniques, RESOLVE-EPI will generate high resolution DWIs with improved geometric accuracy, which can potentially improve detectability of small lesions for RT of brain tumors. Our recent experience with the RESOLVE-EPI indicates that the geometric distortion in the brain (except the first 1–2 mm from the brain surface) is unmeasurable compared to the fast spin echo based T1-weighted images.

Evaluation of radiation-induced white matter injury using an atlas-based, automated DTI tractograph analysis

Quality life for the long-term survivors with benign and low-grade brain tumors and treated by intracranial radiation therapy is important. However, RT, including partial brain RT, has been shown to cause neurocognitive

dysfunction [5–10] and affects quality of life of a substantial percentage of long-term survivors. Radiobiologic studies [6–8] have shown that radiation-induced death of neurons is minimal following clinically relevant dose. However, cognitive function is carried out by neural networks, supported by white matter (WM) pathways, rather than single cortical structures (i.e. the hippocampus). DTI combined with fiber tracking techniques allows us to assess individual fiber bundle response to radiation dose and contribution to changes in cognitive functions after RT.

The decline in executive function is one of the most common patterns of cognitive declines observed in patients with benign and low-grade cranial tumors after RT. The executive function is mainly carried out in the neural network consisting of the prefrontal functional cortical regions, such as dorsal lateral prefrontal cortex (DLPFC), and the WM fiber bundles including the inferior fronto-occipital fasciculus (IFOF). However, the common decline in executive function seems to be contradictory to the heterogeneous tumor locations of the patients, where the high doses were delivered (Fig. 3). When the network involved in the executive function is considered, it is not a surprise.

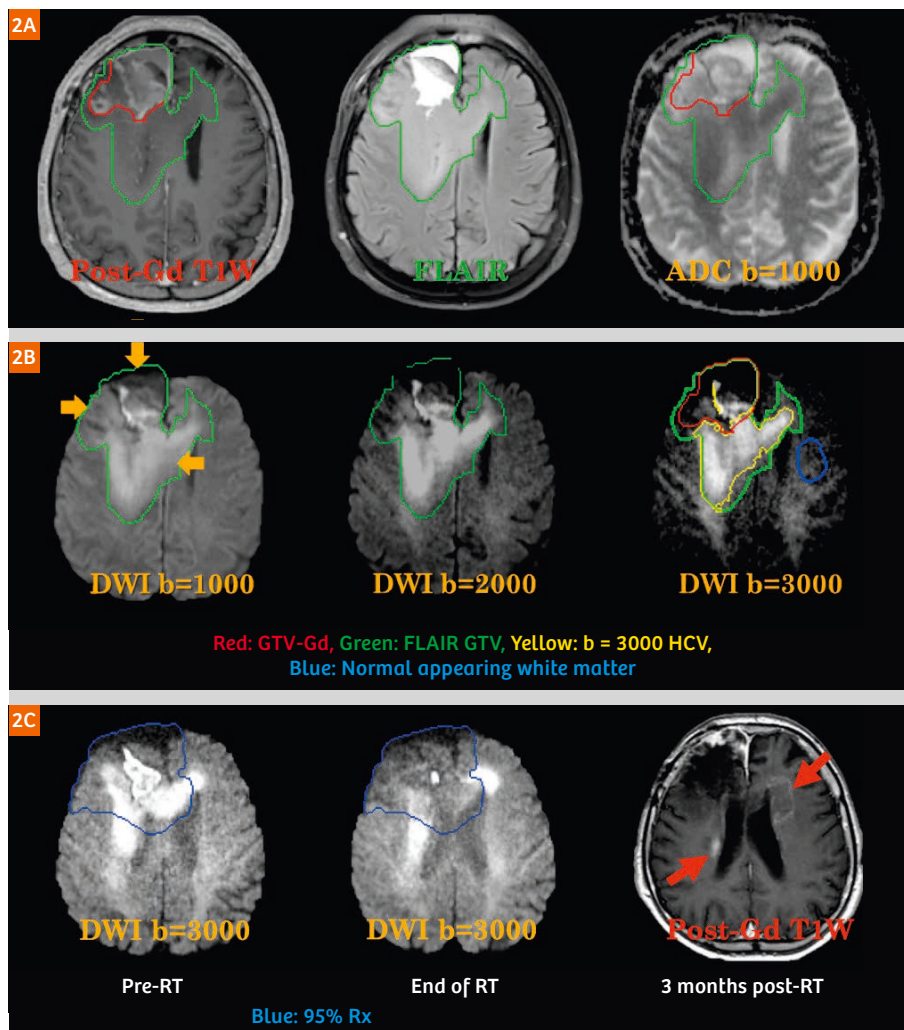


Figure 2: High b-value DWI for detection of hyper-cellularity in patients with non-contrast enhanced sub-volume of glioblastoma. **(2A)** There was no difference in depicting tumor volume between post-Gd T1 (red contour, also used as the gross target volume for RT) and conventional ADC maps acquired with a b-value of 1000 s/mm².

FLAIR images overestimated the tumor volume (green contour) due to edema. **(2B)** With a b-value of 3000 s/mm², it attenuated fast water diffusion such as those from edema and normal tissues. Contributions from slow water diffusion from high density tumor cells were enhanced (yellow contours). **(2C)** Compared to high b-value DWI images pre-RT (left column), hyper-cellular tumor tissues within volumes defined by the 95% prescription isodose line from the treatment plan for the GTV defined by the pre-treatment Gd-enhanced T1 MRI (middle column) were largely killed by radiation treatment. However, Gd-enhanced T1 of the recurrent tumors (red arrows in the right column) clearly showed large overlapping between recurrence and the sub-volumes of pre-treatment HCV that were not covered by radiation.

In a recent study [11], we hypothesized that *subject-specific radiation damage to different sections of the same WM network could result in a similar neurocognitive outcome, and WM bundles could respond to a maximum radiation dose, much like a serial structure.* To test the hypothesis, we conducted a longitudinal DTI study of 33 patients with low-grade or benign cranial tumors underwent partial brain RT. MRI scans were performed at six time points: 1–2 weeks pre-RT, 3 and 6 weeks during RT, and 1, 6, and 18 months after RT. We implemented an atlas-based, automated DTI WM tractograph analysis to segment 22 major WM bundles

of the whole brain of 33 patients from DTI data of six time points to relate longitudinal WM changes to radiation dose and specific neurocognitive outcomes. Our study found that long inter-cortical association and projection WM bundles responded to the maximum dose received by the bundles, like a typical serial structure. This type of dose response cannot be discovered without DTI and fiber tracking. Also, we found that axial diffusivity (AD) decreased progressively over time, and 20 Gy (EQD2) caused significant changes in DTI-derived measures.

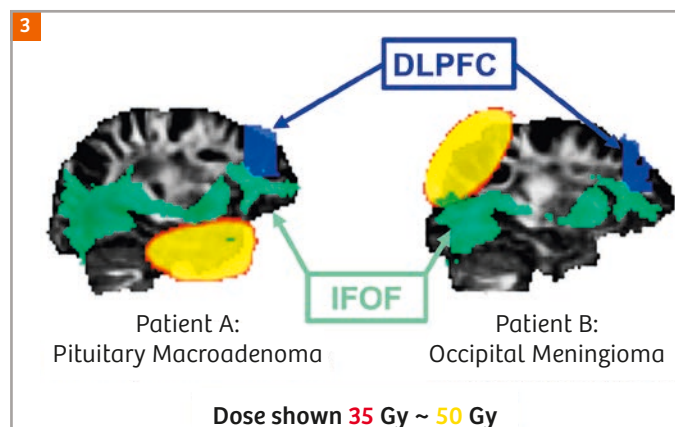


Figure 3: Typical examples of heterogeneity of primary tumor locations / high dose regions vs. common patterns of neurocognitive decline post-RT among patients with low-grade/benign cranial tumors. Both patients experienced decline in executive and long-term memory functions related to the dorsolateral prefrontal cortex (DLPFC). Both patients had high-dose regions (dose larger than 35 Gy are shown in the map with orange to bright yellow colors) distal to the DLPFC but overlapped at different sections of the inferior fronto-occipital fasciculus (IFOF), an essential part of the DLPFC neural network.

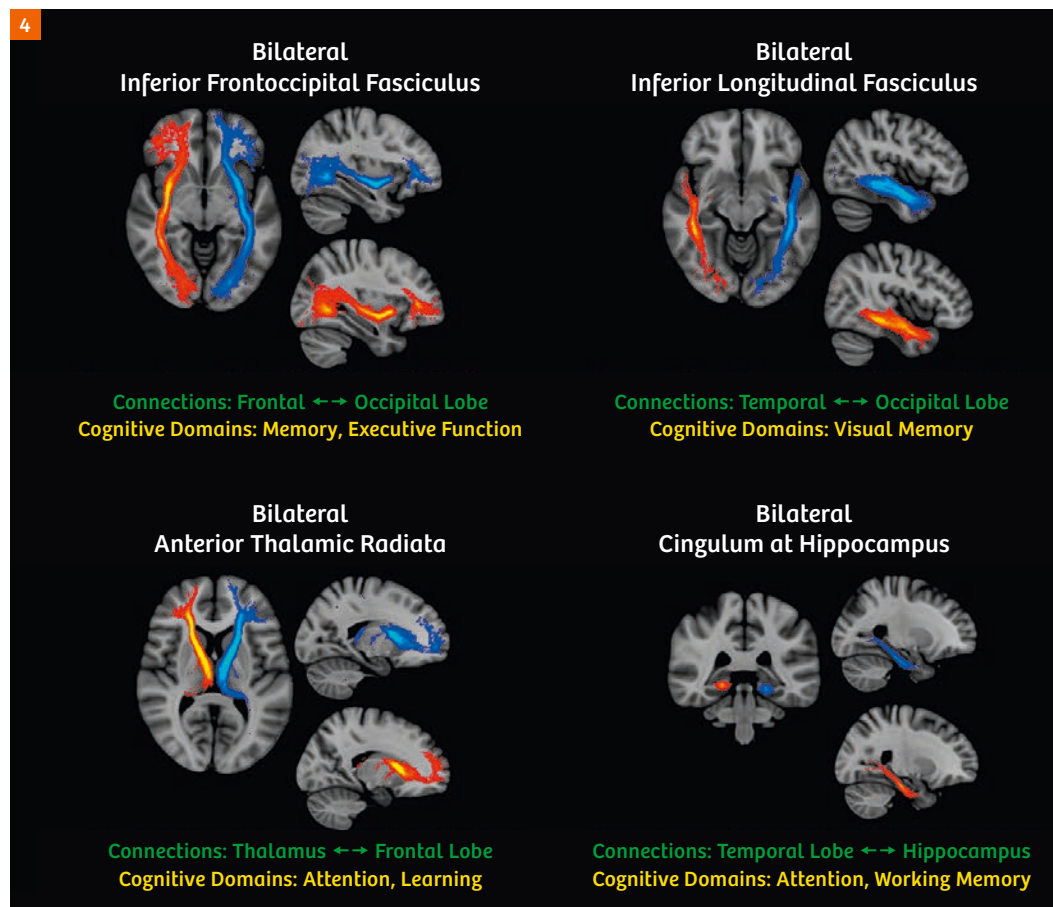


Figure 4: Examples of long inter-cortical association and projection WM fiber bundles where longitudinal changes in WM following RT significantly correlate with the maximal dose received by the bundles, with their anatomical inter-cortical connections and their known involvements in cognitive domain labelled.

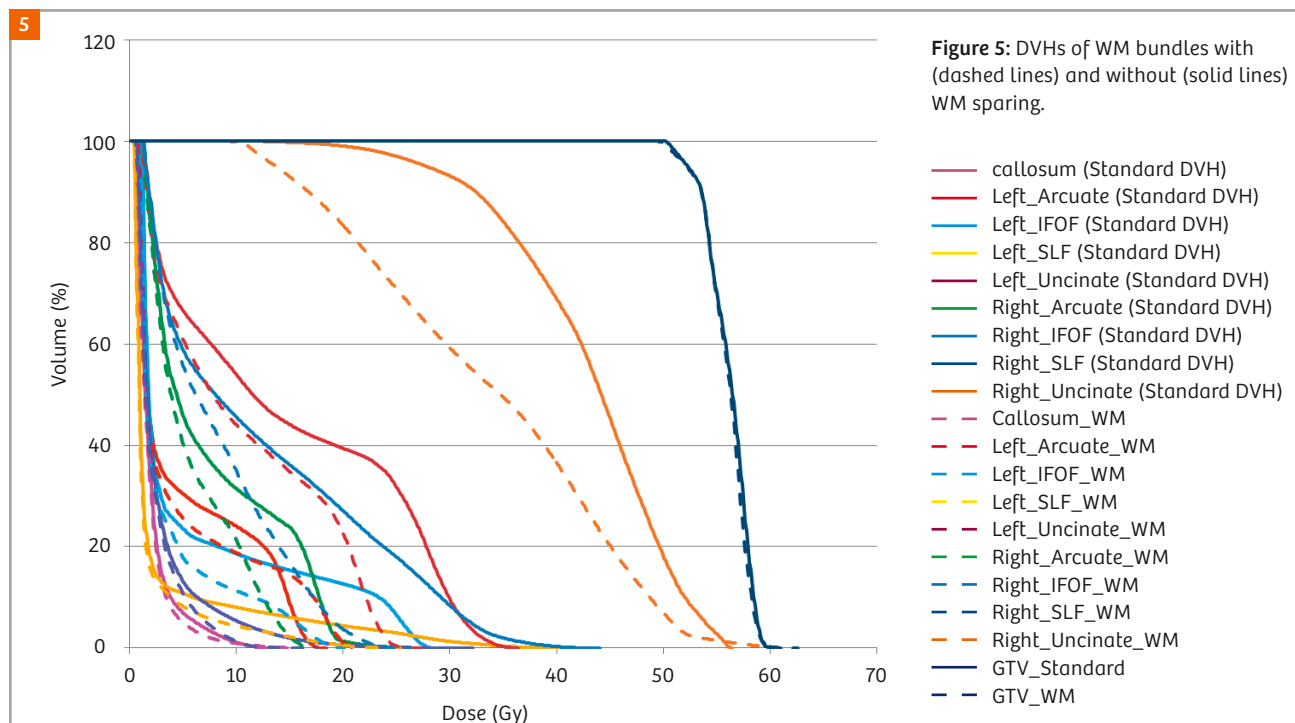
The dose response patterns observed in our study could provide a new insight on how to plan radiation doses in the long-term survivors to reserve critical cognitive functions. In current clinical practice, the guidelines [12] are only limited to spare brain stem and optic nerves/chiasm. Sparing critical white matter fibers to reserve cognitive functions is achievable by the state-of-art radiation therapy techniques, such as intensity modulated radiation therapy / volumetric modulated arc therapy (IMRT/VMAT). Several fiber bundles that show the significant dose effects in our study are known to be essential parts of neural networks for executive functions, working memory and decision making (Fig. 4). To test the feasibility of reducing the maximum dose to less than 20 Gy for key WM bundles without compromising the planned target volume (PTV) coverage, we further carried out a preliminary study of nine patients who experienced decline in executive functions post-RT. Nine WM bundles were identified with major to minor roles in the network of executive functions, including the genu of the corpus callosum (Callosum), bilateral arcuate fasciculi (Arcuate), bilateral inferior fronto-occipital fasciculi (IFOF), bilateral superior longitudinal fasciculi (SLF), as well as bilateral uncinate fasciculi (Uncinate). VMAT plans were generated, and the V20 (i.e. the percentage of volume in WM bundles receiving dose at least 20 Gy) for each bundle was calculated for plans optimized with and without WM sparing. Our results showed that PTV doses were the same with and without WM sparing. The 5 patients who had pituitary or nasal tumors, or tumors located in the anterior temporal lobe had 77% or greater of WM bundles spared with the V20 less than 5%. For the 4 patients with tumors located in the frontal lobe or the mid brain, it was

impossible to spare the ipsilateral WM bundles and the genu of corpus callosum, however sparing 22–30% of contralateral WM bundles such as the accurate fasciculus and the SLF was achieved. DVHs from treatment plans with and without WM sparing of one patient are shown in Figure 5 as examples.

A whole-brain DTI scan can be done in 3–5 minutes. An example protocol of DTI that we used on a 3T MAGNETOM Skyra scanner is as following: TR = 4600 ms and a minimized TE, resolution = $1.72 \times 1.72 \times 3.9 \text{ mm}^3$, b-value = 1000 s/mm^2 , a GRAPPA factor of 2, the number of unique diffusion-weighting directions = 20, two repeat measurements and a total scan time of 3 minutes and 40 seconds for coverage of a whole brain. To quantify the robustness of automated tractograph analysis on clinically acquired DTI data, we used the Jaccard Similarity Index (JSI) to evaluate the within-patient similarity of pairs of tracked and binarized fiber bundles at any two time points, and achieved a mean JSI of 0.85 over all WM bundles from all patients scanned on the Siemens scanner, equivalent to 90% of volume overlap of the same bundle tracked longitudinally. This indicated high repeatability of our method and also excellent DTI quality for conducting robust DTI tractograph analyses.

Discussion

Quantitative measures from DWI and DTI have been successfully applied to radiation therapy of brain tumors for evaluation of tumor response [13] and for understanding radiation-induced brain injury on selected white matter structures [14, 15]. Recent developments in MRI, especially



parallel imaging [16–18] and parallel RF transmission [19] that improve imaging acquisition efficiency and reduce image artifacts due to geometric distortion, enable us to acquire high-quality DWI images with high b-value and high-quality DTI within a clinically feasible time frame to explore two new clinical applications of

- 1) improving detectability of non-enhanced hypercellular subvolumes of glioblastoma for radiation therapy and,
- 2) better understanding of radiation dose response of WM fiber pathways within the whole brain using robust and efficient DTI tractograph analyses respectively.

Our study of high b-value DWI for glioblastoma raises an exciting hypothesis that boosting the hypercellular volume delineated by high b-value DWI could delay time to progression, which is an area for future study. The new information that elongated association and projection fiber bundles respond like a serial structure, could provide a new insight into radiation treatment planning to preserve critical cognitive functions in long-term survivors. A preliminary treatment planning study also demonstrated the feasibility of dose sparing of critical WM fiber pathways without compromising the prescribed dose to the planned target volume.

While clinical applications of DWI/DTI in radiation therapy of brain tumors are promising, several limitations of DWI/DTI have impacts on their applications in radiation therapy, for example, the trade-off among overall image quality, acquisition time and geometric accuracy. Geometric distortions from susceptibility and eddy current artifacts, which are intrinsic to EPI sequences, may lead to increased uncertainty in target definition. Imaging acquisition of DWI/DTI with segmented EPI techniques like the RESOLVE-EPI DWI/DTI [4], fast spin-echo based imaging sequences such as fast spin echo PROPELLER DWI [20], and variable density spiral DTI sequence [21] could potentially improve geometric accuracy and achievable image resolution. There are still a lot of works need to be done to optimize MRI sequences, protocols and workflow for radiation oncology applications. Finally, robust QA procedure should be implemented and evaluated periodically in order to reduce variation in ADC measurement due to system performance.

References

- 1 Joiner M, van der Kogel A. Basic clinical radiobiology 4th edition. Hodder Arnold, London, 2009.
- 2 Hanahan D, Weinberg RA. Hallmarks of cancer: the next generation. *Cell* 2011; 144:646-674.
- 3 Pramanik PP, Parmar HA, Mammoser AG, Junck LR, Kim MM, Tsien CI, Lawrence TS, Cao Y. Hypercellularity Components of Glioblastoma Identified by High b-Value Diffusion-Weighted Imaging. *Int J Radiat Oncol Biol Phys* 2015; 92:811-819.
- 4 Porter DA, Heidemann RM. High Resolution Diffusion-Weighted Imaging Using Readout-Segmented Echo-Planar Imaging, Parallel Imaging and a Two-Dimensional Navigator-Based Reacquisition. *Magn Reson Med* 2009; 62:468-475.
- 5 Sheline G. Radiation therapy of brain tumors. *Cancer* 1977; 39:873-881.
- 6 Tofilon PJ, Fike JR. The radioresponse of the central nervous system: A dynamic process. *Radiat Res* 2000; 153:357-380.
- 7 Soussain C, Ricard D, Fike JR, et al. CNS complications of radiotherapy and chemotherapy. *Lancet* 2009; 374:1639-151.
- 8 Greens-Schloesser D, Robbins ME, Peiffer AM, et al. Radiation-induced brain injury: a review. *Front Oncol* 2012; 2:73. doi: 10.3389/fonc.2012.00073.
- 9 Klein M, Heimans JJ, Aaronson NK, et al. Effect of radiotherapy and other treatment-related factors in mid-term to long-term cognitive sequelae in low-grade gliomas: a comparative study. *Lancet* 2002; 360: 1361-1368.
- 10 Douw L, Klein M, Fagel SSA, et al. Cognitive and radiological effects of radiotherapy in patients with low-grade glioma: long-term follow-up. *Lancet Neurol* 2009; 8: 810-818.
- 11 Zhu T, Chapman C, Tsien C, Spratt D, Lawrence T, Cao Y. Effect of the maximum dose on white matter fiber bundles utilizing longitudinal diffusion tensor imaging. *Int J Radiat Oncol Biol Phys* 2016; 96:696-705.
- 12 Marks LB, Yorke ED, Jackson A, Ten Haken RK, Constone LS, Eisbruch A, Bentzen SM, Nam J, Deasy JO. Use of Normal Tissue Complication Probability Models in the Clinic. *Int J Radiat Oncol Biol Phys* 2010; 76:S10-S19.
- 13 Galban CJ, Hoff BA, Chenevert TL, Ross BD. Diffusion MRI in early cancer therapeutic response assessment. *NMR Biomed* 2016; doi: 10.1002/nbm.3458
- 14 Nagesh V, Tsien CI, Chenevert TL, et al. Radiation-induced changes in normal-appearing white matter in patients with cerebral tumors: A diffusion tensor imaging study. *Int J Radiat Oncol Biol Phys* 2008; 70:1002-1010.
- 15 Chapman CH, Nagesh V, Sundgren PC, et al. Diffusion tensor imaging of normal-appearing white matter as biomarker for radiation-induced late delayed cognitive decline. *Int J Radiat Oncol Biol Phys* 2012; 82:2033-2040.
- 16 Sodickson DK, Manning WJ. Simultaneous acquisition of spatial harmonics: fast imaging with radiofrequency coil arrays. *Magn Reson Med* 1997; 38:591-603
- 17 Pruessmann KP, Weiger M, Scheidegger MB, Boesiger P. SENSE: sensitivity encoding for fast MRI. *Magn Reson Med* 1999; 42:952-962.
- 18 Griswold MA, Jakob PM, Heidemann RM, et al. Generalized autocalibrating partially parallel acquisitions (GRAPPA). *Magn Reson Med* 2002; 47:1202-1210.
- 19 Katscher U, Börner P. Parallel RF transmission in MRI. *NMR Biomed*. 2006; 19:393-400.
- 20 Pipe JG, Farthing VG, Forbes KP. Multishot diffusion-weighted FSE using PROPELLER MRI. *Magn Reson Med*. 2002; 47:42-52.
- 21 Frank LR et al., High Efficiency, Low Distortion 3D Diffusion Tensor Imaging with Variable Density Spiral Fast Spin Echoes (3D DW VDS RARE). *Neuroimage* 2010; 49: 1510-1523.

Contact



Assistant Professor Tong Zhu, Ph.D.
Department of Radiation Therapy
University of North Carolina at Chapel Hill
CB# 7512, NC Cancer Hospital
101 Manning Dr
Chapel Hill, NC 27599-7512
USA
tong_zhu@med.unc.edu

Initial Clinical Experience Utilizing 4D-MRI for Radiation Treatment Planning

Eric S. Paulson^{1,3}; Nikolai J. Mickevicius^{1,3}

Departments of ¹Radiation Oncology, ²Radiology, and ³Biophysics, Medical College of Wisconsin, Milwaukee, WI, USA

Introduction

Knowledge of target and organ at risk (OAR) motion trajectories is essential in radiation therapy. Motion can result in a smearing of planned dose distributions, particularly when steep dose gradients are employed to reduce radiation doses to proximal OARs [1]. This can result in an inevitable disconnect between planned and actual doses delivered to targets and OARs over the course of treatment.

Motion management in radiation therapy involves two components: 1) generation of high-fidelity static images of targets and OARs along with models of respiratory motion for use in treatment *planning*, 2) real-time intrafraction motion monitoring for exception gating and/or tracking during treatment *delivery* [1]. Currently, the clinical standard-of-care to address the former relies on four-dimensional (4D) computed tomography (CT) images of the patient [2]. However, the poor soft tissue contrast can challenge accurate target and OAR delineation in some cancer sites with CT [3] and, thus, the accuracy of motion models obtained with this approach. Consequently, larger margins are often prescribed to prevent underdosing of tumor targets [1, 4].

Due to its non-ionizing and high soft tissue contrast properties, magnetic resonance imaging (MRI) is an ideal 4D-imaging platform. A multitude of 4D-MRI strategies have been explored in the literature, utilizing prospective and retrospective acquisitions of multi-slice 2D or 3D excitations with Cartesian and non-Cartesian readouts and a variety of motion surrogates [5–15]. Recently, self-navigated, under-sampled, retrospectively sorted 3D volumetric acquisitions have been introduced for 4D-MRI. Although long acquisition and reconstruction times (up to 8 minutes and several hours, respectively) have been reported with some of these methods, the 3D radial stack-of-stars method [12–15] offers great potential to minimize acquisition and reconstruction times while maintaining image quality. In addition, the method facilitates ease of extracting motion surrogates and is robust against motion artifacts from the inherent properties of radial k -space trajectories. We discuss here our initial clinical experience performing and utilizing 4D-MRI for radiation treatment planning.

Methods

Patients undergoing MR simulation for radiotherapy of abdominal or thoracic cancers were imaged with 4D-MRI after providing informed written consent under guidelines established by the IRB at our Institution. Following CT simulation, patients were transferred to a 3T MAGNETOM Verio scanner (Siemens Healthcare, Erlangen, Germany) and set up in treatment position on a flat table overlay. Two 6-channel flexible array coils were wrapped around the anterior of the patient and suspended on expandable RF coil bridges. Combined with the spine array, between 21 and 24 receive coils were used for imaging. Per standard MR simulation protocols at our Institution, glucagon (1 mg, Novo Nordisk, Bagsværd, Denmark) was administered intravenously in abdominal cancer patients to reduce peristalsis. Post-contrast imaging was performed following administration of Eovist (10 mL, Bayer Healthcare, Berlin, Germany) for cholangiocarcinoma patients, or Multihance (0.1 mmol/kg, Bracco Imaging, Milano, Italy).

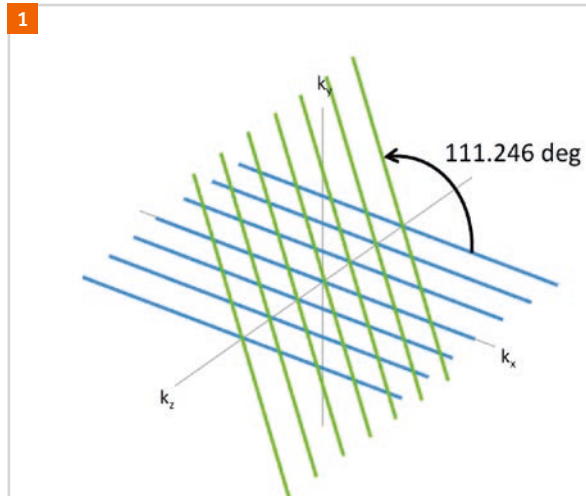


Figure 1: Hybrid 3D golden angle radial stack of stars trajectory. All partitions defining a spoke-plane are acquired before incrementing the spoke angle.

4D-MRI acquisition

A hybrid, slab-selective, 3D radial VIBE sequence of our own design was implemented for 4D-MRI. The sequence supports switchable FLASH, FISP, TrueFISP, and PSIF modes for T1 and mixed T2/T1-weighted contrasts. A 3-point Dixon readout, integrated into the sequence, is available for FLASH and FISP modes. Cartesian encoding of partitions is performed along the slab-select direction (k_z) for a given spoke angle, forming a spoke-plane. After acquisition of the prescribed partitions within the spoke-plane, the spoke angle is incremented by the golden angle ($\pi \times \text{golden ratio} = 111.246^\circ$) and another spoke-plane is acquired (Fig. 1). This process is repeated for the entire scan duration. In this manner, a unique spoke is sampled throughout the entire duration of the acquisition, eliminating the need to complex average overlapping spokes after the k -space data are retrospectively sorted into respiratory phases. Typical 4D-MRI scan parameters included: axial prescription, field-of-view: 330 mm, base resolution: 192, readout bandwidth: 200 kHz, TE/TR: 1.3/3.5 msec, flip angle: 10° , slab thickness: 240 mm, total acquisition time: 2 minutes.

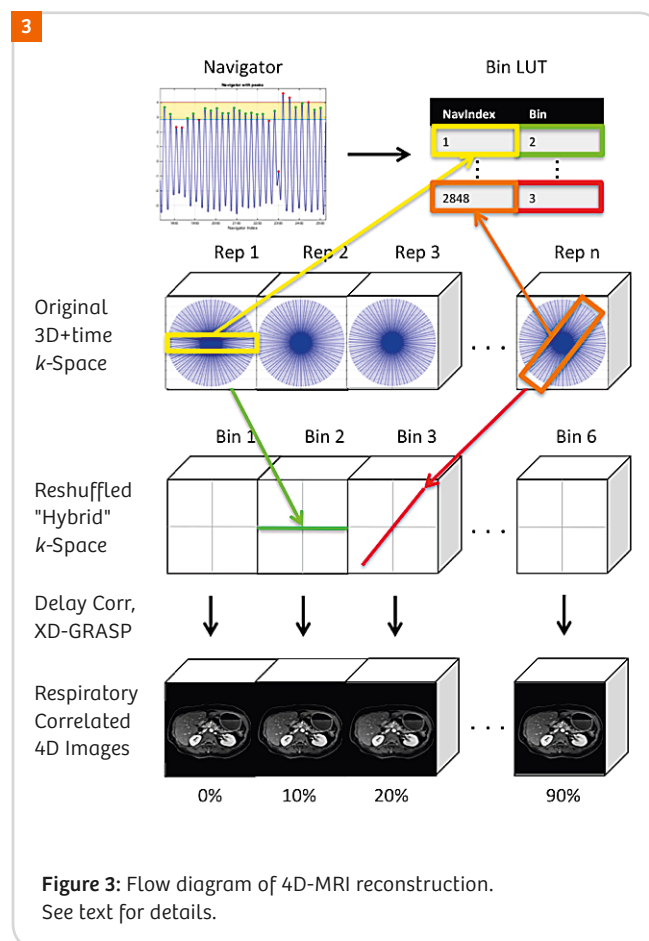
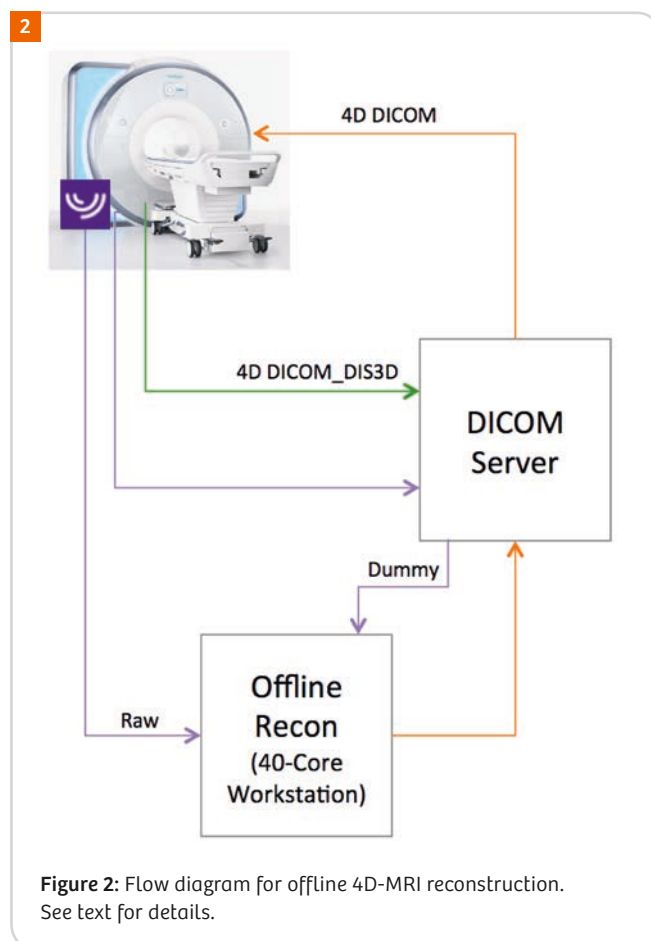
4D-MRI reconstruction pipeline

Figure 2 displays a flow diagram of the 4D-MRI reconstruction pipeline. The raw k -space data were transferred offline

to a 40-core, 2.3 GHz Linux workstation using the Yarra RDS client (<https://yarra.rocks/doc/client/RDS>). In addition, DICOM images from a quick dummy scan, acquired over the same geometrical prescription, were exported to the workstation to facilitate gradient nonlinearity correction. The reconstructed 4D-MR images were converted to DICOM with header information transferred from the dummy scan headers. The 4D-MRI DICOM images were then piped back to the scanner where 3D gradient nonlinearity distortion correction was performed online (orange arrows in Fig. 2). Finally, the distortion corrected 4D-MR images were sent to a clinical delineation software package for use during radiation treatment planning (green arrows in Fig. 2).

4D-MRI reconstruction

4D-MR images were reconstructed in Matlab (The Mathworks, Natick, MA, USA) using the non-uniform fast Fourier transform (NUFFT) toolbox [16]. Projections along the slab-select direction were generated by taking the 1D Fourier transform of the acquired k -space signal passing through the axis of rotation ($k_x = k_y = 0$). One-dimensional motion surrogate signals from all receive coils were generated by plotting the center of mass of each projection, or the cross-correlation coefficient of a given projection against a reference projection as a function of time. These signals were then bandpass filtered between 0.1 and 0.5 Hz



to remove DC offset and high frequency fluctuations (e.g., cardiac motion). Principal component analysis was performed to obtain a single motion surrogate signal using information from all receive coils. This derived navigator signal, analogous to external motion surrogate signals acquired using reflector-camera or respiratory bellows during 4D-CT acquisitions, arises from changes in total signal power during respiration. Constrained amplitude-based sorting was then applied to retrospectively reshuffle each acquired spoke-plane into a hybrid k -space of six-to-eight respiratory phase bins. Correction for gradient and receive chain group delays was performed using an iterative approach [17]. The XD-GRASP algorithm [14, 18], a compressed sensing method exploiting temporal sparsity, was then applied to improve image quality. This process is shown graphically in Figure 3. The Cartesian sampling of the radial stack of stars trajectory was exploited to reduce image reconstruction time by parallelizing over partitions once an initial 1D Fourier transform along the slab-select direction was performed [15].

4D-MRI radiation treatment planning

4D-MR images were loaded into clinical delineation software side-by-side with conventional 4D-CT images sorted based on reflector-camera surrogate. Maximum target motion extents and trajectories were compared between 4D-MRI and 4D-CT. Internal target volumes were constructed on the 4D-CT images and reviewed for agreement on the 4D-MR images.

Results

All patients successfully completed the 2-minute 4D-MRI acquisition. Total reconstruction time was approximately 8 minutes, demonstrating the advantage of the 4D radial

stack-of-stars approach in permitting the reconstruction to be parallelized over partitions. Unlike conventional 4D-CT or other 4D-MRI methods relying on peripheral motion surrogates, no gain resetting or signal saturation was observed in the self-navigated radial stack of stars 4D-MRI motion waveforms used to guide the k -space data reshuffling.

Figure 4 displays one respiratory frame of 4D-CT, and T1-weighted 4D-MR images of a cholangiocarcinoma patient obtained prior to and 20 minutes post-Eovist administration. Consistent with prior studies [14, 15], the XD-GRASP algorithm was effective at reducing undersampling artifacts in the reshuffled pre- and post-contrast 4D-MRI data. The tumor region is more readily discernable on pre and post-Eovist 4D-MR images compared to 4D-CT images. The post-Eovist 4D-MR images also demonstrate a clear demarcation between functioning and dysfunctional hepatocytes.

Figure 5 displays one respiratory frame of 4D-CT and post-Multihance T1-weighted 4D-MR images in a patient with liver metastasis. The liver met is more easily visualized on the 4D-MR images compared to 4D-CT (yellow arrow). In addition, the 4D-MR images do not demonstrate stitching artifacts present on the 4D-CT (evident at the lung-liver interface in the sagittal plane).

Figure 6 displays axial, water-only and fat-only T1-weighted 4D-MR images at inspiratory and expiratory phases for a pancreas cancer patient, obtained using a 4D-MRI Dixon FLASH acquisition. The reconstruction algorithm was effective at separating fat, water, and motion phases.

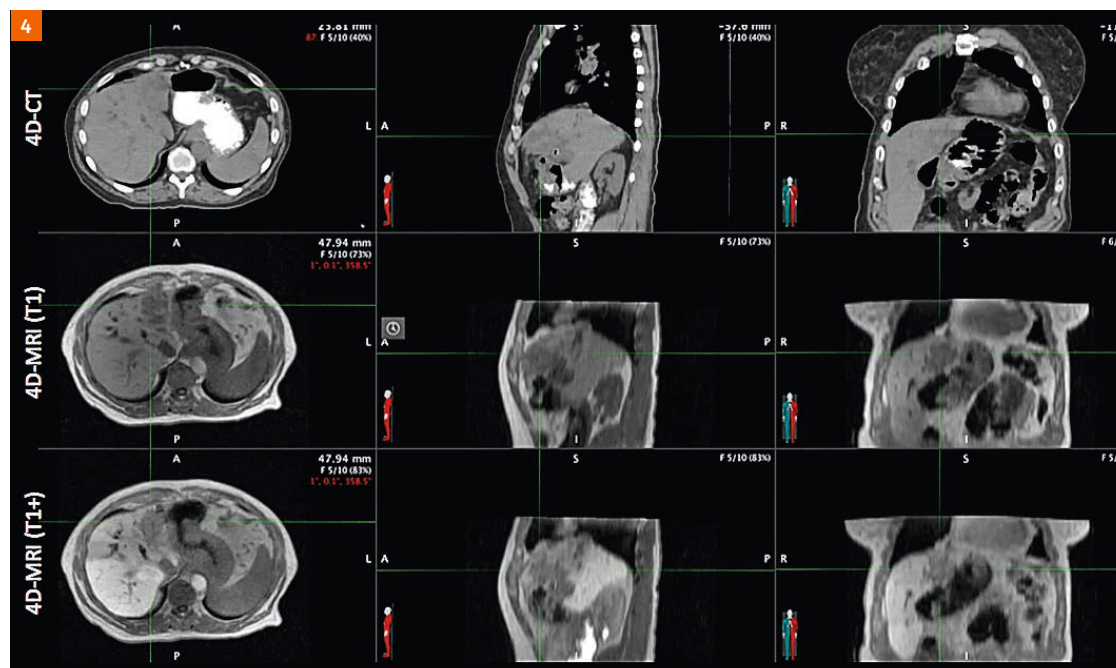


Figure 4: Comparison of 4D-CT (top row) and T1-weighted pre- (middle row) and 20 minute post-Eovist (bottom row) 4D-MR images in a cholangiocarcinoma patient.

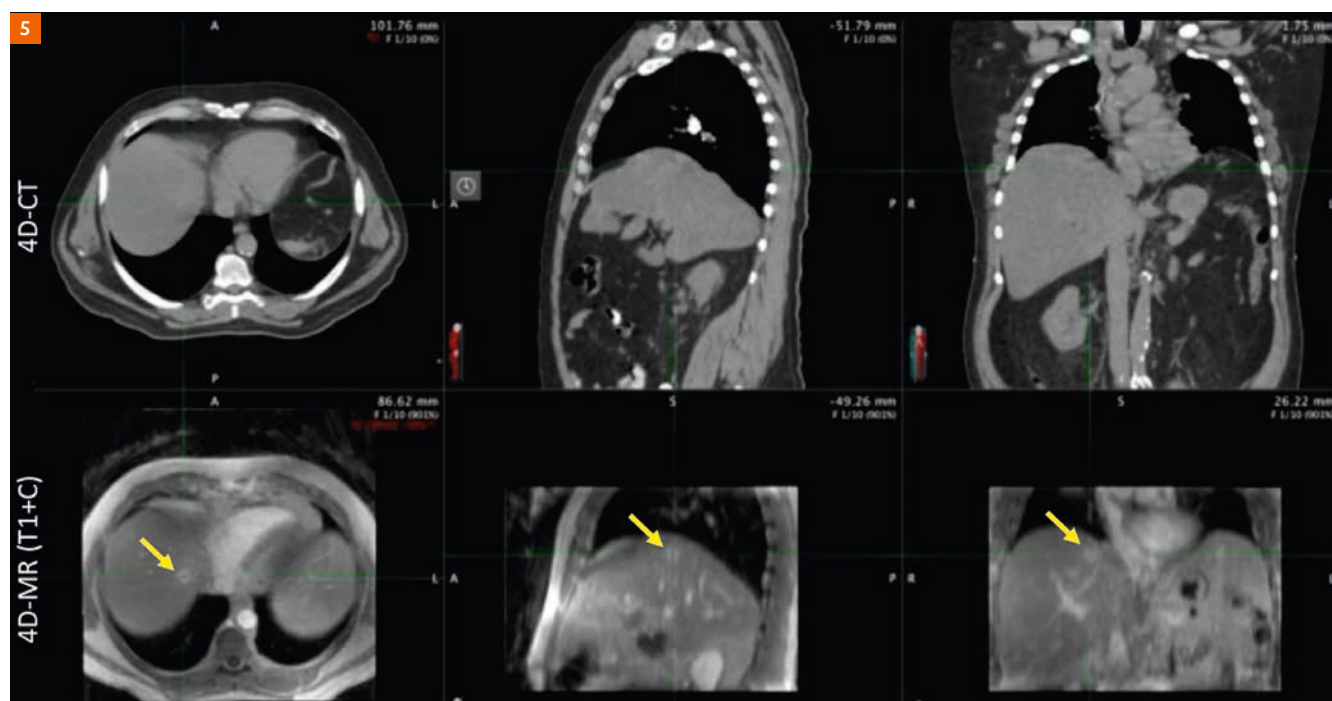


Figure 5: End expiratory 4D-CT (top) and post-Multihance T1-weighted 4D-MR (bottom) images of a liver metastasis patient. The enhancing liver met is more readily visible on the 4D-MR images (yellow arrow).

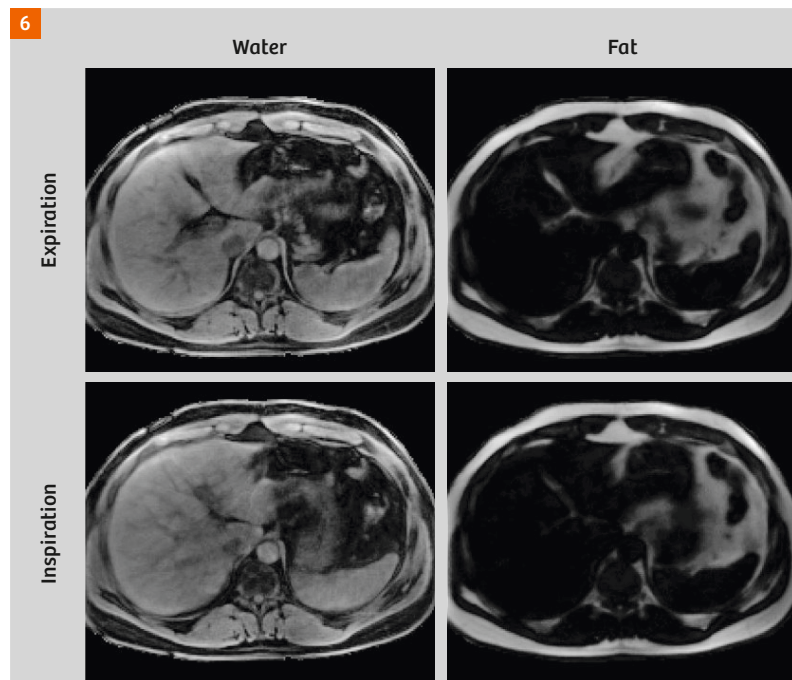


Figure 6: Water-only and fat-only inspiratory and expiratory 4D-MR images of a pancreas cancer patient obtained using a 4D Dixon FLASH acquisition.

Figure 7 displays one respiratory frame of a mixed T2/T1-weighted 4D-MR image obtained in a healthy volunteer using a 4D-MRI PSIF acquisition. Compared to TrueFISP, the PSIF image does not demonstrate banding artifacts but does display increased T2 contrast (evident from the bright cerebrospinal fluid signal).

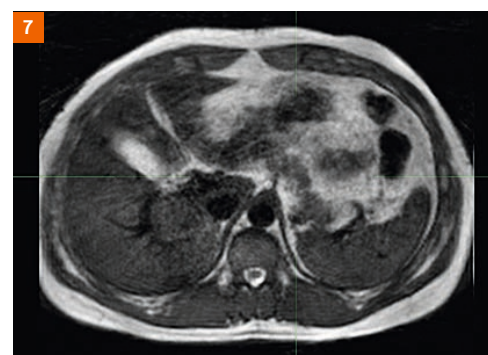


Figure 7: Mixed T2/T1-weighted 4D-MR image of a healthy volunteer acquired using a 4D-MR PSIF acquisition. The increased T2 weighting is evident by the bright CSF signal.

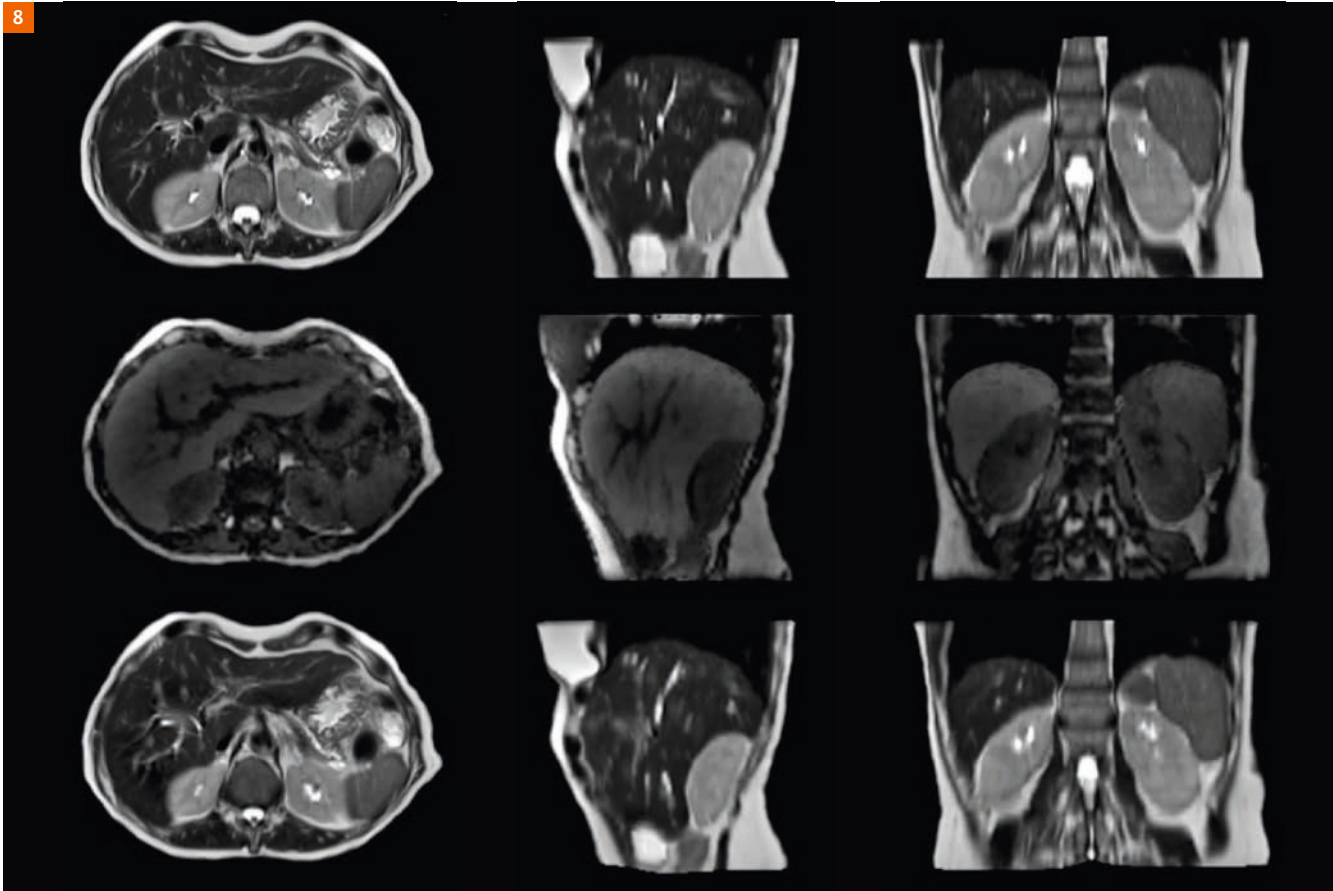


Figure 8: Demonstration of using 4D-MRI as a vehicle. Respiratory-triggered T2 TSE images acquired at end expiration (top row) are transformed to a mid-position anatomical state (middle row) using 4D-MRI and deformable image registration. This process permits image contrasts to be obtained at one respiratory phase more favorable for acquisition, and then transformed to another phase more favorable for treatment delivery (bottom row).

Figure 8 demonstrates the feasibility of using 4D-MRI as a vehicle. In this case, respiratory-triggered T2 images are transformed to a time-averaged, mid-position 4D-MR image [19]. This process permits image contrasts to be acquired at a phase of the respiratory cycle more favorable for acquisition and then be transformed to a potentially different respiratory phase more favorable for treatment delivery.

Discussion

The 4D-MRI method discussed here utilizes the self-navigating properties of radial k -space trajectories to generate respiratory-correlated 4D-MR images. The change in intensity producing the self-navigating signal arises from a change in total signal power in the excited volume during respiration. The method eliminates the need for external respiratory surrogates (bellows, reflector camera, body surface area, etc), and improves image contrast and reduces sorting errors compared to 4D-CT. The spin system steady state is maintained by consecutively exciting the same slab with each shot, and increased efficiency is obtained by

eliminating the need to interlace 1D pencil beam or 2D image navigators. In a prior motion phantom study, the displacement estimates obtained with the 4D-MRI method used here were within 1 mm [15].

We have made several observations during our initial clinical experience of performing and utilizing 4D-MRI for treatment planning:

- 4D-MRI may increase clinical efficiency compared to 4D-CT, depending on the technology available in a particular clinic. The increased efficiencies arise from reduction in setup time for ancillary 4D equipment (respiratory bellows/reflector-camera), (re-)positioning of the equipment, faster acquisition times, and elimination of manual sorting.
- Stitching artifacts that may be present on 4D-CT images are greatly reduced on 4D-MR images. However, in extreme cases of inconsistent breathing patients, respiratory motion inconsistencies can result in a slight blur on 4D-MR images.

- Similar to 4D-CT, the motion waveform derived from the 4D-MR acquisition, and its Fourier transform, can be used to judge whether a given patient may be a candidate for respiratory-gated treatment delivery.
- VIBE interpolation can contribute to blurring along the slab-select direction, which can be reduced by increasing the number of partitions acquired within the slab. Slice partial Fourier can be employed to maintain a high navigator sampling rate in these cases.
- Metal¹ and plastic stents do not appear to significantly obscure 4D-MR image quality.
- Administration of exogenous contrast agents can obscure some structures on non-fat-suppressed T1-weighted 4D-MRI. However, this can be rectified by switching to a 4D-MRI Dixon FLASH acquisition.

The optimal image contrast and timing of the 4D-MRI acquisition within the MR simulation exam may be disease specific. The present 4D-MRI method permits switchable FLASH, FISP, TrueFISP, and PSIF modes, permitting tailoring of 4D image contrast on a tumor-specific basis. Additional studies are planned to determine the optimal 4D-MRI contrast and timing for each cancer site.

References

- 1 Keall PJ, Mageras GS, Balter JM, Emery RS, Forster KM, Jiang SB, Kapatoes JM, Low DA, Murphy MJ, Murray BR, Ramsey CR, Van Herk MB, Vedam SS, Wong JW, Yorke E. The management of respiratory motion in radiation oncology report of AAPM task group 76. *Med Phys* 2006; 33:3874-3900.
- 2 Goldstein SD, Ford EC, Duhon M, McNutt T, Wong J, Herman JM. Use of respiratory-correlated four-dimensional computed tomography to determine acceptable treatment margins for locally advanced pancreatic adenocarcinoma. *Int J Radiat Oncol Biol Phys* 2010; 597-602.
- 3 Njeh CF. Tumor delineation: The weakest link in the search for accuracy in radiotherapy. *J Med Phys* 2008; 33:136-140.
- 4 Blackall JM, Ahmad S, Miquel ME, McClelland JR, Landau DB, Hawkes DJ. MRI-based measurements of respiratory motion variability and assessment of imaging strategies for radiotherapy planning. *Phys Med Biol* 2006; 51:4147-4169.
- 5 Von Siebenthal M, Szekely G, Gamper U, Boesiger P, Lomax A, Cattin Ph. 4D MR imaging of respiratory organ motion and its variability. *Phys Med Biol* 2007; 52:1547-1564.
- 6 Tokuda J, Morikawa S, Haque HA, Tsukamoto T, Matsumiya K, Liao H, Masamune K, Dohi T. Adaptive 4D MR Imaging using Navigator-Based Respiratory Signal for MRI-Guided Therapy. *Mag Reson Med* 2008; 59:1051-1061.
- 7 Cai J, Chang Z, Wang Z, Segars WP, Yin FF. Four-dimensional magnetic resonance imaging (4D-MRI) using image-based respiratory surrogate: A feasibility study. *Med Phys* 2011; 38:6384-6394.
- 8 Hu Y, Caruthers SD, Low DA, Parikh PJ, Mutic S. Respiratory amplitude guided 4-dimensional magnetic resonance imaging. *Int J Radiat Oncol Biol Phys* 2013; 86:198-204.
- 9 Tryggestad E, Flammang A, Han-Oh S, Hales R, Herman J, McNutt T, Roland T, Shea SM, Wong J. Respiration-based sorting of dynamic MRI to derive representative 4D-MRI for radiotherapy planning. *Med Phys* 2013; 40:051909-1 – 051909-12.
- 10 Celicanin Z, Bieri O, Preiswerk F, Cattin P, Scheffler K, Santini F. Simultaneous Acquisition of Image and Navigator Slices using CAIPIRINHA for 4D MRI. *Mag Res Med* 2015; 73:669-676.
- 11 Du D, Caruthers SD, Glide-Hurst C, Low DA, Li HH, Mutic S, and Hu Y. High-Quality T2- Weighted 4-Dimensional Magnetic Resonance Imaging for Radiation Therapy Applications. *Int J Radiat Oncol* 2015; 92:430-437.
- 12 Stemkens B, Tijssen RHN, de Senneville BD, Heerkens HD, van Vulpen M, Lagendijk JJW, and van den Berg CAT. Optimizing 4-dimensional magnetic resonance imaging data sampling for respiratory motion analysis of pancreatic tumors. *Int J Radiat Oncol Biol Phys* 2015; 91:571-8.
- 13 Deng Z, Pang J, Yang W, Yue Y, Sharif B, Tuli R, Li D, Fraass B, and Fan Z. Four- dimensional MRI using three-dimensional radial sampling with respiratory self-gating to characterize temporal phase-resolved respiratory motion in the abdomen. *Magn Reson Med* 2015;
- 14 Feng L, Axel L, Chandarana H, Block KT, Sodickson DK, Otazo R. XD-GRASP: Golden-angle radial MRI with reconstruction of extra motion-state dimensions using compressed sensing. *Magn Reson Med* 2016; 75:775-88.
- 15 Mickevicius NJ, Paulson ES. Investigation of undersampling and reconstruction algorithm dependence on respiratory correlated 4D-MRI for online MR-guided radiation therapy. *Phys Med Biol* 2016; (in press)
- 16 Fessler JA, Sutton BP. Nonuniform fast Fourier transforms using min-max interpolation. *IEEE Trans Sig Proc* 2013; 51:560-574.
- 17 Krämer M, Biermann J, Reichenbach JR. Intrinsic correction of system delays for radial magnetic resonance imaging. *Magn Reson Imag* 2015; 33:491-6
- 18 Benkert T, Feng L, Sodickson DK, Chandarana H, Block KT. Free-breathing volumetric fat/water separation by combining radial sampling, compressed sensing, and parallel imaging. *Magn Reson Med* 2016; (in press)
- 19 Wolthaus JW, Sonke JJ, van Herk M, Belderbos JS, Rossi MM, Lebesque JV, Damen EM. Comparison of different strategies to use four-dimensional computed tomography in treatment planning for lung cancer patients. *Int J Radiat Oncol Biol Phys* 2008; 70:1229-38.

¹ The MRI restrictions (if any) of the metal implant must be considered prior to patient undergoing MRI exam. MR imaging of patients with metallic implants brings specific risks. However, certain implants are approved by the governing regulatory bodies to be MR conditionally safe. For such implants, the previously mentioned warning may not be applicable. Please contact the implant manufacturer for the specific conditional information. The conditions for MR safety are the responsibility of the implant manufacturer, not of Siemens.

Contact



Eric Paulson, Ph.D., DABR
Assistant Professor and Senior
Medical Physicist
Radiation Oncology, Radiology,
and Biophysics

Medical College of Wisconsin
Radiation Oncology
8701 Watertown Plank Road
Milwaukee, WI 53223
USA
epaulson@mcw.edu

Metastatic Prostate Cancer in Practice – the MET-RADS-P Imaging Response System Using Whole-body MRI

Anwar R. Padhani¹; Nina Tunariu²

¹ Paul Strickland Scanner Centre, Mount Vernon Hospital, Northwood, Middlesex, UK

² Royal Marsden NHS Foundation Trust & Institute of Cancer Research and Cancer Research UK Cancer Imaging Centre, Sutton, Surrey, UK

Introduction

Whole-body MRI (WB-MRI) is an increasingly used, radiation-free imaging method for assessing bone and soft tissue pathology, and for evaluating response to therapy [1]. WB-MRI has been developed to overcome the limitations of Bone Scintigraphy (BS) and Computed Tomography (CT) for detection and therapeutic response assessments in bone metastases [2]. Although increasingly used and recommended by international guidelines for multiple myeloma [3], WB-MRI usage has been confined mainly to expert centers, causing some concerns about its broader applicability. While WB-MRI can be performed on almost all modern MRI scanners, inconsistencies in WB-MRI acquisition protocols and reporting standards have prevented its widespread testing and implementation, beyond the indication for multiple myeloma.

Recently, a group of oncologic imaging specialists teamed with a leading urologist and oncologist, to develop recommendations on the minimum requirements for WB-MRI acquisition protocol as well as standardized reporting guidelines. They recognized that for this promising method to become mainstream it is vital to enforce some uniformity in acquisition, interpretation, and reporting. The authors have named their formulation for metastatic disease response and diagnostic system for prostate cancer as MET-RADS-P (METastasis Reporting And Data System for Prostate cancer) [4].

Why MET-RADS is needed

BS/CT scans are widely used and endorsed by international guidelines as the standard imaging investigations in the staging and follow-up of metastatic prostate cancer, thereby affecting patient management [5, 6]. However, it is increasingly clear that currently used imaging methods are limited in their effectiveness in directing therapy and may no longer be relevant in the era of high-precision medicine, where an increasing number of cytostatic and novel therapies are becoming available [2]. For example, the accepted minimum lymph node diameter (10 mm – short axis) on CT scan as measure of involvement is only modestly correlated with the presence of malignant disease, and CT cannot accurately evaluate the presence or the therapeutic response in bone

metastases, the commonest metastatic site in prostate cancer. Conversely, increased BS uptake in number and extent of lesions can equally occur with the osteoblastic healing (FLARE reaction) associated with tumor response and with the osteoblastic progression associated with tumor burden increase, thus creating confusion between response and progression, when response to therapy is being assessed. Next generation whole-body imaging tools such as PET with targeted tracers and WB-MRI with diffusion-weighted sequences are emerging as powerful alternatives; however, the challenge remains in validating these newer imaging approaches, so that their use can be justified in the clinical routine.

An important step in this process is to ensure uniformity in the acquisition, interpretation, and reporting of next generation whole-body imaging methods, so that multicenter trials leading to validation of these methods can be more easily performed and evaluated. An important step for WB-MRI is the new MET-RADS-P standard for use in patients with advanced prostate cancer [4]. The standard establishes minimum acceptable technical parameters for imaging acquisitions built with sequences already available on most modern scanners. Of the sequences recommended, it is acknowledged that whole-body diffusion-weighted sequences are the most challenging to implement across imaging platforms. These sequences have been grouped to enable fast, high-quality examinations for tumor detection and response assessments (core and comprehensive protocols respectively). Image quality control and quality assurance procedures are also detailed by the standard. The MET-RADS-P standard is designed to offer day-to-day reporting guidance, paired with a detailed reporting tool that describes the disease phenotype based on anatomic patterns of metastatic spread thus, enabling systematic collection of analyzable data for research purposes.

Comprehensive response criteria for bone and soft tissue metastases and local disease have been proposed, with the ability to summarize the likelihood of a response to treatment, using a Likert-like 1–5 scale. It is important to note that the summarized likelihood of response in bone, uses newly developed MET-RADS criteria, but the response in soft-tissues continues to be based on long established

Figure 1: Updated MET-RADS-P template form and response criteria for bone and soft tissue disease.

1A Physician Exam date current Exam date comparator

Soft tissues RECIST		MET-RADS Prostate Report		Bones MET-RADS	
Primary Involved	Y N		Skull Involved	Y N	
RAC	1- 2+		RAC	1- 2+	
Comment			Comment		
Pelvic nodes Involved	Y N		Cervical spine Involved	Y N	
RAC	1- 2+		RAC	1- 2+	
Comment					
Retroperitoneal Involved	Y N		Dorsal spine Involved	Y N	
RAC	1- 2+		RAC	1- 2+	
Comment			Comment		
Other nodes Involved	Y N		Lumbosacral spine Involved	Y N	
RAC	1- 2+		RAC	1- 2+	
Comment			Comment		
Liver Involved	Y N		Pelvis Involved	Y N	
RAC	1- 2+		RAC	1- 2+	
Comment			Comment		
Lungs Involved	Y N		Thorax Involved	Y N	
RAC	1- 2+		RAC	1- 2+	
Comment			Comment		
Other sites Involved	Y N		Limbs Involved	Y N	
RAC	1- 2+		RAC	1- 2+	
Comment			Comment		

Response assessment categories (RAC): 1 Highly likely to be responding; 2 Likely to be responding; 3 No change; 4 Likely to be progressing; 5 Highly likely to be progressing. Single lesion 1* RAC only; ≥2 lesions/diffuse disease use both RACs

Metastasis Reporting and Data System for Prostate Cancer: Practical Guidelines for Acquisition, Interpretation, and Reporting (MET-RADS-P) of Whole-body MRI Evaluations of Metastatic Involvement in Advanced Prostate Cancer. Eur Urol. 2017 Jan;71(1):81-93.

Radiologist Date

1B RAC Region Local, nodal and visceral MET-RADS-P Description

1	Bone	Consistent with RECIST v1.1/PCWG criteria for unequivocal response (partial/complete).
		Return of normal marrow in areas previously infiltrated by focal/diffuse metastatic infiltration Decrease in number/size of focal lesions Evolution diffuse neoplastic pattern to focal lesions Decreasing soft tissue associated with bone disease Dense lesion sclerosis (edge to edge), sharply defined, very thin/disappearance of hyperintense rim on T2W-FS images The emergence of intra-peri-tumoural fat within/around lesions (fat dot/halo signs) Previously evident lesion shows increase in ADC from $\leq 1400 \mu m^2/s$ to $>1400 \mu m^2/s$ ≥40% increase in ADC from baseline with corresponding decrease in high b-value SI; and morphological findings consistent with stable or responding disease
2	Bone	Changes depicting tumour response that do not meet RECIST v1.1/PCWG criteria for partial or complete response (see below)
		Evidence of improvement, but not enough to fulfil criteria for RAC 1. For example: Previously evident lesions showing increases in ADC from $\leq 1000 \mu m^2/s$ to $<1400 \mu m^2/s$ >25% but <40% increase in ADC from baseline with corresponding decrease in high b-value SI; and morphological findings consistent with stable or responding disease
3	All	No observable change
4	Bone	Changes depicting tumour progression that do not meet RECIST v1.1/PCWG criteria for progression
		Evidence of worsening disease, but not enough to fulfil criteria for RAC 5. Equivocal appearance of new lesion(s)
5	Bone	No change in size but increasing SI on high b-value images (with ADC values $<1400 \mu m^2/s$) consistent with possible disease progression
		Relapse disease: re-emergence of lesion(s) that previously disappeared or enlargement of lesion(s) lesions that had partially regressed/stabilized with prior treatments Imaging depicted bone lesions that might be clinically significant (therefore excludes asymptomatic fractures in non-critical bones) Soft tissue in spinal canal causing narrowing not associated with neurological findings and not requiring radiotherapy
5	Bone	Tumour progression that meet RECIST v1.1/PCWG criteria for unequivocal progression
		New critical fracture(s)/cord compression requiring radiotherapy/surgical intervention → only if confirmed as malignant by MRI signal characteristics Unequivocal new focal/diffuse area(s) of metastatic infiltration in regions of prior normal marrow Unequivocal increase in number/size of focal lesions Evolution of focal lesions to diffuse neoplastic pattern Appearance/increasing soft tissue associated with bone disease New lesions/regions of high signal intensity on high b-value images with ADC value between 600-1000 $\mu m^2/s$

Response Assessment Category (RAC) allocation rules – compare to relevant baseline scan

The primary RAC value is based on the dominant response of more than half of the disease within the region; The secondary RAC value is for the second most frequent pattern of response.

For a single lesion in a region only the primary number category is assessed. Regions with multiple lesions/diffuse disease, all with the same RAC, both the primary and secondary have the same values

When equal numbers of lesions are of higher and lower RACs then the primary pattern allocation is reserved for the higher RAC

RECIST v1.1 categories

- Complete Response (CR): Disappearance of all target lesions
- Partial Response (PR): At least a 30% decrease in the sum of the longest diameter (LD) of target lesions, taking as reference the baseline sum LD
- Stable Disease (SD): Neither sufficient shrinkage to qualify for PR nor sufficient increase to qualify for PD, taking as reference the smallest sum LD since the treatment started
- Progressive Disease (PD): At least a 20% increase in the sum of the LD of target lesions, taking as reference the smallest sum LD recorded since the treatment started or the appearance of one or more new lesions

Progression of local prostate disease: Use RECIST v1.1 for progression criteria above applied to local disease

Progression of nodes (short axis)

- <1.0 cm nodes have to have grown by at least 5 mm in from baseline or treatment nadir and be ≥1 cm to be considered to have progressed
- For nodes that are 1.0-1.5 cm that have grown by at least 5 mm from baseline or treatment nadir and are ≥1.5 cm in short axis can be considered to have progressed
- For nodes ≥1.5 cm short axis use RECIST v1.1 progression criteria

Progression of visceral disease: Use RECIST v1.1 progression criteria above applied to visceral disease

Figure 1A: Updated MET-RADS-P template form allocates the presence of unequivocal identified disease to 14 predefined regions of the body (primary disease, seven skeletal and three nodal regions, lung, liver and other soft tissue sites) at baseline and on follow-up assessments. At each anatomical location, the presence of disease is indicated (yes/no) together with the response assessment categories (primary/secondary). The overall response of the primary tumor, nodal and visceral disease are categorical (no disease (ND), complete response (CR), partial response (PR), stable disease (SD) and progressive disease (PD)). However, the overall response of bone disease is on a scale of 1–5 indicating the likely overall response category: (1) highly likely to be responding, (2) likely to be responding, (3) stable, (4) likely to be progressing and (5) highly likely to be progressing.

Figure 1B: Criteria for regional response assessment categories (RACs) that summarize likelihood of response in bone disease employ the newly developed MET-RADS criteria, but RACs for response in soft-tissues uses established standards already prescribed by RECIST v1.1 and PCWG guidance [7, 8]. Response assessment is indicated on a 1–5 scale indicating the likely RAC for each location, comparing to the baseline study (RAC-1, indicates highly likely to be responding, up to RAC-5, indicating highly likely to be progressing).

Figure 2: Primary resistance to hormonal therapy
67-year-old male with metastatic castrate resistant prostate cancer (mCRPC).
WB-MRI examinations before and on androgen deprivation therapy (Abiraterone and Goserelin).

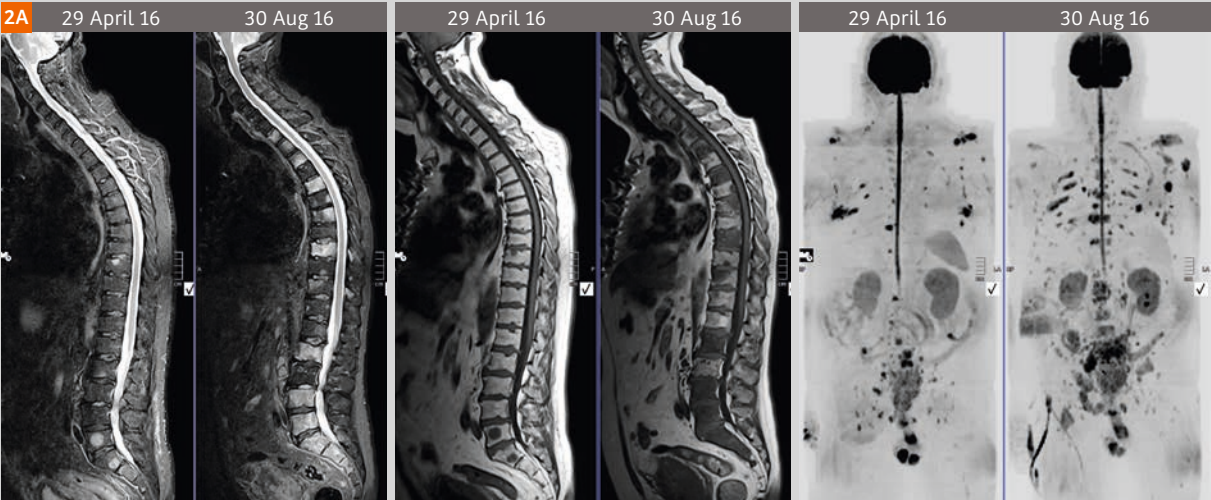


Figure 2A: Marked disease progression can be seen on morphology T1-weighted and STIR sequences and on WB b900 MIP images and confirmed by ADC measurements (see Fig. 2D also). Disease progression is seen in the prostate gland with extensive bladder invasion together with rectal invasion. There is disease progression in pelvic and retroperitoneal lymph nodes with nodal enlargement in the left axilla also. There is bone disease progression throughout the spine with extra-osseous soft tissue disease with new and enlarging deposits. No liver or lung disease is seen. The spinal stenosis at L3/L4 is degenerative in nature.

2B

30/08/2016 MRI Whole body

Clinical details: mCRPC. Restaging post urinary diversion. On Abiraterone and zoledex.

Technique: A whole-body MRI scan with whole body diffusion sequences. Comparison is made to the previous whole-body MRI scan dated 29/04/2016.

Findings:

Cervical and dorsal spine:

The intervertebral bony alignment is normal. Regrettably, there is marked disease progression. New metastases are seen throughout the cervical and dorsal spine with multifocal lesions. No interval loss of vertebral height. The cervicodorsal junction is normal. The cervical and dorsal cord outline normally.

Lumbosacral spine:

The intervertebral bony alignment remains normal with no interval loss of vertebral height. Degenerative spinal stenosis at L3/L4 as noted on the previous occasion. Regrettably, there is marked disease progression in the lumbosacral spine since the previous study.

Body scan:

No skull vault deposits have emerged. Normal sinonasal airways.

No supraclavicular fossa lymphadenopathy. Progressive left axillary lymphadenopathy also.

There is marked disease progression left scapula bone with extra osseous soft tissue disease now visible. Marked disease progression the ribs bilaterally also. There are artefacts sternotomy wires.

The central mediastinal and hilar regions are normal. No lung abnormalities are detected.

The liver and spleen are homogeneous. Normal pancreas and adrenal glands. Both kidneys are unobstructed with bilateral renal stents in situ. Small retroperitoneal lymph nodes are also detected.

Extensive metastatic bone disease is present in the sacrum predominantly on the left side, right and left hemipelvis bone disease also.

Nodal disease in the common iliac regions bilaterally. Right obturator region with extra nodal tumour spread.

There is large locally advanced prostate carcinoma with bladder and ureteric involvement. No tumour involvement of the rectum or rectosigmoid junction.

Metastatic disease in the right proximal femur also.

Impression:

There is marked disease progression since 29/04/2016. Disease progression is seen locally the prostate gland with extensive bladder invasion. There is disease progression within pelvic and retroperitoneal lymph nodes with extra nodal tumour spread. There is disease progression in the left axilla also. Bone disease progression additionally throughout the spine with extra-osseous soft tissue disease also visible. No new visceral relapse of disease.

Please see graphical MET-RADS-P report also.

2C

Physician PO

Exam 30/8/16

Exam 29/4/16

Soft tissues	MET-RADS Prostate Report						Bones
RECIST							MET-RADS
Primary Involved Y							Skull Involved N
RAC 3/5							RAC
Rectal and bladder involvement							Comment
Pelvic nodes Involved Y							Cervical spine Involved N
RAC 3/5	5/5	5/5	5/5	5/5	5/5	5/5	
Other nodes	OVERALL ASSESSMENT						Dorsal spine Involved Y
Involved Y	No dis	CR	PR	SD	PD	DISCORD	RAC 5/5
RAC 3/5	Primary				✓		5/5
Left axilla	Nodes	✓				No/minor/major only for PR/SD categories	
Liver	Viscera				✓		Pelvis Involved Y
Involved N	Bones	✓				5	RAC 5/5
RAC 3/5	Comments						Comment
Comment	Bladder and rectal involvement by primary tumor.						
Lungs							Thorax Involved Y
Involved N							RAC 5/5
RAC 3/5							Comment
Other sites							Limbs Involved Y
Involved N							RAC 5/5
RAC 3/5							Comment

Response assessment categories (RAC): 1 Highly likely to be responding; 2 Likely to be responding; 3 No change; 4 Likely to be progressing; 5 Highly likely to be progressing. Single lesion 1* RAC only; a2 lesions/diffuse disease use both RACs

MET-RADS Reporting and Data System for Prostate Cancer: Protocol Guidelines for Acquisition, Interpretation, and Reporting (MET-RADS-P) of Whole-body MRI Evaluations of Multisite Involvement in Advanced Prostate Cancer, Eur Urol. 2017 Jan;71(1):85-92.

Figure 2B: Original text report for the follow-up examination that accompanies the MET-RADS-P template report.

Figure 2C: Completed MET-RADS-P template report indicating sites of disease and RACs at each anatomical location compared to the baseline study. The presence of unequivocal identified disease is indicated together with primary and secondary RACs at each site using the criteria set out in Figure 1B. Short relevant comments are included for clarification purposes where needed.

Figure 2D: WB-tumor load segmentation undertaken on syngo.via Frontier MR Total Tumor Load software (Siemens Healthcare; released research prototype – not part of the MET-RADS-P standard) for illustrative purposes only.

The whole-body b900 images are segmented using computed high b-value images of 1200 s/mm² and signal intensity threshold of approximately 100 AU. Extraneous signals (such as the brain, kidneys, bowel, gonads) are removed to leave only recognizable disease sites. The color the b900 MIP images are overlaid with ADC value classes using the thresholds indicated. The green voxels are values $\geq 1500 \mu\text{m}^2/\text{s}$ (representing voxels that are 'highly likely' to be responding). The yellow voxels are set to lie between the 95th centile ADC value of the pre-treatment histogram (1295 $\mu\text{m}^2/\text{s}$) and 1500 $\mu\text{m}^2/\text{s}$ thus representing voxels 'likely' to be responding. Red-voxels represent mostly untreated disease.

43 mL of tumor are segmented before therapy and 472 mL on therapy. Note that there is no significant global increase in ADC values (859 $\mu\text{m}^2/\text{s}$ and 885 $\mu\text{m}^2/\text{s}$) on the corresponding absolute frequency histograms. There is also no increase in the standard deviation of the histogram (247 and 249 $\mu\text{m}^2/\text{s}$). Note increased extent and volume of red-voxels consistent with disease progression (95% before therapy and 94% after therapy).



standards, prescribed by RECIST v1.1 and PCWG, the Prostate Cancer Working Group [7, 8] for clinical research. Discordant responses in which progressing and responding lesions are seen at same time point, are increasing seen with the use of targeted therapies and are a recognized manifestation of tumor heterogeneity. MET-RADS-P proposes methods to record the presence, location and extent of discordant responses between and within body parts. The use of MET-RADS-P enables for the first time to categorize bone disease response into 3 categories (progressive disease, stable disease and response), rather than the clinically recommended categories (progression/no progression) when using BS/CT scans [8], thus mirroring response assessments in soft tissues disease.

The benefits of using a standardized approach include enhanced data collection for outcomes monitoring in clinical trials and from patient registries, enhancing the education of radiologists to reduce variability in imaging interpretations, and for improving communication with referring clinicians. The MET-RADS-P authors state that the new way of response categorization from 2 categories used currently, to 3 categories when assessing bone disease response, could lead to a paradigm shift from the current concept of treating patients to documentable progression (when tumor volume could be substantially greater than baseline), to being guided

by the presence or absence of benefit to therapy thus introducing more nuanced delivery of patient care.

MET-RADS-P template form

Response assessment categories (RACs)

An updated MET-RADS-P template form can be found in Figure 1 and is available as a pdf document at: www.siemens.com/magnetom-world.

The use of MET-RADS-P system starts by allocating the presence of unequivocal identified disease based on morphology and signal characteristics on all acquired images to 14 predefined regions of the body (primary disease, seven skeletal and three nodal regions, lung, liver and other soft tissue sites) at baseline and on follow-up assessments (see page 1 of the MET-RADS-P template form Figure 1A).

For follow-up studies, a response assessment on a scale of 1–5 indicating the likely response assessment category (RAC) for each location is recorded, comparing to the baseline study (RAC-1, indicating highly likely to be responding, up to RAC-5, indicating highly likely to be progressing).

The reporting guideline provides detailed explanations of the imaging criteria to be used to classify the likelihood of response in bones. Thus, RACs that summarize likelihood

of response in bone disease employ the newly developed MET-RADS criteria (Fig. 1B), but RACs for response in soft-tissues continues to use established standards already prescribed by RECIST v1.1 and PCWG guidance [7, 8].

For each region, only 2 RACs are needed to account for heterogeneity of responses that may occur in different anatomic areas. The primary RAC value (1–5) is based on dominant pattern of response within the region (that is, the response shown by more than half of the lesions within the region). A secondary RAC value (1–5) is assigned to the second most frequent pattern of response seen within the region.

A tertiary RAC value (4–5) maybe assigned to the region to illustrate progressing disease (i.e. RAC 4–5), if not already captured by the primary or secondary RAC values but this is not usually necessary in clinical practice.

When assessing a single lesion in a region, only the primary number category is used. Regions with multiple lesions all with the same pattern of response will have the same RAC value assigned as both the primary and secondary RACs. When equal numbers of lesions are category RAC 4/5 (progressing) as RAC 1/2/3 (responding & stable), then the primary pattern allocation is reserved for RAC 4/5 (the higher category). Similarly, when equal numbers of lesions are category RAC 1/2 as RAC 3, then the primary pattern allocation is reserved for RAC 3 (the higher category).

Overall response

The final response assessment consists of separately assessing the status of the primary disease, bones, nodes, and viscera without an overall patient response result. The overall patient assessment should be summarized in the text report which should accompany the MET-RADS-P template report (Figs. 2B, C).

Unlike regional response assessments which allocate RACs, the overall response for the primary tumor, nodal and visceral disease should be categorical, thus following established guidelines [7, 8], to improve communication with clinicians who are already familiar with this format. The following categories should be assigned: no disease (ND), complete response (CR), partial response (PR), stable disease (SD) and progressive disease (PD).

In contradistinction, the overall response of bone disease should be categorized on a scale of 1–5 indicating the likely overall response category: (1) highly likely to be responding, (2) likely to be responding, (3) stable, (4) likely to be progressing and (5) highly likely to be progressing.

Discordance or mixed response indicates the presence of progressing bone/soft tissue disease, not meeting definite progression criteria in the primary category, that is, when the majority of disease is stable or responding.

Discordant response should also be separately reported for primary, nodal, viscera and bone; evaluation of regional responses will enable the specific identification of the anatomic sites of mixed responses.

When discordant response is observed, the degree of discordance should be indicated major or minor to indicate in the evaluators opinion on whether alternative therapy options should be considered.

ADC value measurements should be made using a region-of-interest (ROI) technique on ADC images. Due to the lower spatial resolution of WB-MRI compared to CT scans, a 1.5 cm diameter threshold for bone lesions ROI is recommended for ADC measurements.

ADC measurements in bone disease should only be obtained from lesions that have sufficient signal intensity detected on all b-value images (including b0); otherwise the ADC values will be erroneous, reflecting only the noise in the images. Note that the absence of tissue signal on highest b-value images does not exclude tissues from ADC measurements because signal maybe present at lower b-values (thus, low or intermediate b-value images should be chosen instead for ROI placements).

Research components

Because of the need to unequivocally identify disease and to cope with the lower spatial resolution of WB-MRI compared to CT scans, a 1.5 cm diameter threshold for lesion size assessments is advised. Lesion size should be measured on anatomic T1-weighted images where possible.

Note that progression assignments for soft tissues, if based on measurements should be from baseline or the treatment induced summed measurement nadir, whichever is lower as per the RECIST v1.1 guidelines [7].

The type of progression (new disease versus growth of existing lesions) should be separately recorded; the location of progression can be accessible from the regional response assessments.

RACs at each time point should be compared to the baseline (pre-treatment) study for clinical use, but maybe referenced to the immediate prior study for research purposes if needed.

Whole-body tumor segmentations and histogram analysis are not part of the MET-RADS-P standard but can be used as ancillary tools if available (and are used in this paper for illustrative purposes only).

Worked up examples

An updated MET-RADS-P template form and detailed bone response assessment criteria can be found in Figure 1 and is available as a pdf document at www.siemens.com/magnetom-world.

Figures 2–4 illustrate the use of the MET-RADS-P standard in advanced, metastatic prostate cancer illustrated with examples of disease progression, responding and discordant responses.

The figures also demonstrate the utility of the WB-tumor load segmentation which is undertaken with the MR Total Tumor Load prototype, a released research software tool available on syngo.via Frontier (Siemens Healthcare,

Figure 3: Excellent response to chemotherapy

65-year-old male with metastatic castrate naive prostate cancer (mCNPC).
WB-MRI examinations before and after 4 cycles of docetaxel, goserelin and prednisolone therapy.

Figure 3A: There is improvement in the spinal canal narrowing in the mid-dorsal and lumbar spine on the T2W-FS images. The T1-weighted images are essentially unchanged or possibly minimally worse. There is also marked improved appearances of the bone and nodal disease on the paired WB b900 MIP images (inverted scale) and confirmed by significant increase in ADC values (see Figure 3C) of the bone lesions and reduction in size of the nodes.

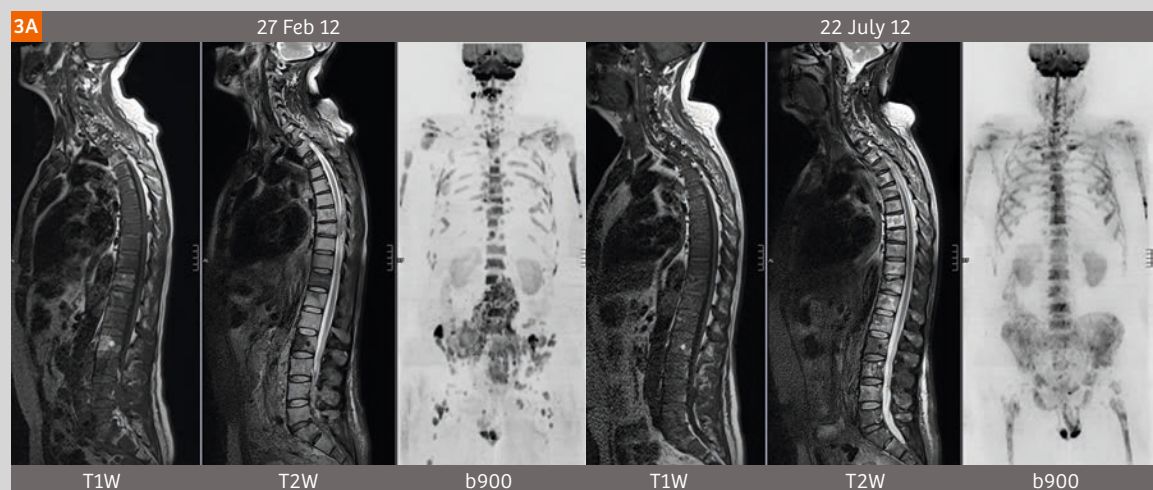


Figure 3B: Completed MET-RADS-P template report indicating sites of disease and RACs at each anatomical location compared to the baseline study. Note how the overall response at the primary tumor is indicated as no disease (previous radiotherapy). The overall pelvic nodal and retroperitoneal disease is excellent indicated as partial response (PR). The bone disease response is indicated by category 1 (highly likely to be responding).

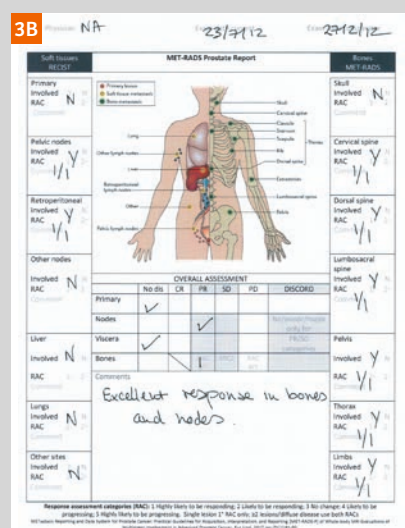


Figure 3C: WB-tumor load segmentation undertaken on syngo.via Frontier MR Total Tumor Load software (Siemens Healthcare; released research prototype – not part of the MET-RADS-P standard) for illustrative purposes only.

The whole-body b900 images are segmented using computed high b-value images of 1000 s/mm² and signal intensity threshold of approximately 30 AU. Extraneous signals (such as the brain, kidneys, bowel, gonads) are removed to leave only recognizable disease sites. The thresholded mask is overlaid with ADC value classes using the thresholds indicated and superimposed onto the b900 MIP images. The green voxels are values $\geq 1500 \mu\text{m}^2/\text{s}$ (representing voxels that are 'highly likely' to be responding). The yellow voxels are set to lie between the 95th centile ADC value of the pre-treatment histogram ($1067 \mu\text{m}^2/\text{s}$) and $1500 \mu\text{m}^2/\text{s}$ thus representing voxels 'likely' to be responding. Red-voxels represent mostly untreated disease.

1281 mL of bone marrow and retroperitoneal nodal disease were segmented before therapy and 430 mL on therapy. Note that there is marked global increase in ADC values ($705 \mu\text{m}^2/\text{s}$ and $1635 \mu\text{m}^2/\text{s}$) on the corresponding relative frequency histograms. There is a marked decrease in excess kurtosis of the histograms (9.0 and -0.60). Note decreased extent and volume of red-voxels consistent with disease response (95% before therapy and 17% after therapy). The residual red regions on the post therapy scan are presumed to represent residual disease with low ADC values in the lower lumbar spine and in the left proximal femur.

Figure 4: Discordant response to Radium-223 therapy

55-year-old male with metastatic castrate resistant prostate cancer (mCRPC). Previously failed treatments include docetaxel chemotherapy and abiraterone. Previously lumbar spinal radiotherapy. WB-MRI scans were obtained before and after Radium-223 treatment. Symptomatically the patient is worse with increasing bone pain and has become blood transfusion dependent; however PSA values are improved from 792 ng/mL to 167 ng/mL thus creating diagnostic confusion on the effectiveness of Radium-223 therapy.

Figure 4A: T1-weighted spine images show increased abnormal signal in the cervical, dorsal and lumbosacral spine suggestive of disease progression using the criteria in Figure 1B. However, the STIR sequence shows higher signal intensities in the cervical and dorsal spine indicating increased tissue water. Note increase in size of retro-peritoneal nodes (orange arrows).

Figure 4B: Responding disease in femora & dorsal spine, new disease in lumbar spine

Coronal b900 and ADC maps show decreased b900 signal intensities and increased ADC values in the dorsal spine and proximal femora (orange arrows) indicating responding disease (T1w-pseudo-progression in the dorsal spine). However, the opposite is seen in the lumbar spine where b900 signal intensity is increased (red arrows) and with low ADC values indicating new disease (true progression). Note some enlargement of the primary prostate tumor also (vertical red arrows).

Figure 4C: Paired b900 MIP images (inverted scale) showing new nodal disease in the left hemipelvis, retroperitoneum and in the left supraclavicular fossa (red arrows). On the other hand, the enlarged lymph nodes in the right common iliac region is improved (green arrow). There seems to be an increase in extent of bone marrow signal intensity. The high signal geographic lesion over the right thigh on the follow-up examination is a dipper pad (*). Note lower signal intensity of the brain on follow-up examination due to the absence of the head coil.

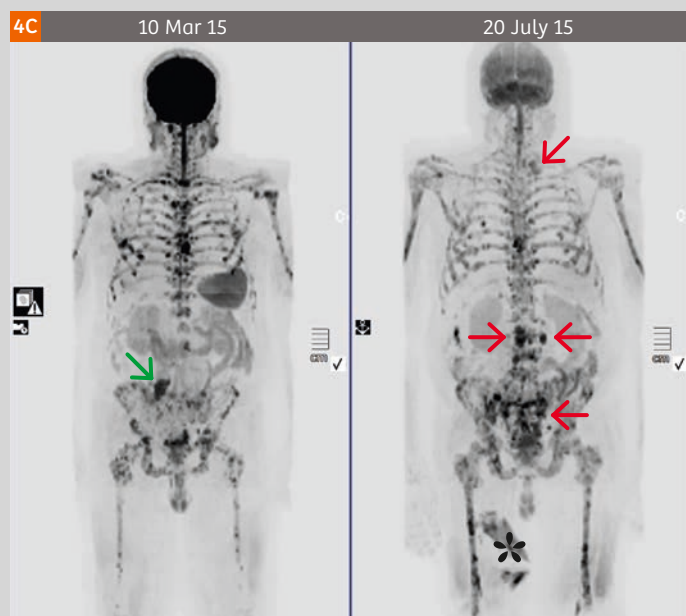
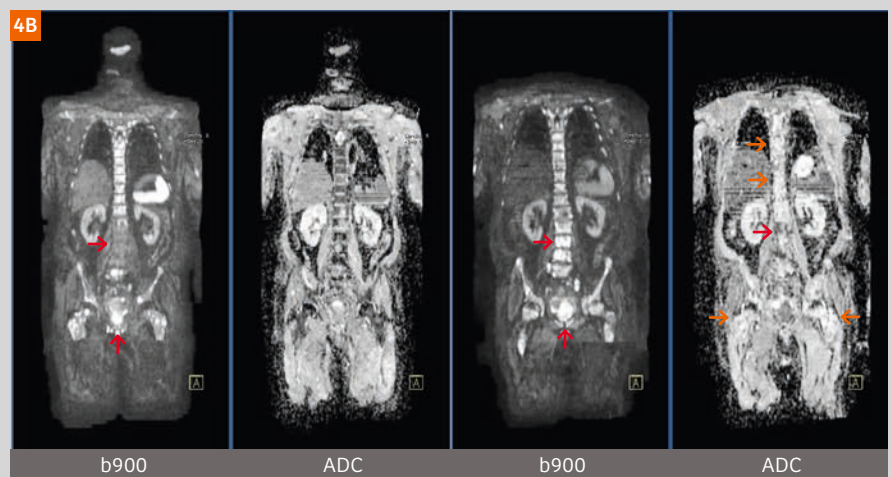
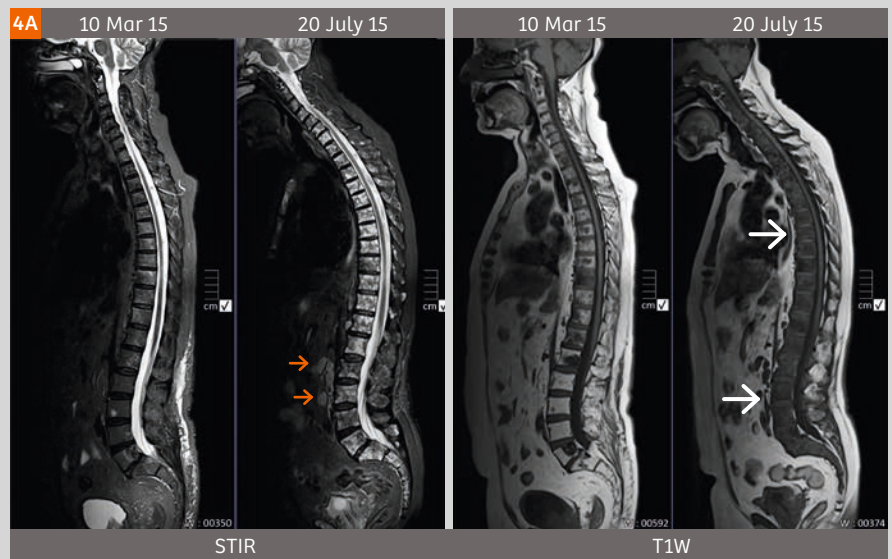


Figure 4D: Completed MET-RADS-P template report indicating sites of disease and RACs at each anatomical location compared to the baseline study. Note how the RAC of response at the primary tumor is mostly stable with some progression (RAC 3/4). The RAC of the pelvic nodes is indicated as 5/2 meaning that there is progression in the majority of the nodes although a single lymph node has responded (see also Figure 4E). Overall the bone disease is scored as 2 (likely to be responding in the majority of regions) with major discordance due to progression in lumbo-sacral spine and pelvis (both with RAC scores of 5/5).

4D Physician *Po* Exam date *20/11/15* Exam *1873/15*

MET-RADS Prostate Report

Soft Tissues RECIST

Primary Involved RAC *Y* *3/4*

Pelvic nodes Involved RAC *Y* *5/2*

Retroperitoneal Involved RAC *Y* *5/5*

Other nodes Involved RAC *Y* *5/5*

Liver Involved *N* *0/0*

Lungs Involved *N* *0/0*

Other sites Involved *N* *0/0*

Bones MET-RADS

Skull Involved RAC *N* *0/0*

Cervical spine Involved RAC *Y* *2/3*

Dorsal spine Involved RAC *Y* *2/3*

Lumbosacral spine Involved RAC *Y* *5/5*

Pelvis Involved RAC *Y* *5/5*

Thorax Involved RAC *Y* *3/5*

Limbs Involved RAC *Y* *5/2*

OVERALL ASSESSMENT

Primary: No dis, CR, PR, SD, PD, DISCORD

Nodes: No/minor/major, PD/SD, Category

Viscera: *✓*

Bones: *2*

Comments: *Progression in nodes. Response (stable/progressive) in dorsal spine but true progression in lumbar spine.*

Response assessment categories (RAC): 1 Highly likely to be responding; 2 Likely to be responding; 3 No change; 4 Likely to be progressing; 5 Highly likely to be progressing. Single lesion 1* RAC only; 22 lesions/diffuse disease use both RACs

Figure 4E: WB-tumor load segmentation undertaken on syngo.via Frontier MR Total Tumor Load software (Siemens Healthineers; released research prototype – not part of the MET-RADS-P standard) for illustrative purposes only.

The whole-body b900 images are segmented using computed high b-value images of 1000 s/mm² and signal intensity threshold of approximately 100 AU. Extraneous signals (such as the brain, kidneys, bowel, gonads) are removed to leave only recognizable disease sites. The color the b900 MIP images are overlaid with ADC value classes using the thresholds indicated. The green voxels are values $\geq 1500 \mu\text{m}^2/\text{s}$ (representing voxels that are 'highly likely' to be responding). The yellow voxels are set to lie between the 95th centile ADC value of the pre-treatment histogram (1208 $\mu\text{m}^2/\text{s}$) and 1500 $\mu\text{m}^2/\text{s}$ thus representing voxels 'likely' to be responding. Red-voxels represent mostly untreated disease.



570 mL of bone marrow and nodal disease are segmented before therapy and 538 mL on therapy. Note that there is moderate global increase in ADC values (670 $\mu\text{m}^2/\text{s}$ and 920 $\mu\text{m}^2/\text{s}$) on the corresponding relative frequency histograms. There is a decrease in excess kurtosis of the histograms (2.2 and -0.05). Note decrease extent and volume of red-voxels consistent with disease response (95% before therapy and 76% after therapy). Heterogeneity of response in the spine (more red voxels in the lumbar spine and more green voxels in the dorsal spine) and in the pelvis is appreciable on these color projected images. This heterogeneity of response emphasizes the need to evaluate all the relevant WB-MRI images and to apply regional responses using the MET-RADS-P criteria.

Erlangen, Germany; released research prototype). Note that tumor load and ADC histogram analysis is not part of the MET-RADS-P standard, and is included for illustrative and cross-correlations purposes only. Detailed working of the *syngo.via* Frontier MR Total Tumor Load software is described in an accompanying article by Robert Grimm and Anwar R. Padhani in this issue of MAGNETOM Flash.

Conclusions and future developments

The MET-RADS-P system provides the minimum standards for whole-body MR with DWI image acquisition, interpretation, and reporting of both baseline and follow-up monitoring examinations of men with advanced, metastatic prostate cancer. MET-RADS-P is suitable for guiding patient care in practice (using the regional and overall assessment criteria), but can also be incorporated into clinical trials when accurate lesion size and ADC measurements become more important (thus, recording of measurements is not mandated for clinical practice). MET-RADS-P enables the evaluation of the benefits of continuing therapy to be assessed, when there are signs that the disease is progressing (discordant responses).

MET-RAD-P requires validation within clinical trials initially in studies that assess the effects of known efficacious treatments, such as those targeting the androgen axis, cytotoxic chemotherapy, Radium-223 and PARP inhibitors. METRADS-P measures should be correlated to other tumor response biomarkers delineated by PCWG (such as PSA declines), quality of life measures, rates of skeletal events, radiographic progression free survival and overall survival. The latter will be needed for the introduction of WB-MRI into longer term follow-up studies that will allow objective

assessments of whether WB-MRI is effective in supporting patient care. Thus, we recommend that MET-RADS-P is now evaluated in clinical care and trials, to assess its impact on the clinical practice of advanced prostate cancer.

References

- 1 Lecouvet FE. Whole-Body MR Imaging: Musculoskeletal Applications. *Radiology*. 2016;279:345–365.
- 2 Padhani AR, Lecouvet FE, Tunariu N, et al. Rationale for Modernising Imaging in Advanced Prostate Cancer. *Eur Urol Focus*. European Association of Urology; 2016;44:198–205.
- 3 Dimopoulos M a., Hillengass J, Usmani S, et al. Role of magnetic resonance imaging in the management of patients with multiple myeloma: a consensus statement. *J Clin Oncol*. 2015;33:657–664.
- 4 Padhani AR, Lecouvet FE, Tunariu N, et al. METastasis Reporting and Data System for Prostate Cancer : Practical Guidelines for Acquisition , Interpretation , and Reporting of Whole-body Magnetic Resonance Imaging-based Evaluations of Multiorgan Involvement in Advanced Prostate Cancer. *Eur Urol*. European Association of Urology; 2017;71:81–92.
- 5 Mottet N, Bellmunt J, Bolla M, et al. EAU-ESTRO-SIOG Guidelines on Prostate Cancer. Part 1: Screening, Diagnosis, and Local Treatment with Curative Intent. *Eur Urol*. 2016;1–12.
- 6 Cornford P, Bellmunt J, Bolla M, et al. EAU-ESTRO-SIOG Guidelines on Prostate Cancer. Part II: Treatment of Relapsing, Metastatic, and Castration-Resistant Prostate Cancer. *Eur Urol*. 2016;1–13.
- 7 Eisenhauer EA, Therasse P, Bogaerts J, et al. New response evaluation criteria in solid tumours: revised RECIST guideline (version 1.1). *Eur J Cancer*. 2008/12/23. 2009;45:228–247.
- 8 Scher HI, Morris MJ, Stadler WM, et al. Trial Design and Objectives for Castration-Resistant Prostate Cancer: Updated Recommendations From the Prostate Cancer Clinical Trials Working Group 3. *J Clin Oncol*. 2016;34:1402–1418.

Contact

Professor Anwar R. Padhani
MB, BS, FRCP, FRCR
Paul Strickland Scanner Centre
Mount Vernon Hospital

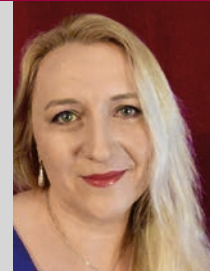
Rickmansworth Road
Northwood, Middlesex HA6 2RN
United Kingdom
anwar.padhani@stricklandscanner.org.uk



Contact

Nina Tunariu
MD MRCP FRCR MDR
Royal Marsden NHS Foundation Trust &
Institute of Cancer Research
Cancer Research UK Cancer Imaging Centre

Downs Road, Sutton, Surrey, SM2 5PT
United Kingdom
Nina.Tunariu@icr.ac.uk



Visit us at

www.siemens.com/magnetom-world

to download the MET-RADS-P template form.

Name	ID	DOB												
Physician	Exam date current	Exam date comparator												
<table border="1"> <thead> <tr> <th>Soft tissues RECIST</th> <th>MET-RADS Prostate Report</th> <th>Bones MET-RADS</th> </tr> </thead> <tbody> <tr> <td> Primary Involved RAC Comment </td> <td> </td> <td> Skull Involved RAC Comment Cervical spine Involved RAC Comment Dorsal spine Involved RAC Comment </td> </tr> <tr> <td> Pelvic nodes Involved RAC Comment </td> <td></td> <td></td> </tr> <tr> <td> Retroperitoneal Involved RAC Comment </td> <td></td> <td></td> </tr> </tbody> </table>			Soft tissues RECIST	MET-RADS Prostate Report	Bones MET-RADS	Primary Involved RAC Comment		Skull Involved RAC Comment Cervical spine Involved RAC Comment Dorsal spine Involved RAC Comment	Pelvic nodes Involved RAC Comment			Retroperitoneal Involved RAC Comment		
Soft tissues RECIST	MET-RADS Prostate Report	Bones MET-RADS												
Primary Involved RAC Comment		Skull Involved RAC Comment Cervical spine Involved RAC Comment Dorsal spine Involved RAC Comment												
Pelvic nodes Involved RAC Comment														
Retroperitoneal Involved RAC Comment														



HyperArc™
High Definition
Radiotherapy*



MAGNETOM
RT Pro edition



"The partnership between Siemens Healthineers and Varian provides access to the latest innovative technology and helps the medical community to increase the benefits for patients."

Ernesto Roesler, MD

Hospital Real Portugues, Recife, Brazil

Mission: EnVision **better cancer care** **with intracranial HD Radiotherapy**

Varian and Siemens Healthineers work together as strategic partners. Siemens' advanced diagnostic imaging capabilities coupled with Varian's powerful delivery systems and treatment planning tools give even more of an edge in the pursuit of our common goal: to EnVision better cancer care. Together we offer more personalized treatment and

expanded care options that aid you in making the best possible decisions for your patients – with confidence. By gathering our strengths, we have the energy and vision to better help healthcare professionals detect, diagnose and treat cancer while paving the way for the future of cancer care.

**Our partnership not only brings us together,
it helps shape the future of cancer care.**

*Not all products are available for sale in all markets and are subject to change. Courtesy of Varian Medical Systems

The statements by Siemens' customers presented here are based on results that were achieved in the customer's unique setting. Since there is no 'typical' hospital and many variables exist (e.g., hospital size, case mix, level of IT adoption), there can be no guarantee that other customers will achieve the same results.

Observing Endocrine Therapy Resistance in Metastatic Breast Cancer with Whole-body MRI

Anwar R. Padhani

Paul Strickland Scanner Centre, Mount Vernon Hospital, Northwood, Middlesex, UK

Introduction

Approximately 70% of breast cancers are estrogen receptor (ER) positive, and are, therefore, treated with endocrine therapies. However, about 25% of patients with primary disease and almost all patients with metastases will present with or eventually develop endocrine resistance [1]. The mechanisms underlying the development of resistance remain largely unknown but in the last 2 years, several studies have shown ER independent gain-of-function mutations in ESR1, the gene that encodes the ER, in approximately 20–30% of patients with metastatic ER-positive disease who received endocrine therapies, such as tamoxifen and aromatase inhibitors. These mutations lead to ligand-independent ER activity that promotes tumor growth, promoting resistance to endocrine therapy, and potentially enhancing metastatic ability. The emergence of endocrine therapy resistance via this mechanism suggests that, under selective treatment pressure, clonal expansion of rare mutant clones occurs, thus contributing to resistance. Rationale-based novel therapeutic strategies that target these ESR1 mutants have the potential to improve treatment outcomes for patients. Fulvestrant

is a hormonal therapy that specifically targets the ESR1 mutation, that seems to work well in metastatic breast cancer patients with endocrine resistance. Multiple studies suggest greater therapy efficacy in those with bone disease.

In this case study, we demonstrate the potential of quantitative whole-body MR imaging (WB-MRI) to monitor response of breast cancer to hormonal therapy, showing that (1) morphological response does not work as well as diffusion MRI for monitoring response to therapy, (2) that ADC histogram analyses can depict the emergence of treatment resistance, and (3) that spatially discordant response to targeted therapy can emerge when bone disease is effectively treated.

Patient history

50-year-old woman with metastatic invasive breast cancer, ER positive and HER-2 neu negative disease was initially treated with first line hormonal therapy (Exemestane, Goserelin) and bisphosphonates (Zoledronic acid) for bone only metastatic disease. She was switched to 2nd line hormonal therapy with Fulvestrant and Zoledronic on bone disease progression, with good response in her bone disease

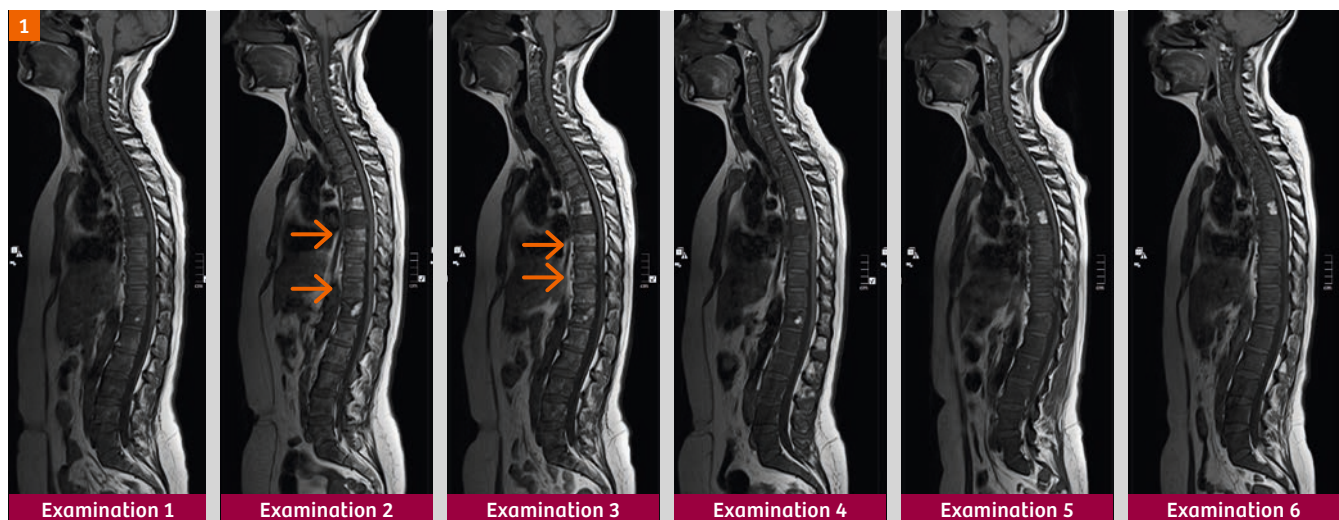


Figure 1: Whole-spine T1-weighted images show diffuse bone marrow infiltration with some return of bone marrow fat on examinations 2 and 3 (arrows) with first-line hormonal therapy. The bone marrow fat disappears at therapy relapse on examination 4 and no further T1w changes are detected after therapy change to second-line on examinations 5 and 6. There is a hemangioma in T6.



Figure 2: Whole-spine STIR show diffuse bone marrow infiltration with subtle increases in signal intensity with first-line therapy on examinations 2 and 4, but signal intensity lowers by examination 4 at the time of disease relapse (relapse). The bone marrow signal increases again after change to second-line hormonal therapy on examinations 5 and 6. These increases in bone marrow signal intensity are consistent with alternations in tissue water associated with the cell kill mechanism of hormonal treatment (apoptosis).

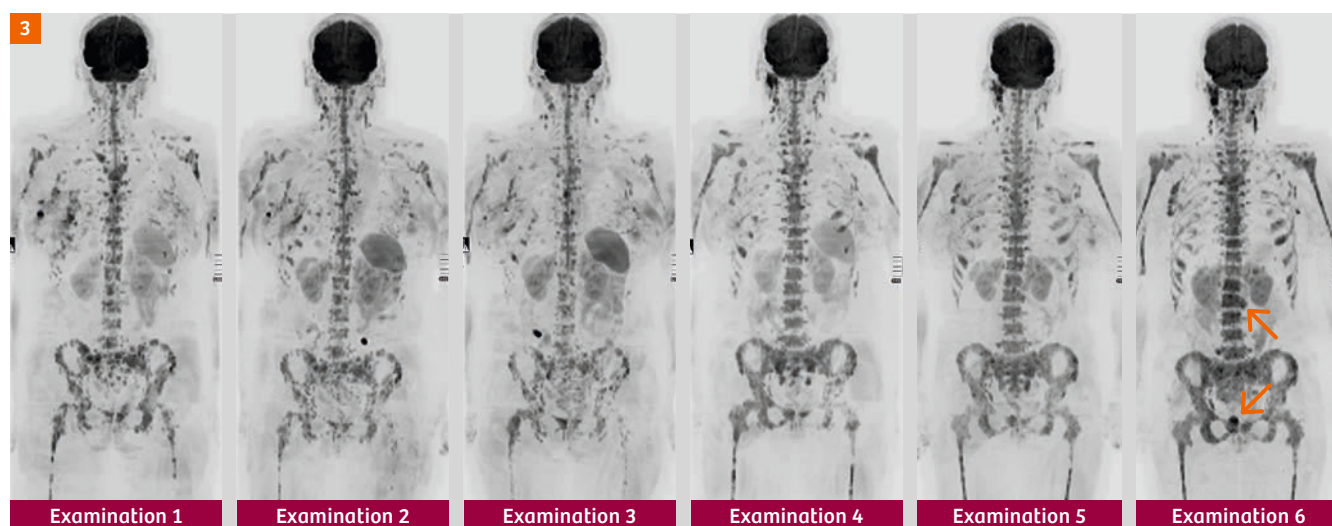


Figure 3: Whole-body b900 3D MIP (inverted scale). The bone marrow is diffusely involved with multiple small focal and confluent regions of high-signal intensity in the axial skeleton and in the proximal limb bones. The primary right-sided breast cancer is *in-situ* with axillary nodal disease visible also. Decreases in the signal intensity of bone marrow with first-line therapy can be seen to occur slowly, but there are focal areas of persistent hyperintensities indicating the likely presence of active disease (examination 3). On examination 4, full-blown relapse can be seen, indicated by increases in signal intensity extent in the bones (see article by Padhani & Tunariu on page 64 in this MAGNETOM Flash for progression criteria for bone disease). On changing to second-line hormonal therapy, no response can be confidently identified but there is increasing disease in the anterior ribs, on the left side of L2 and pubic symphysis (arrows).

only shown on quantitative diffusion imaging. Unfortunately, she also developed liver and pancreas metastases needing further therapy change to chemotherapy. No regional radiotherapy has been administered.

Serial examinations with whole-body diffusion MRI were undertaken using published protocols [2]. Whole-body diffusion sequences using b-values of b50, b600 and

900 s/mm² were undertaken together with spinal T1-weighted and STIR sequences, to monitor response to treatment. Six examinations were performed in total. Following the baseline examination, three further examinations were done while on first-line hormonal therapy and two examinations while on second-line hormonal therapy.

Figure 4: WB-tumor load segmentations were undertaken on syngo.via Frontier MR Total Tumor Load software (Siemens Healthcare, Erlangen, Germany; released research prototype). The whole-body b900 images are segmented using computed high b-value images of 1000–1200 s/mm², setting a signal intensity threshold of approximately 100 AU. Extraneous signals (such as the brain, kidneys and bowel) are removed, to leave only recognizable bone disease sites including the right breast and axilla. The color the b900 MIP images are overlaid with ADC value classes using the following thresholds. The green voxels are values $\geq 1500 \mu\text{m}^2/\text{s}$ (representing voxels that are ‘highly likely’ to be responding). The yellow voxels are set to lie between the 95th centile ADC value of the pre-treatment (examination 1 or examination 4) histograms (1256 and 1127 $\mu\text{m}^2/\text{s}$ respectively) and 1500 $\mu\text{m}^2/\text{s}$. Thus, yellow voxels represent regions ‘likely’ to be responding. Red voxels represent mostly areas that are untreated disease or have no detected response.

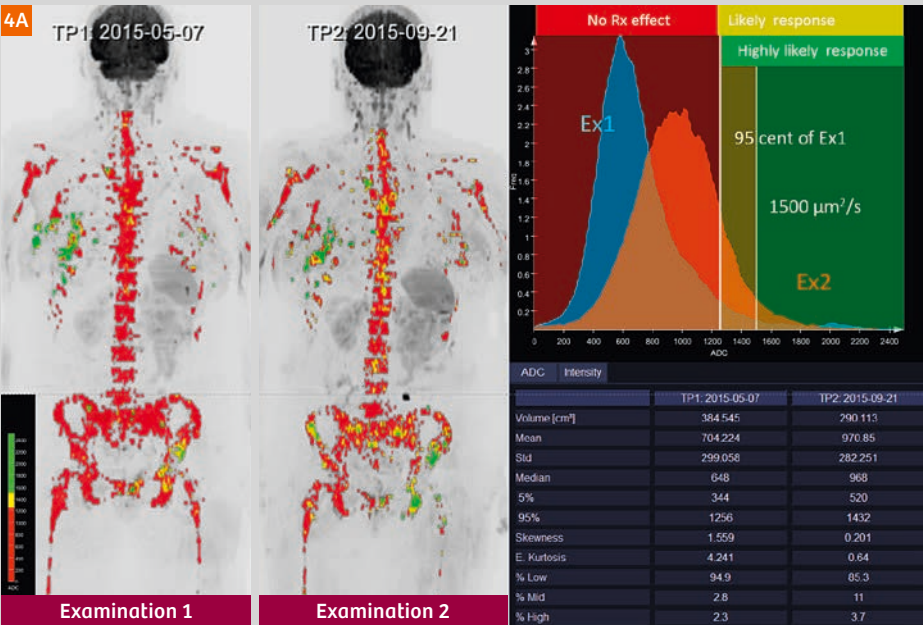


Figure 4A: Histogram analysis of examination 1 and 2. 384 ml of tumor was segmented before therapy and 290 ml on therapy. Note that there is a significant global increase in ADC values (704 $\mu\text{m}^2/\text{s}$ and 971 $\mu\text{m}^2/\text{s}$) and a decrease in kurtosis (4.2 and 0.6) on the corresponding relative frequency histograms indicating some response on a whole-body basis. Note increasing numbers of yellow and green voxels occurring in patches (for example the left hip – note no radiotherapy has been given). These appearances taken with morphologic assessments indicate a favourable response overall with no evidence of progression.

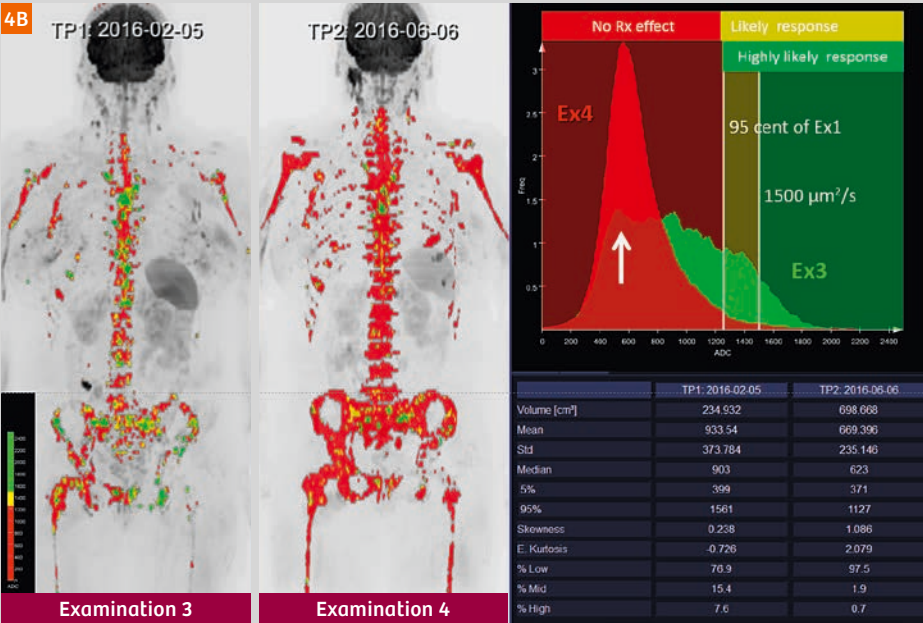


Figure 4B: Histogram analysis of examination 3 and 4. 235 ml of tumor was segmented on examination 3 and 698 ml on examination 4 at disease relapse. Note that on examination 3 there is a flattened histogram (green histogram) with a significant global increase in ADC values (933 $\mu\text{m}^2/\text{s}$) compared to baseline and a marked decreased kurtosis (-0.7) on the relative frequency histograms, indicating a good response to first-line hormonal therapy. Note increasing numbers of yellow and green voxels. These appearances taken with morphologic assessments indicate a good response overall. However, note persistent red voxels on examination 3 and a corresponding peak on the examination 3 histogram, indicating areas of therapy resistance (vertical white arrow). On examination 4, the patient has relapsed with a histogram that is identical to the baseline pretherapy study (examination 1).

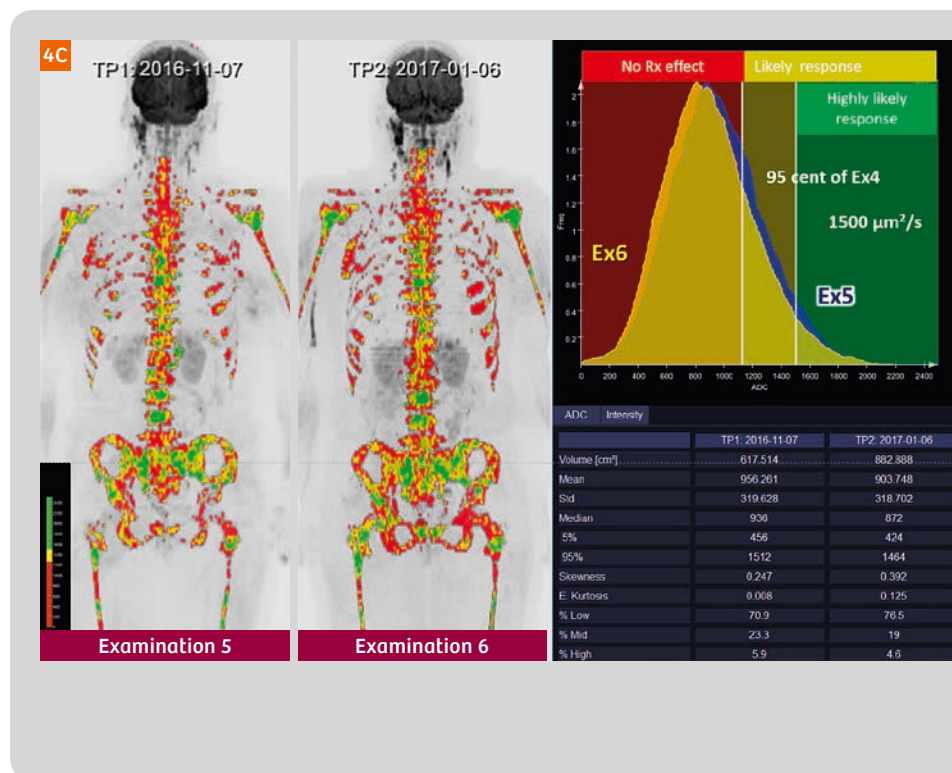


Figure 4C: Histogram analysis of examination 5 and 6.

617 ml of tumor was segmented on examination 5 and 883 ml on examination 6. Note that on both examinations, the histograms show significant global increases in ADC values (956 and 904 $\mu\text{m}^2/\text{s}$) compared to examination 4 (pre-second-line treatment baseline) indicating a good response to second-line hormonal therapy. The diffusion imaging appearances indicate a good response overall not observable on the T1w spine images. However, note that there are persistent red voxels on both examinations 5 and 6, indicating persistent areas of therapy resistance in the bones. Note also increased volume of right axillary nodal disease. Therapy was changed because of new liver and pancreatic metastases.

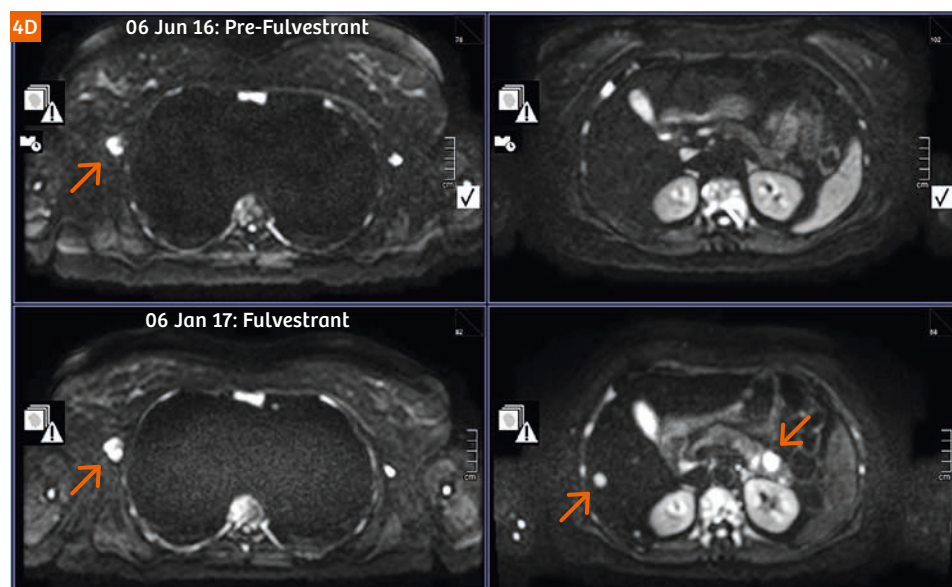


Figure 4D: Axial b900 images of the upper abdomen for examinations 4 (pre-second-line hormonal therapy) and 6 show the emergence of new disease in liver and pancreas (arrows), resulting in a change to chemotherapy therapy. Right axillary nodes are also enlarging.

References

- 1 Jeselsohn R, Buchwalter G, De Angelis C, Brown M, Schiff R. ESR1 mutations – a mechanism for acquired endocrine resistance in breast cancer. *Nat Rev Clin Oncol*. 2015;12:573–583.
- 2 Padhani AR, Lecouvet FE, Tunariu N, et al. METastasis Reporting and Data System for Prostate Cancer : Practical Guidelines for Acquisition , Interpretation , and Reporting of Whole-body Magnetic Resonance Imaging-based Evaluations of Multiorgan Involvement in Advanced Prostate Cancer. *Eur Urol*. European Association of Urology; 2017;71:81–92.

Contact



Professor Anwar R. Padhani
MB, BS, FRCP, FRCR
Paul Strickland Scanner Centre
Mount Vernon Hospital

Rickmansworth Road
Northwood, Middlesex HA6 2RN
United Kingdom
anwar.padhani@
stricklandscanner.org.uk

Whole-body Diffusion-weighted MR Image Analysis with syngo.via Frontier MR Total Tumor Load

Robert Grimm¹, Anwar R. Padhani²

¹ Siemens Healthineers, Erlangen, Germany

² Paul Strickland Scanner Centre, Mount Vernon Hospital, Northwood, Middlesex, UK

Whole-body diffusion-weighted MRI has recently gained a lot of attention as a promising technique for the assessment of multifocal bone disease such as multiple myeloma and bone metastases from breast and prostate cancer [1–3]. Compared to other imaging techniques, diffusion-weighted MRI has a high sensitivity and specificity for disease detection, without exposing the patient to ionizing radiation. Uniquely, diffusion imaging also enables therapy response to be evaluated, with particular application for bone disease. However, one challenge is the relatively large effort in response interpretation, due to the number of images that are generated and the lack of tools for efficient evaluation for multifocal disease.

This limitation was addressed by an efficient analysis approach that has been proposed by Blackledge et al. [4], using a threshold-based segmentation on diffusion-weighted images to identify regions of disease. Based on this segmentation, the overall tumor volume as well as histogram metrics of the corresponding apparent diffusion coefficient (ADC) maps are analyzed. Excellent inter- and intra-observer agreement of this computed approach was demonstrated recently in a pilot study [5].

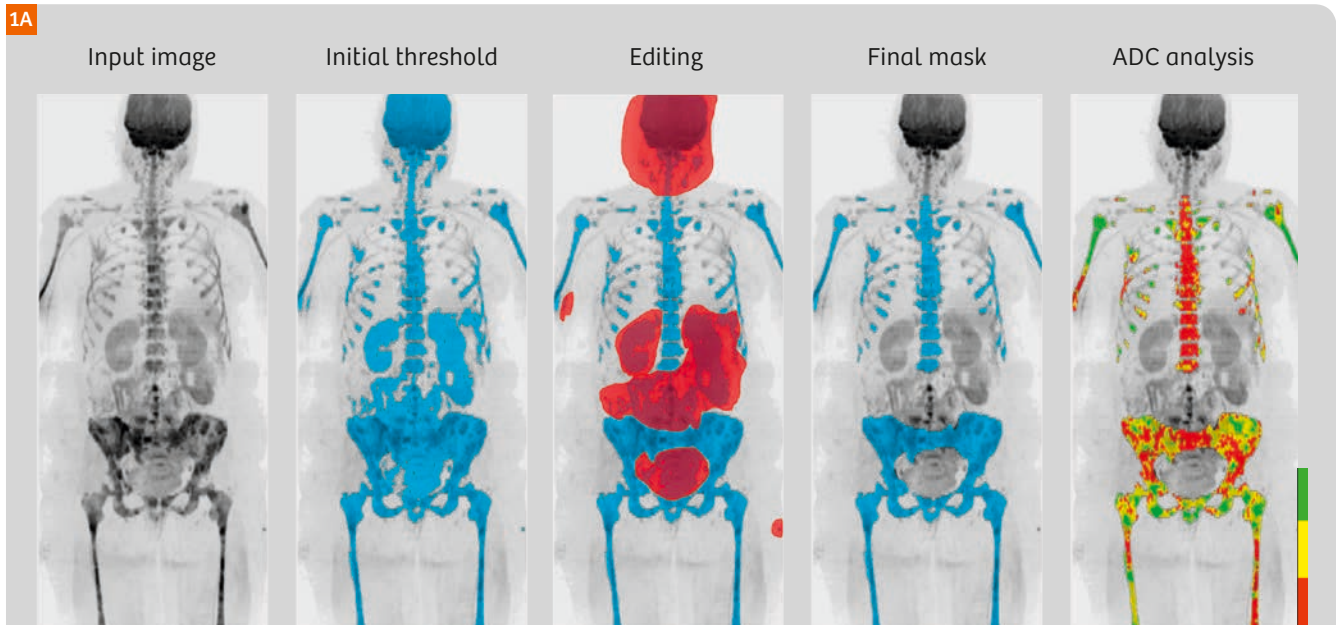
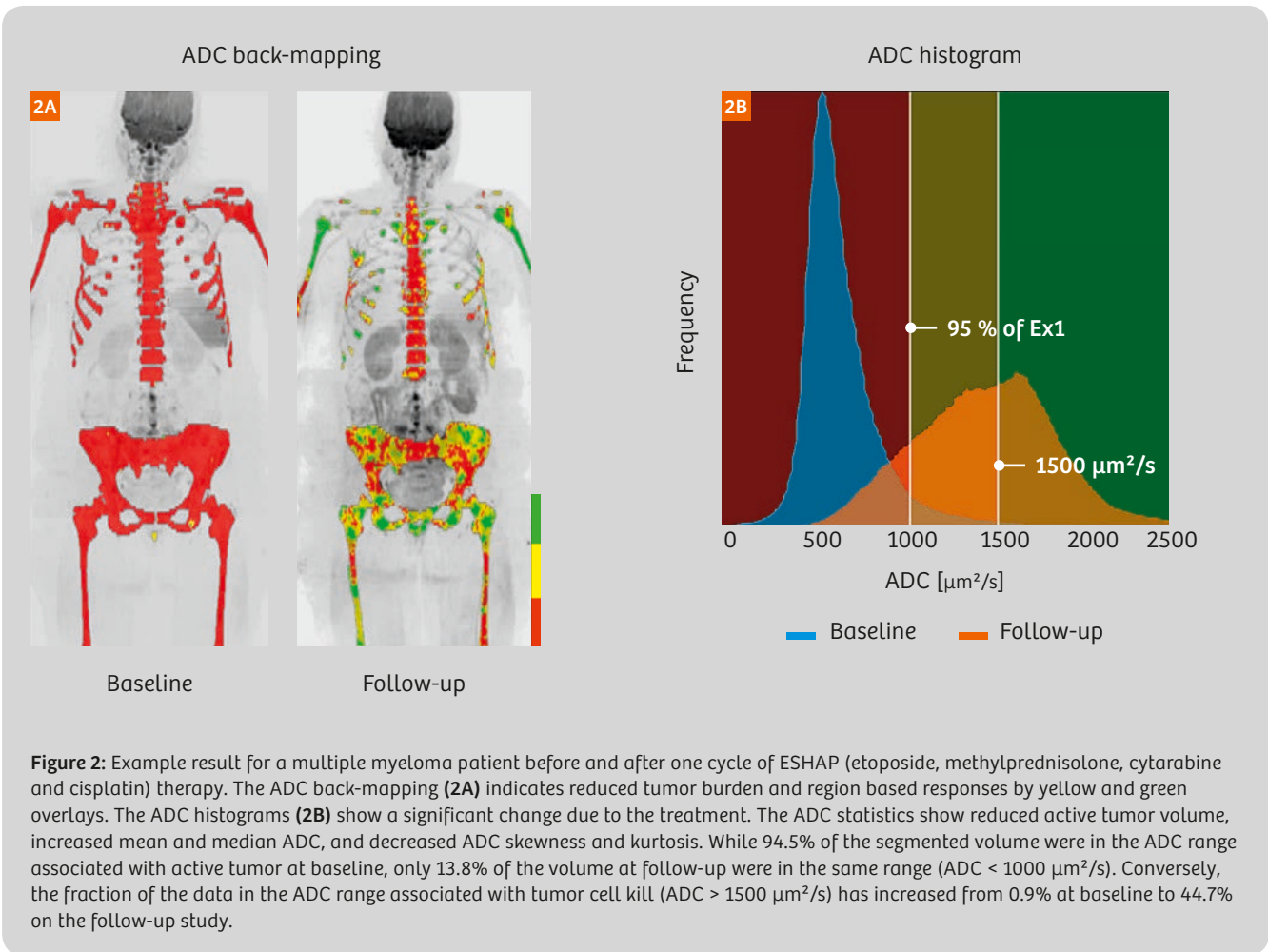


Figure 1: Application workflow. A computed high b-value image ($b = 800 \text{ s/mm}^2$) serves as input. An initial segmentation of the multiple myeloma lesions is obtained by thresholding and then edited to manually exclude regions from the analysis. In this case the brain, neck nodes, salivary glands, kidneys, spleen, and pelvic bowel were removed. Furthermore, the lower lumbar spine was removed, because of artifacts from a spine stabilization. Finally, back-mapping analysis reveals the ADC associated with each voxel, and provides detailed ADC histogram metrics (see also Figure 2).



Quantitative whole-body diffusion MRI is implemented in the *syngo.via* Frontier MR Total Tumor Load¹ released research prototype: It uses diffusion-weighted images as input and allows creation of a 3D mask on diffusion images, for the analysis of the corresponding ADC maps. The prototype supports evaluation of up to two time-points, side-by-side and utilizes maximum intensity projections (MIPs) to facilitate efficient visual assessment of the intermediate result at each step. The workflow is structured in three steps, as depicted in Figure 1. The example illustrates the processing steps for a patient with multiple myeloma:

- 1. Initial segmentation:** An initial mask is defined interactively by applying a threshold to a computed high b-value image (for example, $b = 800 \text{ s/mm}^2$). An automatic outlier removal can be performed to reduce false positive voxels due to artifacts or T2 shine-through.
- 2. Mask editing:** The initial mask is edited by the user. The user can perform volume punching in order to exclude artifact regions and normal hyperintense organs such

as brain, kidneys, spleen, testes, salivary glands etc, or users can choose to retain only a selected volume of interest. Furthermore, a volumetric, semi-automatic segmentation tool is available for manually adding false negative regions to the mask if not already captured.

Metric	Baseline	Follow-up
Volume [cm^3]	1298	978
ADC mean [$\mu\text{m}^2/\text{s}$]	653	1432
ADC median [$\mu\text{m}^2/\text{s}$]	609	1437
ADC skewness	2.11	0.12
ADC e. kurtosis	8.21	0.07
% Low	94.5	13.8
% High	0.9	44.7

Table 1: Segmentation statistics. The tumor volume as well as several histogram metrics have changed significantly during treatment.

¹ *syngo.via* Frontier is for research only, not a medical device.

3. **Analysis:** The ADC histogram and corresponding statistics are computed for the edited masked volume. Histogram metrics include mask volume, mean, median, standard deviation, skewness, excess kurtosis, and customizable percentiles.

Regions of low, intermediate and high ADC values can be inspected interactively by adjusting slider positions on the histogram. Depending on the ADC chosen, the colored back-mapping ADC overlays allow the visual discrimination of regions with untreated disease (typically associated with lower ADC values) compared to disease regions that have been treated effectively (high ADC values).

In the example shown in Figure 2, the 95th percentile of the baseline examination, approximately 1000 $\mu\text{m}^2/\text{s}$, was used as lower ADC threshold and 1500 $\mu\text{m}^2/\text{s}$ was used as upper threshold. The ADC back-mapping in Figure 2A shows a red overlay for voxels with an ADC below 1000 $\mu\text{m}^2/\text{s}$, a yellow overlay for voxels in the intermediate range, and a green overlay for voxels above 1500 $\mu\text{m}^2/\text{s}$. The corresponding histograms and limits are shown in Figure 2B. The patient shows changes consistent with a significant response to the therapy, indicated by the emergence of mixed yellow and green regions in the humeri, pelvis, and femur. However, red regions continue to be seen indicating the continued presence of untreated disease.

The histogram statistics, listed in Table 1, show a reduction of the total diffusion volume, from 1298 cm^3 at baseline to 978 cm^3 at follow-up, and a radical change in the histogram shape. The mean and median values have increased from 653 (609) $\mu\text{m}^2/\text{s}$ at baseline to 1432 (1437) $\mu\text{m}^2/\text{s}$ in the follow-up examination. The skewness decreased from 2.11 to 0.12, while the excess kurtosis decreased from 8.21 to 0.07.

Further examples obtained with the *syngo.via* Frontier MR Total Tumor Load¹ released research prototype software can be found in the article “*Metastatic Prostate Cancer in Practice – the MET-RADS-P Imaging Response System Using Whole-body MRI*” on page 64 and in the case study “*Observing Endocrine Therapy Resistance in Metastatic Breast Cancer with Whole-body MRI*” on page 80 of this issue of MAGNETOM Flash.

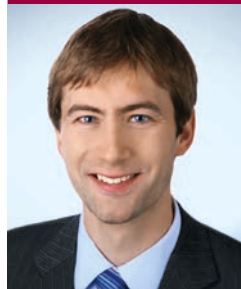
To summarize, the *syngo.via* Frontier MR Total Tumor Load released research prototype provides an efficient and reproducible workflow with quantitative results for the processing and analysis of whole-body diffusion-weighted images in the response assessment setting. It is a promising tool to support the standardization of whole-body MRI for treatment response monitoring of bone disease in particular. Extensions like a fully automatic bone segmentation (as described in “*Whole-body MRI Reading and Bone Assessment with syngo.via Frontier MR Bone Scan*” on

page 76 in this issue), simultaneous consideration of other MR parameters such as the normalized signal intensity, fat fraction, or Gadolinium enhancement fraction [6, 7], and integrated classification techniques to detect and separate regions of discordant response [7], may further add to the potential of the technique to promote high-precision medicine.

References

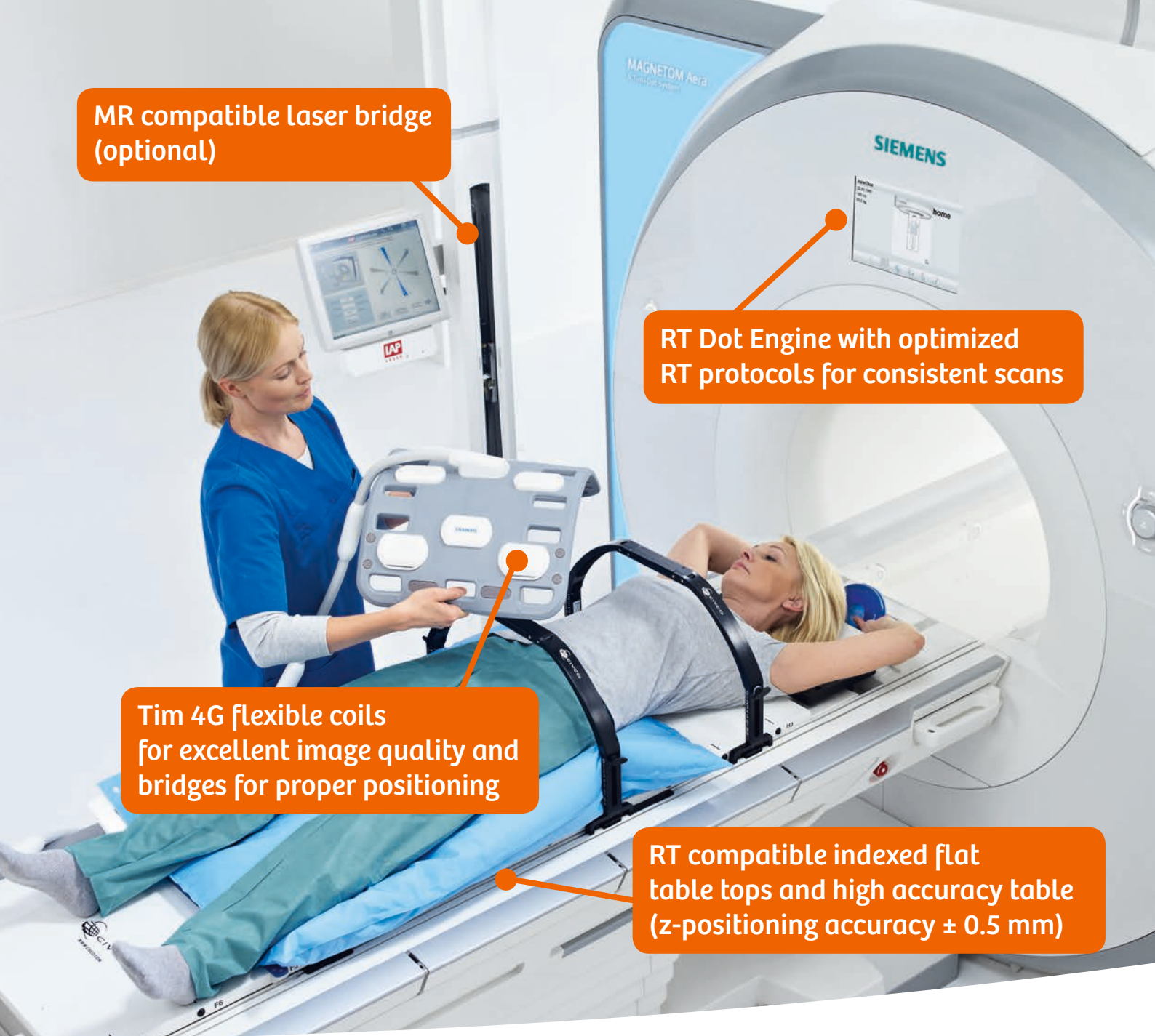
- 1 Pawlyn C, Fowkes L, Otero S, et al. Whole-body diffusion-weighted MRI: a new gold standard for assessing disease burden in patients with multiple myeloma? *Leukemia*. 2016;30(6):1446-1448. doi:10.1038/leu.2015.338.
- 2 Padhani AR, Lecouvet FE, Tunariu N, Koh DM, De Keyzer F, et al. (2016) Rationale for Modernising Imaging in Advanced Prostate Cancer. *European Urology Focus*, Available online. doi:10.1016/j.euf.2016.06.018.
- 3 Padhani AR and Tunariu N, Metastatic response system in using whole body MRI for prostate cancer in practice. See also page 76 in this issue of MAGNETOM Flash.
- 4 Blackledge MD, Collins DJ, Tunariu N, Orton MR, Padhani AR, et al. (2014) Assessment of Treatment Response by Total Tumor Volume and Global Apparent Diffusion Coefficient Using Diffusion-Weighted MRI in Patients with Metastatic Bone Disease: A Feasibility Study. *PLOS ONE* 9(4): e91779. doi: 10.1371/journal.pone.0091779.
- 5 Blackledge MD, Tunariu N, Orton MR, Padhani AR, Collins DJ, et al. (2016) Inter- and Intra-Observer Repeatability of Quantitative Whole-Body, Diffusion-Weighted Imaging (WBDWI) in Metastatic Bone Disease. *PLOS ONE* 11(4): e0153840. doi: 10.1371/journal.pone.0153840
- 6 Amlani A, Ghosh-Ray S, van Ree K, Makris A, D'Sa S, Ostler P, Anyamene N, Padhani AR. Relationships Between Diffusion Weighted Signal Intensity, ADC and Water/fat Content of Malignant Bone Marrow. Program Number: 3447. Proceedings of the International Society of Magnetic Resonance in Medicine. 20th Scientific Meeting and Exhibition, Salt Lake City, May 2013.
- 7 Blackledge MD, Leach M, Rata M, Tunariu N, Koh DM, et al. (2016) Visualizing whole-body treatment response heterogeneity using multi-parametric magnetic resonance imaging. *Journal of Algorithms & Computation Technology*, in press. doi: 10.1177/1748301816668024.

Contact



Robert Grimm, Ph.D.
Siemens Healthcare GmbH
HC DI MR PI TIO ONCO

Postbox 32 60
91050 Erlangen
Germany
Phone: +49 (0) 9131 84-2717
robertgrimm@siemens.com



Advance your
clinical capabilities
with the **MAGNETOM RT Pro edition**

For more information please visit us at: [siemens.com/mri](https://www.siemens.com/mri)

Go to: **MRI in Therapy > MAGNETOM RT Pro edition**

Whole-body MR Image Reading and Bone Assessment with syngo.via Frontier MR Bone Scan

Matthias Fenchel¹; Anwar R. Padhani²

¹ Siemens Healthineers, Erlangen, Germany

² Paul Strickland Scanner Centre, Mount Vernon Hospital, Northwood, Middlesex, UK

Whole-body MRI with diffusion imaging has gained a lot of attention as a promising technique for the assessment of multifocal bone disease, such as multiple myeloma and bone metastases from breast and prostate cancer [1–3]. Diffusion-weighted MRI in combination with other MRI contrasts has a high sensitivity and specificity for disease

detection [4], without exposing patients to ionizing radiation. However, one challenge is the relatively large effort in image interpretation, due to the number of images that are generated, and the lack of available tools for efficient evaluation.

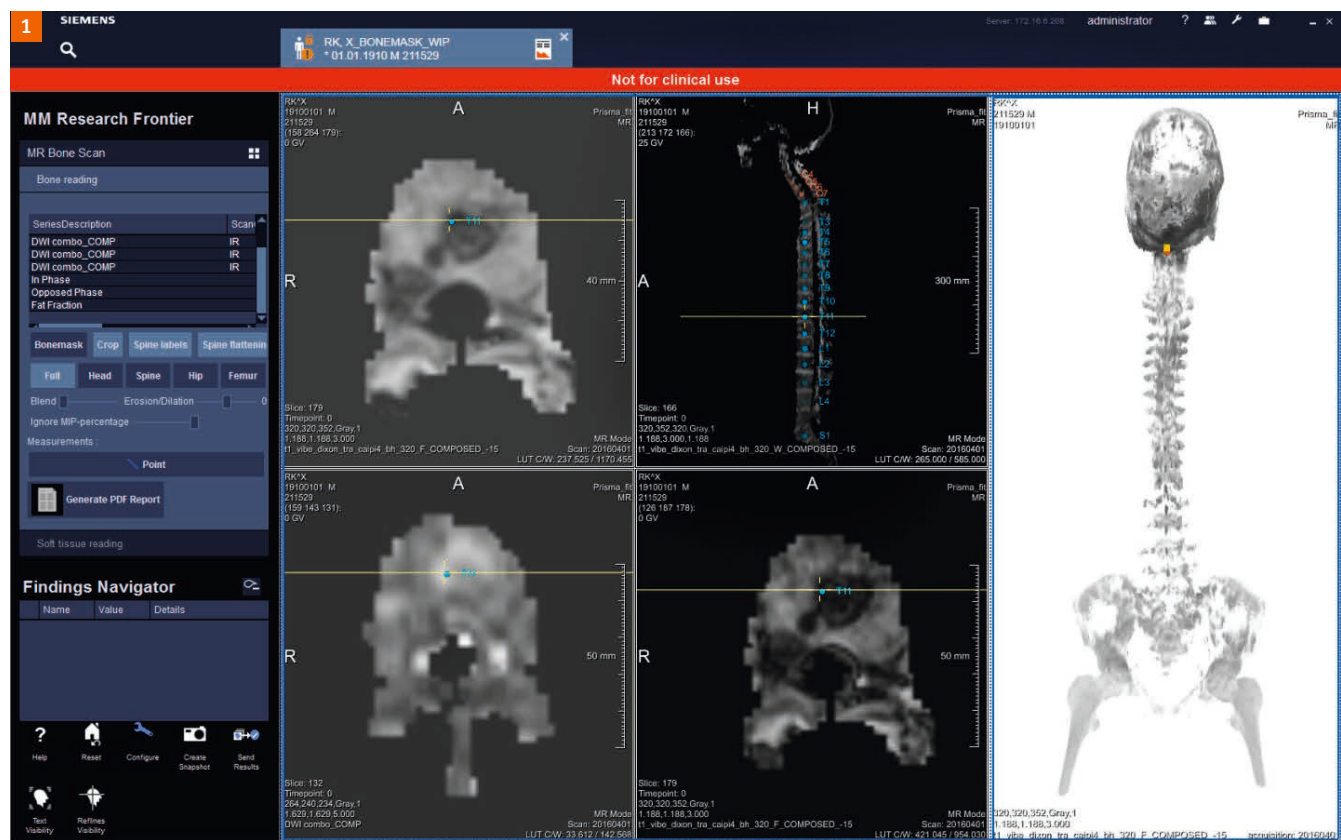


Figure 1: The figure shows a snapshot of the bone reading step of the application with the cropping and the spine unrolling/flattening and spine labeling features activated. The cursor is centered at the T11 vertebral body.

Siemens has implemented a novel MR whole-body image reading prototype with a specific focus on metastatic bone disease. The vision behind this *syngo.via* Frontier MR Bone Scan¹ is to leverage MR and MR-PET bone reading and make it as efficient as in the *syngo*.CT Bone Reading application. As a central feature, the application computes segmentations of the axial skeleton based on Dixon input images, using an atlas based algorithm [5].

The bone segmentations can be used in several ways:

- 1) Bone segmentations can be applied to remove all other tissues on any given image contrast, thus directing the reader's attention directly to the bone and the bone marrow. When this is done with high b-value images, rotating maximum intensity projections (MIPs) can be generated that provided a focused overview of the state of the disease in the skeleton. This enables assessments of abnormalities within the bones at a single glance. The ability to automatically remove soft tissues and other extraneous signals increases metastatic conspicuity on inverted MIPs on the segmented volume. This is of advantage in metastatic prostate cancer where lesion conspicuity may be obscured by surrounding tissue signal.

The ability to isolate bones on multiple, registered image sequences such as DWI, ADC maps, in- and opposed phase Dixon, Fat Fraction and T1- and T2-weighted images with combined MIP images, enables focused, efficient multiparametric evaluations of the bones without signals and artefacts from surrounding soft tissues.

- 2) Bone segmentations can help to support visualizations like unrolling bones into a plane to simplify the geometric complexity for complete and easy assessment with few scroll moves through a reduced number of slices. In particular, the *syngo.via* Frontier MR Bone Scan allows for projecting the spine to a plane, displaying all vertebra at a single glance as a straightened flattened spine. All other image contrasts can also be warped accordingly in the unrolled spine mode.
- 3) Bone segmentations provide useful additional anatomic orientations, which helps to facilitate reporting. The vertebra of the segmented spine can be labelled, with labels presented to the user as overlays.
- 4) Bone segmentations from DWI independent image contrasts could support unbiased, quantitative multiparametric evaluation of the bone marrow also. Co-registered bone segmentations of image contrasts

such as fat fraction, ADC, high b-value signals can enable the separation of normal yellow marrow, mixed marrow, viable tumor regions, microscopic necrosis, macroscopic necrosis voxels. Co-registered voxels can be evaluated in *syngo.via* Frontier Total Tumor Load and Scatter Plot software for these purposes.

- 5) In addition, separate evaluations of the different bones are supported. For instance, the pelvic bone and its voxels can be isolated and evaluated. Quantitative values could be evaluated independently thus enabling therapy response assessment and evaluation of spatial heterogeneity if required.

syngo.via Frontier MR Bone Scan supports standard tools for reading and reporting such as automatic configuration of hangings, automatic scrolling and synching of the segments as well as measurement tools.

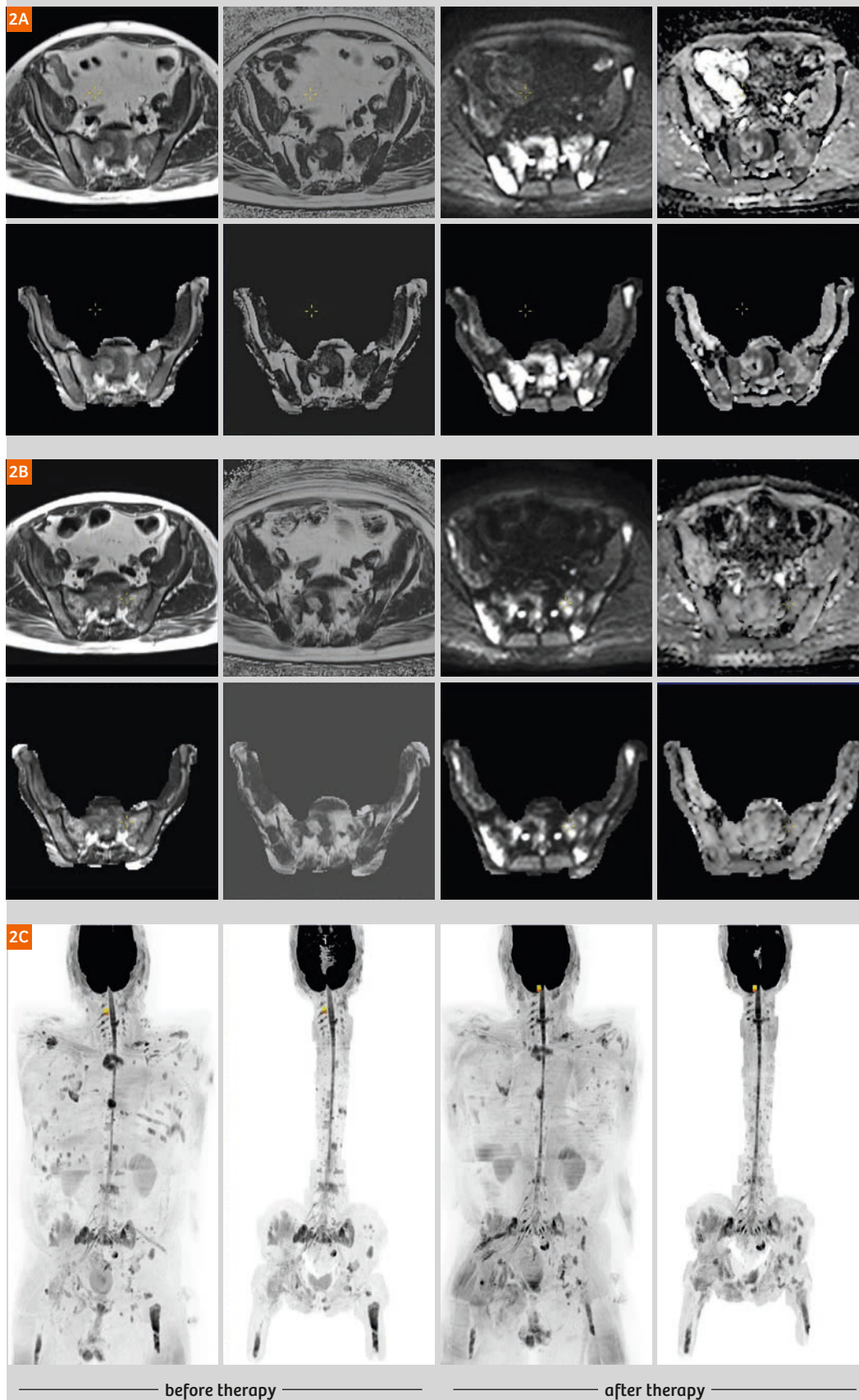
The workflow of the application is structured into two steps.

- 1) Bone reading step: Layout, hangings and tool configuration are set up for the assessment of bone metastases. The bone segmentation runs in the background and yields the bone mask that allows for the usage of the advanced visualization tools mentioned above to support the reading process.
- 2) Soft tissue reading: Layout, hangings and tool configuration are set up to assess the status of soft tissues including primary tumors, lymph node and visceral organs.
- 3) In a final step, results and findings can be exported in a report pdf sheet.
- 4) The computed bone mask can be stored back to the patient image database and be made available for secondary (quantitative) evaluation tools like *syngo.via* Frontier Total Tumor Load as an independent bone mask.

Figure 1 shows a snapshot of *syngo.via* Frontier MR Bone Scan.

The clinical case in Figure 2 shows a 70-year-old man with castrate resistant prostate cancer who has failed hormonal therapy and docetaxel chemotherapy, and is now undergoing a novel therapy that targets the prostate specific membrane antigen (PSMA) receptor. Pre- and post-therapy assessments were undertaken on a 3T MAGNETOM Prisma scanner. Note that assessments of the bone status on the whole-body inverted b800 MIP images is impaired due to signals from soft tissues, including the swollen right leg (new hip fracture on the post therapy), kidneys and bowel on both studies. After automated cropping and removal of the soft tissue signals, the response of the disease becomes easier to evaluate.

¹ *syngo.via* Frontier is for research only, not a medical device.



In summary, *syngo.via* Frontier MR Bone Scan is a promising application for whole-body reading enabling unbiased qualitative and quantitative assessments of bone marrow and bone lesions, with potential applications in therapy monitoring. However, it should be noted that it is still an evolving application, requiring optimizing the reading workflow for therapy response assessment in metastatic bone disease. Future developments will include layouts and tools for parallel evaluation of several time points. It is also planned to include features for direct quantitative evaluation as described in the Total Tumor Load (see article by Grimm and Padhani in this issues of MAGNETOM Flash) and seamless interactions with other *syngo.via* Frontier oncology prototypes.

References

- 1 Pawlyn C, Fowkes L, Otero S, et al. Whole-body diffusion-weighted MRI: a new gold standard for assessing disease burden in patients with multiple myeloma? Leukemia. 2016;30(6):1446-1448. doi:10.1038/leu.2015.338.
- 2 Padhani AR, Lecouvet FE, Tunariu N, Koh DM, De Keyser F, et al. (2016) Rationale for Modernising Imaging in Advanced Prostate Cancer. European Urology Focus, Available online. doi:10.1016/j.euf.2016.06.018.
- 3 Padhani AR and Tunariu N, Metastatic response system in using whole body MRI for prostate cancer in practice – also in this issue of MAGNETOM Flash.
- 4 Li B, Li Q, Nie W, Liu S. Diagnostic value of whole-body diffusion-weighted magnetic resonance imaging for detection of primary and metastatic malignancies: a meta-analysis. European Journal of Radiology 2014; 83(2): 338-344.
- 5 Paulus DH, Quick HH, Geppert C, Fenchel M, Zhan Y, Hermosillo G, Faul D, Boada F, Friedman KP, Koesters T. Whole-Body PET/MR Imaging: Quantitative Evaluation of a Novel Model-Based MR Attenuation Correction Method Including Bone. J Nucl Med. 2015 Jul;56(7):1061-6.

Contact




Matthias Fenchel, Ph.D.
Siemens Healthcare GmbH
HC DI MR PI TIO ONCO

Postbox 32 60
91050 Erlangen
Germany
Phone: +49 (0) 9131 84-2113
matthias.fenchel@siemens.com

Watch Cancer Develop Multidrug Resistance

In this video Professor Padhani shows how quantitative whole-body MRI is used to monitor therapy response in metastatic breast cancer. Watch the video at

www.siemens.com/magnetom-world



Watching cancer develop multidrug resistance

Quantitative whole-body MRI to monitor therapy response in metastatic breast cancer

Professor Anwar R. Padhani, MB, BS, FRCP, FRCR
Paul Strickland Scanner Centre, Mount Vernon Hospital, Northwood, Middlesex, UK

ADC classes and cellular states
Cellular tumor, microscopic cell death, macroscopic necrosis

MR Total Tumor Load 12.8

Cellular tissue: 72%
Microscopic cell death: 95 centile of baseline study
Macroscopic necrosis: 1500 $\mu\text{m}^2/\text{s}$

Response Sept 2012 Visceral disease: Liver

1st line Rx

2012 2013 2014 2015 2016

Therapy	2012	2013	2014	2015	2016
Herceptin Rx	Trastuzumab	Trastuzumab, Herceptin	Trastuzumab	Trastuzumab-embolic	Trastuzumab
ER Rx / Endocrine Rx	Endocrine therapy	Endocrine therapy	Endocrine therapy	Endocrine therapy	Endocrine therapy
Anti bone resorption	Denosumab	Denosumab	Denosumab	Denosumab	Denosumab

Magnet Homogeneity and Shimming

Mathias Blasche, MS; Daniel Fischer, BS, BA, MBA

Siemens Healthineers, Erlangen, Germany

Magnet criteria

The magnet is the most prominent – and most expensive – part of an MRI system. It creates the main magnetic field, B_0 , which serves as the basis for all magnetic resonance imaging.

There are several features and specifications of the magnet design that have an influence on different criteria:

Image quality

- Magnetic field strength B_0
- Magnet homogeneity and maximum field of view
- Shimming capabilities

Patient comfort

- Magnet warm bore and bore diameter (including gradient coil, body coil and covers)
- Magnet length and total system length (including covers)
- Magnet height/width and outer dimensions (including covers)

Economic aspects

- Helium boil-off (Zero Helium boil-off for state-of-the-art systems)
- Stray field, reduced with active shielding, to reduce space requirements
- Magnet and system weight, for siting

In this article, the aspects of magnet homogeneity, shimming capabilities, and their respective relevance for MRI will be addressed.

Particular care will be taken to reduce confusion in the interpretation of the effects and benefits of the homogeneity of an empty magnet (installation shim) versus the effects and benefits of patient-specific (active) shimming. We will have a deeper look into the clinical benefits of linear and high-order shimming capabilities as well as new patient-specific shim technologies.

1

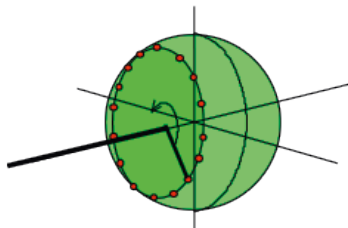


Figure 1: Measurement of magnetic field strength on multiple angles in several planes for assessment of magnetic-field homogeneity.

Relevance and definition of magnetic-field homogeneity

For magnetic resonance to work, a high homogeneity of the magnetic field is imperative. Within the imaging volume, the magnetic field has to be very accurate, with minimal deviations of the magnetic field allowed.

Magnetic-field homogeneity is commonly measured in ppm (parts per million) difference from the B_0 field. For example, if a 1.5-Tesla system has a deviation of, say, 2 ppm (peak to peak) at a particular location, the field strength at this location deviates by $(1.5 \text{ T} \times 2 \times 10^{-6} = 3 \text{ } \mu\text{T})$.

There are different specification methods for homogeneity, the most important ones being:

• Peak-to-peak homogeneity

This is a measure of the maximum deviation within an imaging volume, i.e. the deviation between just the two 'worst-case' points on the surface of that particular volume.

• Volume-root-mean-square (VRMS) homogeneity

VRMS provides an 'integral' specification within the whole imaging volume. It is the industry-wide standard of homogeneity specification for the 'empty magnet' as specified in the data sheets. This will be further discussed in the next chapter, Installation shim.

Installation shim

Despite high efforts in the manufacturing process, a new magnet leaving the factory will typically have a magnetic-field inhomogeneity in the range of ~ 500 ppm (peak-peak) over the maximum volume. The conditions on site (e.g., steel reinforcements in the building structure) will also negatively influence the magnetic field homogeneity. The field homogeneity has to be refined during the system installation. This process is called shimming.

First, the magnetic field is measured at the installation site with the help of a tool to accurately measure the magnetic field. The so-called shimming device is positioned exactly at the iso-center of the magnet. The magnetic field is measured at multiple angles in several planes, see Figure 1.

All superconducting MAGNETOM systems use an accurate 24-plane plot with 20 angles each for the measurement of the magnetic-field homogeneity. Due to the cylindrical symmetry of the magnet, the total number of angles is less critical to the measurement. However, the number of planes can make a big difference in the accuracy of the homogeneity

measurement. Most magnets feature 6 superconducting field-generating coils. In such a 6-coil magnet, especially a 12-plane plot will be highly inaccurate since a 12-plane plot measures the magnetic field on 'equivalent zero-crossing' locations, thus artificially 'improving' magnet homogeneity specifications. A 24-plane plot, on the other hand, 'sees' all maxima and minima of the magnetic field and therefore provides more accurate information about the magnet homogeneity.

After the measurement, the measured values are entered into a computer program and the field homogeneity corrections are calculated. In order to perform a magnet shim, there are a number of options available:

- **Passive shim**

Shim irons of defined weight and shape are placed at exact positions, all calculated by the computer program. The shim irons are placed in dedicated shim pockets, typically situated in the gradient coil.

Passive shimming has a very high number of degrees of freedom (multiple shim irons of different weights at multiple positions). It is therefore very accurate and can correct shim terms up to ~ 24th order.

- **Superconducting shim**

This is a method used by one vendor. Additional superconducting shim coils are positioned in the magnet and can, based on the results of the field measurement and the results of the computer program (see above), be used for the improvement of the homogeneity of the (empty) magnet during installation.

The superconducting shim has the advantage of lower inserted iron mass in the magnet/gradient coil, i.e. there is no temperature dependence of the magnetic effect of the iron pieces.

However, the superconducting shim coils offer much fewer degrees of freedom. For instance, with 18 superconducting shim coils, only shim terms up to ~ 4th order can be corrected.

Note that the superconducting shim is only used for the shimming of the 'empty magnet', i.e. the installation shim.

It cannot be changed dynamically and cannot be used for patient-specific shimming. Also, superconducting shims decay over time and need regular re-adjustments. If something goes wrong with the magnet internal switching, that shim term is lost permanently.

- **Active shim**

For fine-tuning the field homogeneity, an active shim can also be performed. The same linear (and, if available) higher-order shim terms can be used as for the patient-specific shimming (see next chapter).

However, this is of less importance for the installation shim. The active shim only affects 1st-order (max. 2nd-order) shim terms, while the passive shim, described above, can affect terms of much higher order. The active shim is mainly used for the correction of patient-induced inhomogeneities (see below).

The measurement of the magnetic-field homogeneity and the homogeneity corrections by the methods described above are performed iteratively. Typically, 2–3 iterations are sufficient to achieve the homogeneity values that are specified in the data sheet.

Figure 2 shows an example of the homogeneity specifications of an 'empty magnet' after installation of the system, achieved with passive shimming and 1st-order active shimming, as described above.

The homogeneity of the 'empty magnet' can also be understood as the theoretical limit of the magnet homogeneity in clinical operation. In particular, it defines an upper limit for the maximum field of view (FOV) that can be used in clinical operation.

Different sequences show different levels of sensitivity to magnetic-field inhomogeneities. 'Insensitive' sequences (e.g. Turbo Spin Echo) will still achieve acceptable imaging results with inhomogeneities in the range of ~ 50 ppm (peak-peak). Spectral fat saturation, on the other hand, will only work with inhomogeneities up to ~ 2 ppm (peak-peak), since the chemical shift between fat and water is 3.5 ppm. Note that the data sheet specifications in Figure 2 are VRMS values, peak-to-peak values over the same volumes will be much higher.

Shape of the homogeneous magnetic field

The 'natural' shape of the homogeneous field of a solenoid magnet, as used in all 'bore-type' magnets, is spherical or ellipsoid. The ellipsoid is typically shorter in z-direction than in x/y-directions since the z-direction is the more critical one in bore-type magnets. A large homogeneity in z-direction is

DSV	Guaranteed	Typical
50 cm	< 1.5 ppm	0.8 ppm
45 cm	< 1 ppm	0.4 ppm
40 cm	< 0.75 ppm	0.2 ppm
30 cm	< 0.5 ppm	0.1 ppm
20 cm	< 0.25 ppm	0.04 ppm
10 cm	< 0.05 ppm	0.01 ppm
DSV – Diameter spherical volume (x, y, and z direction)	Standard deviation VRMS (volume root-mean-square) measured with highly accurate 24-plane plot method (20 points per plane) standard active shim with 3 linear channels	

Figure 2: Example for the specification of the 'installation shim' with VRMS homogeneity specifications over spherical volumes with 10–50 cm diameter. Screenshot from the data sheet for the MAGNETOM Avanto 1.5T system.

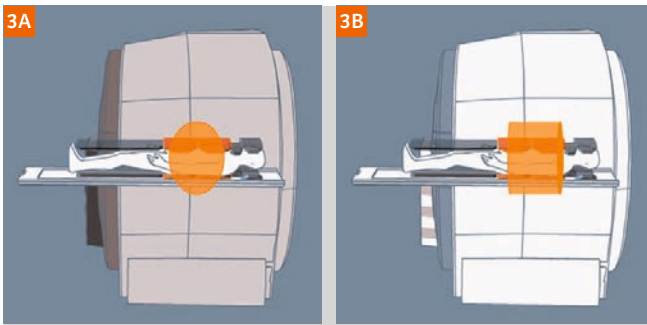


Figure 3: Visualization of the imaging volumes of a conventional magnet with spherical/ellipsoid volume (3A) vs. TrueForm Magnet Design with a cylindrical volume (3B).

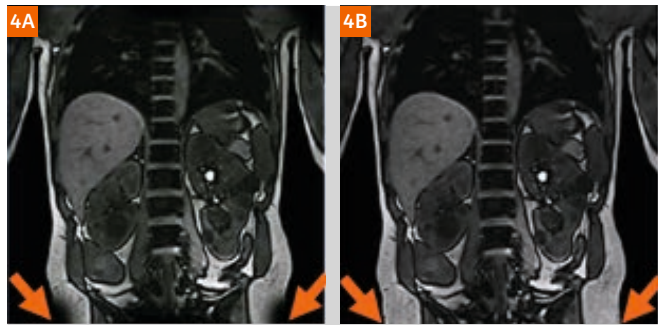


Figure 4: Visualization of the better depiction of the edges in large-FOV coronal images with TrueForm Magnet Design (4B) vs. conventional (4A).

facilitated by a larger magnet length. However, a longer magnet would compromise patient comfort. This needs to be considered in the design phase.

Some MAGNETOM systems (MAGNETOM Aera, Amira, Sempra, Skyra, Spectra, Verio) feature TrueForm Magnet Design. They are optimized for a cylindrical shape of the homo-geneous volume of the magnetic field, rather than the typical spherical or ellipsoid volume. The benefit of TrueForm Magnet Design is a better depiction of the edges of the (3-dimensional) FOV. This is in particular beneficial for large-FOV coronal imaging, for multi-step examinations with extended FOV, and for TimCT. A visualization of TrueForm Magnet Design is shown in Figures 3 and 4.

Patient-specific shim

The homogeneity of the 'empty' magnet, as specified in the data sheet, will be strongly affected once a patient is positioned in the bore. This effect can result in several ppm of field inhomogeneity. This effect can easily be seen when forgetting to perform a patient-specific shim procedure that uses spectral fat saturation. The reason for this failure: fat saturation, being sensitive to peak-to-peak variations in the order of 2 ppm, will fail as a result of the greater inhomogeneity.

In many applications, the effect of the patient-specific shimming will be much more important than the homogeneity of the empty magnet. In particular, the homogeneity specifications of the magnet for small volumes with specifications much smaller than 1 ppm (compare Figure 2) will be irrelevant when compared to the inhomogeneity introduced by the patient. The capabilities that the MRI system offers for patient-specific shimming are critical in these applications.

Applications that are especially sensitive to magnetic-field inhomogeneities – and benefit most from patient-specific shimming – include:

- Spectral fat saturation and water excitation because they depend on the chemical shift between fat and

water of 3.5 ppm. A magnetic-field homogeneity better than ~ 2 ppm (peak-to-peak) is important.

- In general, all sequences that are sensitive to susceptibility effects, e.g. gradient echo with long echo times, TurboGSE, sequences using phase information like phase contrast angiography, SWI, etc.
- In particular, Echo Planar Imaging (EPI) methods, as used for diffusion, perfusion and fMRI, since the EPI echo train can be up to 100 ms long and is affected by the (rather short) T2* relaxation times. Higher magnet homogeneity will increase T2* values.
- TrueFISP sequence because TrueFISP basically consists of an S+ and an S- echo that need to be simultaneous. Magnetic-field inhomogeneities will destroy the synchronicity of S+ and S-, resulting in banding artifacts in the image.
- MR Spectroscopy (especially CSI with large volume of interest) because the chemical shifts of different metabolites in the sub-ppm range need to be resolved. Magnetic-field homogeneity needs to be better than the chemical shift between the metabolites.
- 3 Tesla: magnetic-field homogeneity is especially important for 3T MRI since the higher field strength increases susceptibility artifacts. Therefore, practically all state-of-the-art 3T scanners on the market (with a few exceptions) have a high-order active shim as standard.

As said, in many applications, the patient-specific shim capabilities will be more important than the homogeneity of the empty magnet. The performance of the patient-specific shim depends on two factors:

- Hardware: Dedicated shim coils for patient-specific shimming, for the shimming of linear terms and (if available) higher-order terms.
- Software: Shim algorithms for the measurement and correction of magnetic-field inhomogeneities, making use of the available hardware.

These are covered in the next chapters.

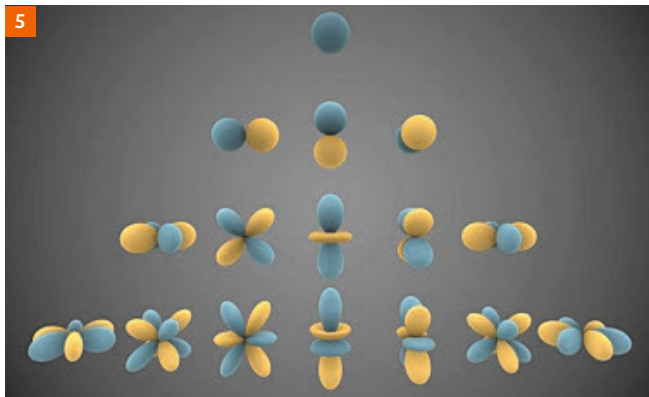


Figure 5: Visual representations of the real spherical harmonics up to 3rd-order. Blue portions represent regions where the function is positive, and yellow portions represent where it is negative. (Source: Wikipedia, http://en.wikipedia.org/wiki/Spherical_harmonics)

Hardware

Linear and higher-order shim terms

The magnetic field is commonly described in the so-called 'spherical harmonics'. The concept of the spherical harmonics is explained e.g. on Wikipedia (http://en.wikipedia.org/wiki/Spherical_harmonics).

The series of harmonics is:

1 0th-order term + 3 1st-order terms + 5 2nd-order terms + 7 3rd-order terms + ...

So, what do these terms mean? A graphical visualization can be found in Figure 5.

- The 0th-order term is nothing else than the static magnetic field B_0 .
- The 1st-order terms are linear deviations from the homogeneous B_0 field. There are 3 linear terms, describing the linear deviations in x, y, and z directions. This is exactly the same shape as is also produced by the 3 axes of the gradient system. The gradient system is there anyway, no additional hardware is required: In all MR systems on the market, the standard gradient system is used for shimming of the linear (= 1st-order) terms.
- The 2nd-order terms are quadratic deviations from the B_0 field. There are 5 2nd-order terms, namely z^2 , xz , yz , xy , x^2-y^2 . Special 2nd-order shim coils are required to correct for 2nd-order field inhomogeneities. Also, 5 additional power supplies and a software implementation are required. A 2nd-order shim set (often called high-order shim or advanced shim) is available for some 1.5T systems in the market. It is standard with most 3T systems.
- 3rd-order shim terms (and higher) are currently not available in the market for MR systems with field strengths up to 3 Tesla.

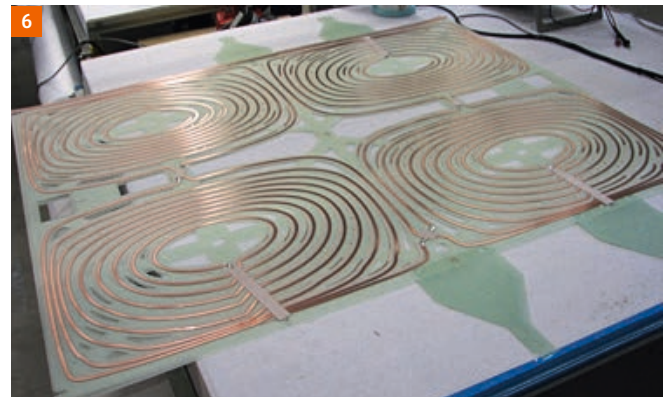


Figure 6: Design of a 2nd-order shim coil. This is wound around (and integrated into) the gradient coil. Shown is the example of the x^2-y^2 coil (same design as xy coil).

Integrated coil shim

A new method to improve the local magnet homogeneity even more, beyond the possibilities using 1st- and 2nd-order shimming, was recently introduced with the MAGNETOM Vida¹. CoilShim, a central feature of BioMatrix technology, offers up to four additional independent shim channels that can be used to power and control local shim coils.

The head/neck region is especially critical regarding magnetic-field inhomogeneities. The shape of the human body – the curvature of the posterior neck, the chin region, the lateral extension of the shoulders, and the susceptibility changes due to the trachea and the esophagus – induces severe inhomogeneities for neck and plexus imaging. Even a (global) 2nd-order shim is not sufficient to correct these inhomogeneities in many cases.

To improve the homogeneity in this critical region, the MAGNETOM Vida features a new Head/Neck 20 coil and a new Head/Neck 64 coil. Both coils have two additional dedicated shim coils built into the coil. The shim coils are very close to the critical anatomy, and their design is optimized to address the specific inhomogeneities in this region. The calculation and fine-tuning of the local CoilShim currents are fully integrated into the shim algorithm.

Software

Shim algorithms

For patient-specific shimming, first the field inhomogeneities need to be measured. The result can be visualized in a so-called B_0 map. It is not possible to measure the field homogeneity with special hardware devices while the patient is in the magnet, for various reasons: First, a costly device would be required; second, the setup of such a device would be time-consuming, compromising workflow and throughput; third (and foremost), the patient is just in the way. Therefore, MR-based phase-sensitive scans are used to gain knowledge about magnetic-field inhomogeneities.

There are different approaches to what is actually being measured. The standard procedure is a 'global' measurement of the whole imaging volume of the scanner. If this is done with a 3D scan, one measures spatially resolved information about the magnetic field. For later imaging scans (at the same table position), only the relevant sub-volumes can be taken into account. These sub-volumes can be identical to the imaging volume, i.e. the volume covered by the 2D slice stack or 3D imaging slab. Alternatively, it can be useful to define the shim volume manually, e.g., only selecting a smaller sub-volume which is most critical.

After the shim measurement has been performed, an algorithm will calculate the optimal shim currents for improving the magnetic-field homogeneity, based on the shim volume selected. The algorithm will make use of the available shim hardware by using gradient offset currents for the linear correction terms and – if available – additional higher-order shim currents for the 2nd-order terms.

All of this – the homogeneity measurement and the calculation of the shim currents – is done fully automated in routine clinical applications. The user will only notice a short delay before the actual imaging scan, typically a few seconds. For special applications (like spectroscopy) and for research use, it is also possible to perform an additional manual shim by changing the shim currents directly in the user interface.

Slice-specific shimming

A global shim, as discussed in the last chapter, can only address an 'average' of the homogeneity improvement over a large imaging volume. Even a patient-specific 2nd-order shim may be insufficient to optimize the magnet homogeneity in all parts of this large volume.

As another new BioMatrix feature of the MAGNETOM Vida, SliceAdjust offers a precise slice-by-slice tuning of resonance frequency, transmitter voltage, first order B_0 shim and B_1 shim. For whole-body diffusion, the SliceAdjust technology helps to avoid station boundaries and apparent 'broken spine' artifacts as well as to preserve the SNR for whole-body diffusion imaging.

Clinical comparison

2nd-order shimming vs. linear shimming

The following images show a comparison between shimming with the 1st-order shim terms only (2nd-order shim was disabled) and shimming using 1st-order and 2nd-order shim terms.

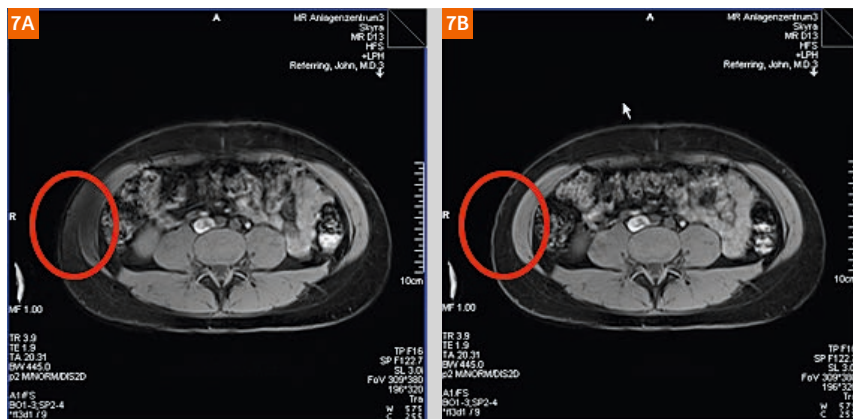


Figure 7: Abdominal imaging with spectral fat saturation, MAGNETOM Skyra 3T.

(7A) With 1st-order shim only (2nd-order shim disabled).

(7B) With 1st-order and 2nd-order shim.

Note the superior fat saturation in the off-center region when using 2nd-order shimming (red circle).

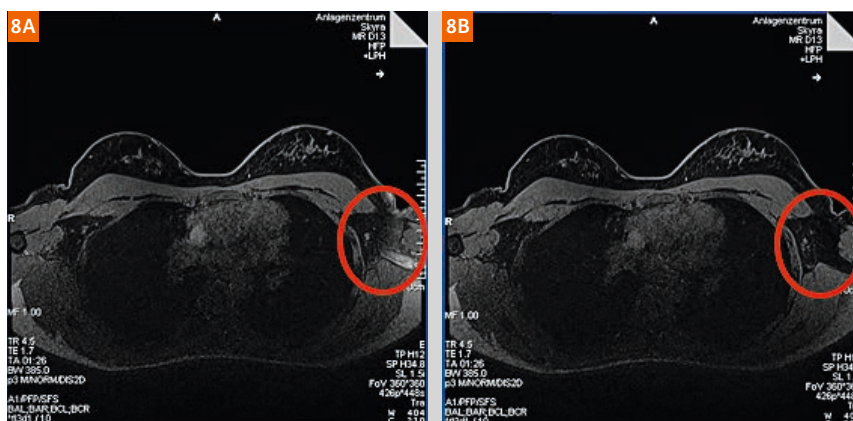


Figure 8: Breast imaging with spectral fat saturation, MAGNETOM Skyra 3T.

(8A) With 1st-order shim only (2nd-order shim disabled).

(8B) With 1st-order and 2nd-order shim.

Note the superior fat saturation in the off-center region when using 2nd-order shimming (red circle).

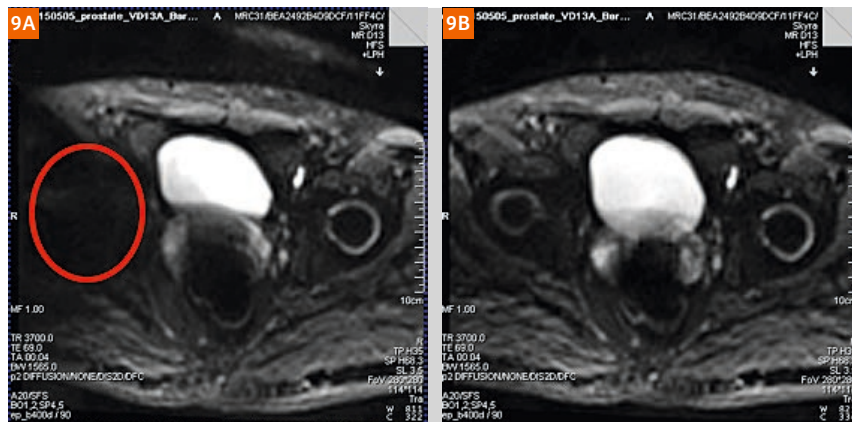


Figure 9: Pelvic imaging with with diffusion-weighted single-shot EPI and spectral fat saturation, MAGNETOM Skyra 3T. (9A) With 1st-order shim only (2nd-order shim disabled). (9B) With 1st-order and 2nd-order shim.

Note the strong spatial distortions (red circle) in the presence of strong susceptibility changes without 2nd-order shimming.

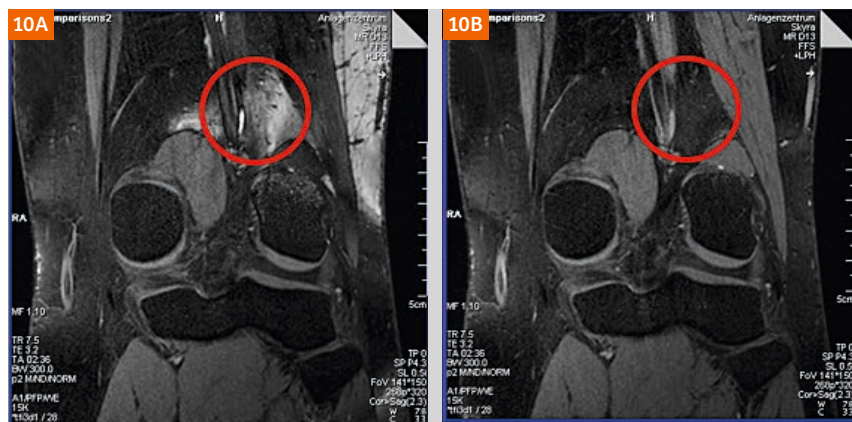


Figure 10: Knee imaging with spectral fat saturation in off-center position, MAGNETOM Skyra 3T. (10A) With 1st-order shim only (2nd-order shim disabled). (10B) With 1st-order and 2nd-order shim.

Note the superior fat saturation when using 2nd-order shimming (red circle).

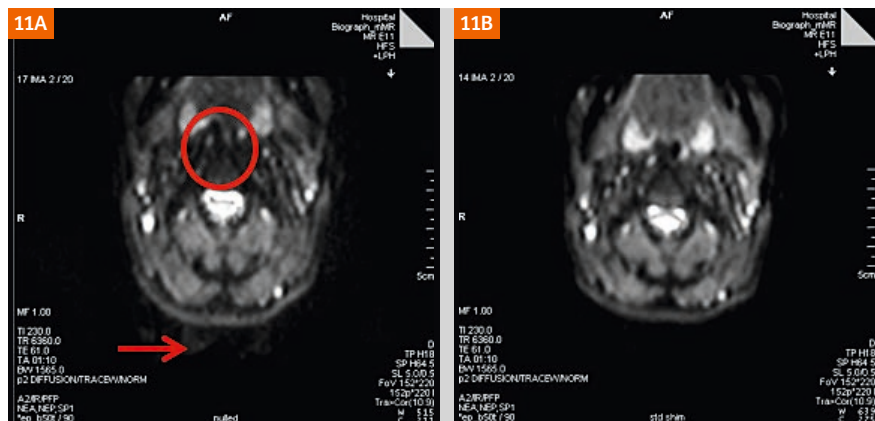


Figure 11: Neck imaging with diffusion-weighted single-shot EPI and spectral fat saturation, Biograph mMR 3T. (11A) With 1st-order shim only (2nd-order shim disabled). (11B) With 1st-order and 2nd-order shim. The neck area is especially critical, due to B_0 inhomogeneities at the head-shoulder transition and due to strong susceptibility changes in the neck. Note the higher level of spatial distortions (red circle) and the stronger appearance of ghosting artifacts (red arrow) without 2nd-order shimming.

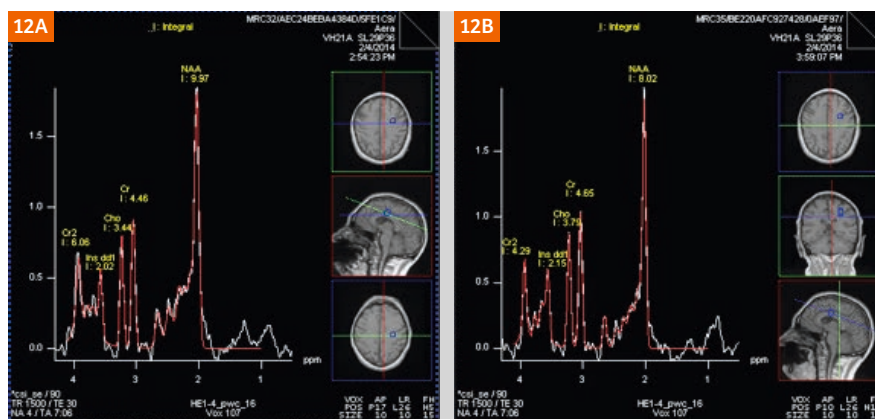


Figure 12: CSI spectroscopy in the brain, MAGNETOM Aera 1.5T. (12A) With 1st-order shim only (2nd-order shim disabled). (12B) With 1st-order and 2nd-order shim. The region in the center of the brain does not suffer from susceptibility effects. The quality of both spectra is similar, i.e. 1st-order shimming is in this 'easy' case sufficient.

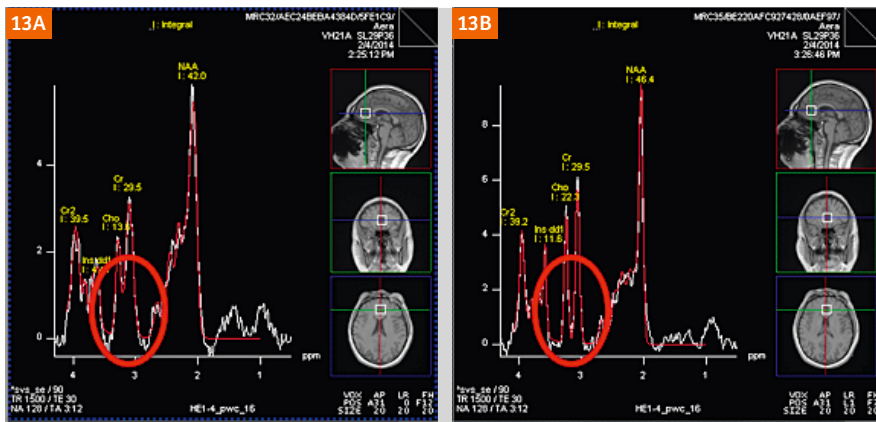


Figure 13: Single-voxel spectroscopy in the brain, MAGNETOM Aera 1.5T. (13A) With 1st-order shim only (2nd-order shim disabled). (13B) With 1st-order and 2nd-order shim. The frontal lobe, close to the nasal cavities, is a critical region, due to strong susceptibility effects. The spectrum without 2nd-order shim can not be evaluated (red circle). Also note the different scaling of the spectra.

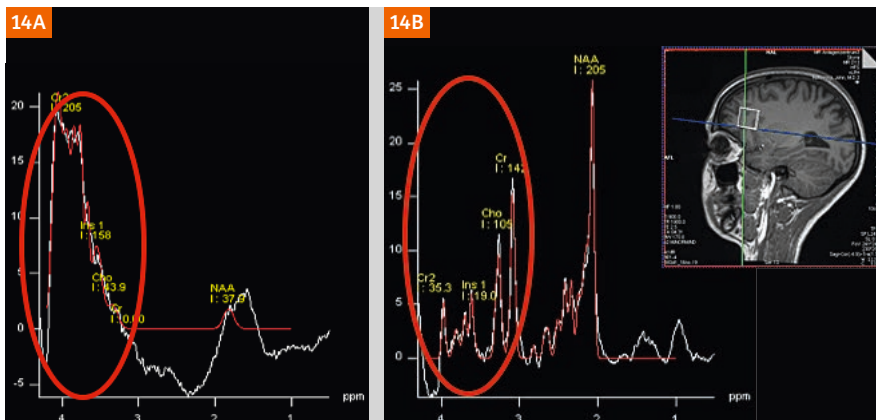


Figure 14: Single-voxel spectroscopy in the brain, MAGNETOM Skyra 3T. (14A) With 1st-order shim only (2nd-order shim disabled). (14B) With 1st-order and 2nd-order shim. At 3T, the susceptibility effects in the frontal lobe are even more severe. The spectrum without 2nd-order shim can not be evaluated (red oval).

Integrated coil shim vs. conventional global shim

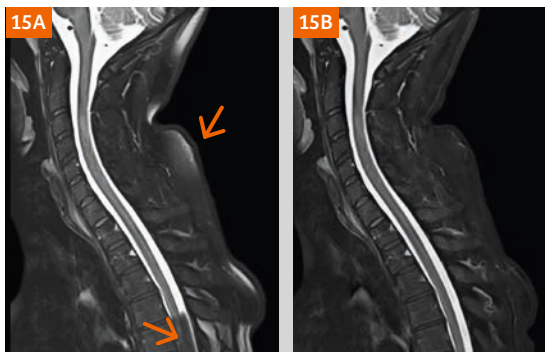


Figure 15: C-spine imaging with fat suppression, MAGNETOM Vida 3T. (15A) With conventional global shim. (15B) With CoilShim. CoilShim improves the local magnet homogeneity in the critical neck region, resulting in an artifact-free depiction of the spinal cord and perfect fat suppression in the posterior neck region (see orange arrows).

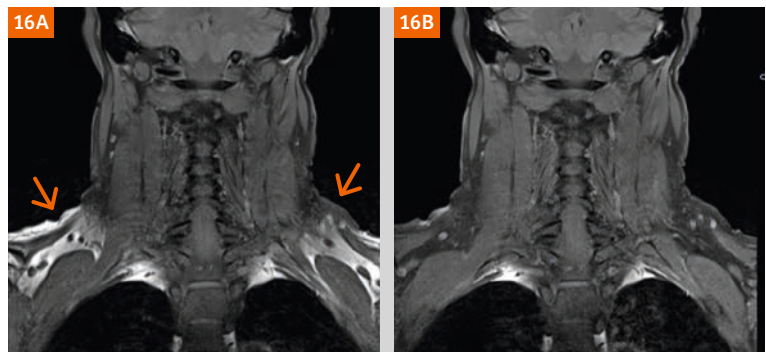
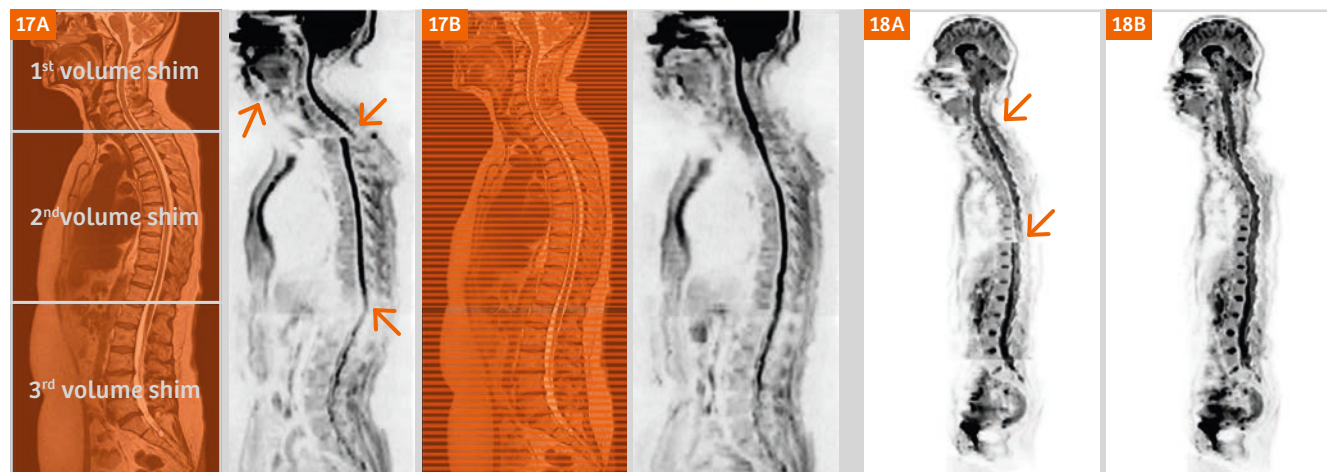


Figure 16: Neck imaging with fat suppression, MAGNETOM Vida 3T. (16A) With conventional global shim. (16B) With CoilShim. CoilShim improves the local magnet homogeneity in the critical neck region, resulting in perfect fat suppression in the neck/shoulder region (see orange arrows).

Slice-specific shimming vs. conventional global shim



Figures 17 and 18: Whole-spine imaging with diffusion weighting, reconstruction from axially acquired slices. MAGNETOM Vida 3T. The 'average' global shim over a large FOV significantly changes between different steps, resulting in 'broken spine' artifacts (orange arrows). The 'continuous' slice-by-slice shim with SliceAdjust guarantees a smooth transition of the shim states and prevents 'broken spine' artifacts.

(17A, 18A) With conventional global shim, acquired in three steps with three shim regions.

(17B, 18B) With SliceAdjust¹, different optimized shim setting for each slice.

Conclusion

The magnet of an MRI scanner is an important component. It has implication on image quality, patient comfort, and economic aspects. The design of the magnet has to be balanced, addressing all these aspects (which are partly contradictory, e.g. magnet homogeneity vs. magnet length).

In this paper, we focused on the aspects of magnet homogeneity and shimming capabilities.

Different criteria of magnet homogeneity should not be confused. The homogeneity of the empty magnet (installation shim) is mainly important for the maximum field of view. Most clinical applications rather depend on the capabilities of the system to perform patient-specific shimming. The homogeneity specification of the magnet for small volumes is rather irrelevant compared to the inhomogeneities induced by the patient.

1st-order shimming alone (by means of the gradient system) is sufficient for many applications. However, for more critical applications and in critical regions, 2nd-order shimming capabilities can play a crucial role for optimal image quality, consistently. The relevance of 2nd-order shimming capabilities depends on the clinical usage of the system.

The new BioMatrix technologies¹, CoilShim and SliceAdjust, allow to improve the local field homogeneity even more, beyond the capabilities of global 1st- and 2nd-order shimming.

¹ 510(k) pending. The product is not commercially available. Future availability cannot be guaranteed.

Contact



Mathias Blasche
Siemens Healthcare GmbH
Karl-Schall-Str. 6
91052 Erlangen
Germany
mathias.blasche@siemens-healthineers.com

Meet Siemens Healthineers

Our brand name Siemens Healthineers embodies our pioneering spirit and engineering expertise in the healthcare industry. The people working for Siemens Healthineers are highly passionate about the technology and the company they work for and their engineering capabilities and pioneering spirit are unique in this industry. In this section we introduce colleagues from all over the world to you – people who put their hearts into what they do.



Stockholm, Sweden

Lars Filipsson graduated in physics from the Royal Institute of Technology, KTH University, Stockholm, Sweden and then spent 8 years at the Karolinska Institutet as Research Engineer with responsibility for the Electron Microscopy Section. There he assisted and supported doctors in various research projects with knowledge and the development of new techniques and applications within Electron Microscopy. He undertook research of his own in the field of transport mechanisms of proteins through cell membranes – “inverted micelles” – using low-temperature preparation techniques. He describes one step, that involved verification of the phase shift by using NMR spectroscopy as his first real contact with “this magical phenomenon”.

In 1985 Lars moved to Siemens as Product Manager MR. Over the years he has worked in different positions as Business Manager/Marketing Manager for CT, Angiography, Ultrasound, PACS, Nuclear Medicine, and Radiation Therapy. In 2007 he joined the Particle Therapy group in Erlangen, moved to Nuremberg, and worked with the Siemens solution for treatment with protons and carbon ions.

Since returning to Sweden he has been working mostly within MR and Radiation Oncology.

How did you first come in contact with MRI?

After being impressed by NMR spectroscopy my first contact with MRI was when the first MRI system in Scandinavia was installed in Uppsala in 1984 and I started my career at Siemens. At that time the field strength was 0.35T, the system was huge and it was really amazing that it was possible to create images out of such a machine.

What is most fascinating about MRI?

It has been a fantastic journey over time to see how MRI has developed. Applications that were considered almost impossible some years ago are now in clinical use. One conclusion is clear: With MRI you should never say never. Everything seems to be possible.

What is your role in the Swedish project to promote the use of MR in Radiation Therapy?

I have been fully convinced that MR could play an important role in RT. As far back as 2005 Siemens began collaborating with Umeå University Hospital with the installation of a MAGNETOM Espree (70 cm bore size) in the Radiotherapy Department. We started from scratch: Umeå produced a homemade flat-table top and coil holders and

Siemens a transport shuttle system between the MR and the Siemens Artisté linear accelerator. This was the first approach to develop a “new workflow” within a Radiotherapy department through better utilization of MR information.

2014 saw the launch of a national project called “Gentle Radiotherapy”, supported by VINNOVA (The Swedish Governmental Agency for Innovation Systems), where all university hospitals and some healthcare companies in Sweden formed a consortium to develop the use of MR in Radiotherapy. Siemens has been the only diagnostic company to participate and my role has been that of a “Work package leader” for one field: “Optimization of sequences and markers for use of MR in RT applications”.

This project was completed in 2016 and resulted in a Method Book describing the patient handling, safety aspects, coil setups, and optimized protocols for, to date: intracranial malignities, (also stereotactical), head/neck, prostate and brachy cervix. In 2017 a new VINNOVA project was launched to focus on development and clinical implementation of MR-only in RT.

What do you think are the most important developments in MRI?

In MRI, the new techniques for motion management will have a big impact on the clinical outcome of MR examinations and will be able to adapt to the conditions of the individual patient just as the BioMatrix Tuners CoilShim and SliceAdjust adapt to challenging anatomical regions.

What would you do, if you could do for one month whatever you wanted?

Professionally, I would like to dig deeper into a single topic related to MR and Radiation Therapy either by working in a research team or attending University courses. However, I doubt that one month would be enough!

Privately, I would like to spend time at my house in the Stockholm archipelago and take a long boat trip through the Baltic Sea. However, I doubt that one month would be long enough for that, either!

.....

Benjamin Schmitt is Head of Collaborations & Research for Australia and New Zealand. His areas of expertise and professional experience cover research projects and application development in Magnetic Resonance Imaging (MRI). His Ph.D. in Physics/Biophysics from the German Cancer Research Center in Heidelberg (the ‘DFKZ’) in 2011 focused on the implementation of Chemical Exchange Saturation Transfer Imaging on a clinical MR platform. During an extended post-doctorate at the Centre of Excellence for High-Field MR at the Medical University of Vienna, Austria, he worked part-time as applications developer in the musculoskeletal pre-development team in Erlangen, where he adapted and helped integrate several MR sequences to enable clinical 7T MR imaging.

In his current position Benjamin leads a team of five collaborations scientists working closely with Siemens’ research customers in the region to explore the development and implementation of novel MR scanning techniques in clinical routine.





Sydney, Australia

How did you first come in contact with MRI?

It began with the NMR of crystals, the research area of one of the professors at Technical University Kaiserslautern, Germany, where I did my Master's degree in Biophysics. The technology immediately attracted my attention, but I wanted to pursue something more applied to human/medical research in my diploma thesis, so I got in touch with Professor Peter Bachert who leads the MR spectroscopy group at the DFKZ. It was spectroscopy that brought MR to life for me.

What fascinates you most about MRI?

MRI is one of the very rare applications where the principles of quantum mechanics can be applied or even visualized in a macroscopic world. From picture to proton as one famous piece of literature calls it [1]. Australia and New Zealand boasts a motivated MR research environment with some of the brightest minds and thought leaders in the field. This holds especially true for MR in RT where the work from the MR research groups that we work with in Australia set standards in MR in RT worldwide. It paves the way for MR-only treatment planning through new ways, for example, for MR-based attenuation correction in the pelvis or for enhancing the implementation of distortion-reduced MR methods in the treatment planning process.

What do you think are the most important developments in Healthcare?

The advent of faster and more powerful computer hardware in compact space has opened up new avenues for accelerating scans, making examinations more tolerable and more accurate for clinical patients, so it is exciting to see concepts such as Simultaneous Multi-Slice and Compressed Sensing become clinical reality. I believe that computer science can help so much more in medical imaging in general and that this ever increasing computational capacity will turn machine learning approaches into clinical reality, raising our ability to diagnose accurately to the next level.

What would you do, if you could do for one month whatever you wanted?

I would travel around Australia and New Zealand with my family. It is amazing how many beautiful places this part of the world has to offer. I have been here for three and a half years already and despite frequent travelling I have only seen a fraction of what the Pacific region has to offer. My little children love the beach and have probably already spent more time in the sand than I ever did in my entire life before coming to Australia.

Workwise, if I had a whole month, I would make a thorough review of all the wonderful collaborative research work that we have been doing in Australia and New Zealand.

Reference

- 1 DW McRobbie, EA Moore, MJ Graves, MR Prince. MRI from picture to proton. Cambridge University Press.

The entire editorial staff at Princess Margaret Cancer Centre, Toronto, Canada and at Siemens Healthineers extends their appreciation to all the radiologists, technologists, physicists, experts, and scholars who donate their time and energy – without payment – in order to share their expertise with the readers of MAGNETOM Flash.

MAGNETOM Flash – Imprint

© 2017 by Siemens Healthcare GmbH,
All Rights Reserved

Publisher:

Siemens Healthcare GmbH
Magnetic Resonance,
Karl-Schall-Str. 6, D-91052 Erlangen, Germany

Editor-in-chief:

Antje Hellwich
(antje.hellwich@siemens-healthineers.com)

Guest Editor:

Professor David A. Jaffray, Ph.D.
Princess Margaret Cancer Centre
610 University Avenue
Toronto, ON, M5G 2M9
Canada

Editorial Board:

Reto Merges; Wellesley Were;
Sunil Kumar S.L., Ph.D.;
Gary R. McNeal, MS (BME)

Review Board:

Matthias Drobnitzky; Daniel Fischer;
Elena Nioutsikou, Ph.D.; Efren Ojeda;
Martin Requardt, Ph.D.; Glen Roberts;
Gregor Thörmer, Ph.D.

Production:

Norbert Moser,
Siemens Healthcare GmbH

Layout:

Agentur Baumgärtner,
Friedrichstr. 4, D-90762 Fürth, Germany

Printer:

Schmidl & Rotaplan Druck GmbH,
Hofer Str. 1, D-93057 Regensburg, Germany

Note in accordance with § 33 Para.1 of the German Federal Data Protection Law: Despatch is made using an address file which is maintained with the aid of an automated data processing system.

MAGNETOM Flash is sent free of charge to Siemens MR customers, qualified physicians, technologists, physicists and radiology departments throughout the world. It includes reports in the English language on magnetic resonance: diagnostic and therapeutic methods and their application as well as results and experience gained with corresponding systems and solutions. It introduces from case to case new principles and procedures and discusses their clinical potential. The statements and views of the authors in the individual contributions do not necessarily reflect the opinion of the publisher.

The information presented in these articles and case reports is for illustration only and is not intended to be relied upon by the reader for instruction as to the practice of medicine. Any health care practitioner reading this information is reminded that they must use their own learning, training and expertise in dealing with their individual patients. This material does not substitute for that duty and is not intended by Siemens Healthcare to be used for any purpose in that regard. The drugs and doses mentioned herein are consistent with the approval labeling for uses and/or indications of the drug. The treating physician bears the sole responsibility for the diagnosis and treatment of patients, including drugs and doses prescribed in connection with such use. The Operating Instructions must always be strictly followed when operating the MR system. The sources for the technical data are the corresponding data sheets. Results may vary.

Partial reproduction in printed form of individual contributions is permitted, provided the customary bibliographical data such as author's name and title of the contribution as well as year, issue number and pages of MAGNETOM Flash are named, but the editors request that two copies be sent to them. The written consent of the authors and publisher is required for the complete reprinting of an article.

We welcome your questions and comments about the editorial content of MAGNETOM Flash. Please contact us at magnetomworld.med@siemens.com.

Manuscripts as well as suggestions, proposals and information are always welcome; they are carefully examined and submitted to the editorial board for attention. MAGNETOM Flash is not responsible for loss, damage, or any other injury to unsolicited manuscripts or other materials. We reserve the right to edit for clarity, accuracy, and space. Include your name, address, and phone number and send to the editors, address above.

MReadings: MR in RT is also available online:

www.siemens.com/magnetom-world-rt

On account of certain regional limitations of sales rights and service availability, we cannot guarantee that all products included in this brochure are available through the Siemens sales organization worldwide. Availability and packaging may vary by country and is subject to change without prior notice. Some/All of the features and products described herein may not be available in the United States.

The information in this document contains general technical descriptions of specifications and options as well as standard and optional features which do not always have to be present in individual cases, and which may not be commercially available in all countries.

Due to regulatory reasons their future availability cannot be guaranteed. Please contact your local Siemens organization for further details.

Siemens reserves the right to modify the design, packaging, specifications, and options described herein without prior notice. Please contact your local Siemens sales representative for the most current information.

Note: Any technical data contained in this document may vary within defined tolerances. Original images always lose a certain amount of detail when reproduced.

Siemens Healthineers Headquarters

Siemens Healthcare GmbH
Henkestr. 127
91052 Erlangen
Germany
Phone: +49 9131 84 0
[siemens.com/healthineers](https://www.siemens.com/healthineers)